UNIVERSITY OF STRATHCLYDE
DEPARTMENT OF PHYSICS

Optical diagnosis of dense plasma evolution during irradiation by ultra-intense laser pulses

by

Jonathan Pacitti Jarrett

in partial fulfilment of the requirements for the degree of Doctor of Philosophy in Physics

2021

Copyright Declaration

Signed: 

Date: 12/05/2021

Abstract

Intense laser-solid interactions have been the focus of much research for a number of decades, and many attractive properties have been demonstrated, such as the ability to produce beams of highly energetic particles, as well as intense X-ray, γ-ray, and THz radiation. This thesis reports on investigations into ultra-intense ($10^{19} - 10^{21}$ Wcm^{-2}) laser-solid interactions, using optical diagnostic techniques applied at state-of-the-art high power laser facilities. Experiments and numerical modelling are undertaken to introduce new methods of optically probing the properties of dense plasmas and their evolution during irradiation by intense laser light. The results reported provide new insight into the physical processes occurring, and the methods that are developed and demonstrated in this thesis have the potential to be employed on future experiments to characterise laser-plasma interactions.

The new results introduced in this thesis are presented in three parts. In the first, experimental measurements of the specularly reflected light from the front surface of microstructured targets are reported. Based on these measurements and ray-tracing modelling, an analytical model is developed that utilises microstructured targets, and measurements of the spacing between the intensity maxima in the reflected light, to determine the laser focal spot size and the electron temperature within the region of the laser focal spot. These properties are difficult to measure by other means, and so the method proposed could be employed on future experiments to provide an enhancement to the research being undertaken.

The second study is an investigation of stripe patterns measured in the profile of the laser light transmitted through expanding ultrathin foil targets, as they undergo

relativistic self-induced transparency. Analysis of these results, along with numerical modelling, demonstrate that the size, ellipticity, and angular orientation of the plasma aperture directly influences the spatial-intensity distribution of these stripes. Previous studies have shown the potential for directly controlling the distribution of the electron beams produced during laser-plasma interactions by altering the spatial properties of the relativistic plasma aperture. The results presented here form part of an important study into how relativistic self-induced transparency can be utilised to enhance laser-driven ion acceleration.

In the final study, measurements of the spectra of laser light back-reflected from thin foil targets are analysed. Observed shifting and broadening of the spectra, relative to the input laser spectrum, is discussed. It is found that the interaction between the outwards expansion due to thermal pressure and the inwards laser hole-boring radiation pressure can be probed by spectral measurements. The force which is dominant over the timescale of the interaction can be determined. From this, a diagnostic technique is presented that could be employed on future experiments to probe the direction of motion of the plasma critical surface during irradiation. In addition, this technique provides a method of estimating the reflectivity of the plasma, through measuring the degree of self-phase modulation occurring in the spectra.

These three studies provide new insight into the complex dynamics of relativistically intense laser-plasma interactions, and demonstrate optical techniques that can be utilised in future experimental investigations to diagnose various properties of the motion and evolution of the dense plasma.

Acknowledgements

The work contained in this thesis would not have been possible without the help of many wonderful colleagues, collaborators and family and friends. Particular thanks go to my supervisor Prof. Paul McKenna, for his excellent expertise and encouragement, and for giving me the opportunity to carry out this PhD. Also to Ross Gray, Martin King, and Robbie Wilson, for their ongoing support and advice, without whom this work would not have been possible. Thanks go to the extremely helpful staff and collaborators at the Central Laser Facility, and Orion, AWE, whose knowledge and expertise facilitated the success of several experimental investigations. I would also like to thank Matthew and Tim, for the company, thoughtful discussions, and mutual love for coffee, as well as my many other colleagues at Strathclyde. I would like to extend my deepest thanks to my family, for their ongoing support and encouragement, and for motivating me to pursue my interest in science, and to Karolina, who has kept me going through the final year of this work.

Finally, acknowledgement goes to the financial contributions from EPSRC and AWE plc towards my PhD studentship.

Role of author

The author played a substantive role in the experimental work discussed in chapter 4, and one of the experiments discussed in chapter 5. All of the analysis of the results presented in this thesis was carried out by the author, with the close collaboration of Prof. Paul McKenna, Dr. Ross Gray, Dr. Martin King, and Dr. Robbie Wilson.

Chapter 4 - The author played the primary role in the set up and running of the specular reflection imaging diagnostic, and the analysis of the data from the measurements. The 2D PIC simulations were run by Dr. Martin King, and the analysis and interpretation of the simulation results was carried out by the author. The author developed the numerical model used to describe the evolution of the critical surface profile of the groove targets, and carried out the analysis of the results. The ray-tracing modelling, and subsequent analysis, was carried out by the author with the collaboration of Dr. Martin King, and the Huygens-Fresnel modelling and analysis was carried out by Dr. Martin King with the collaboration of the author. Prof. Paul McKenna provided input throughout the discussion and analysis.

Chapter 5 - The author was responsible for the design and running of the diagnostic for imaging the transmitted laser light for one of the three experiments discussed (TAP 2018, experiment C) and the analysis of the resulting data, as well as the analysis and interpretation of the data arising from the other two experiments. The author carried out the ray-tracing technique used for modelling the propagation of the light through an aperture, with the assistance of Dr. Robbie Wilson, and conducted the analysis of the data produced. The author was also responsible for conducting the PIC simulations, and analysing the results.

Chapter 6 - The author played the primary role in the analysis and interpretation of the experimental data discussed in this chapter, as well as the running and analysis of the 1D PIC simulations. The 2D PIC simulations were carried out by Dr. Martin King, and the resulting data were interpreted and analysed by the author. The modelling and analysis used in determining the influence of self-phase modulation was carried out by the author, with the collaboration of Dr. Ross Gray. Additionally, Dr. Martin King, Dr. Ross Gray, and Dr. Robbie Wilson provided input to the discussions and analysis throughout the work reported in this chapter.

Publications

- **Reflection of intense laser light from microstructured targets as a potential diagnostic of laser focus and plasma temperature**

  J. Jarrett, M. King, R. J. Gray, N. Neumann, L. Döhl, C. D. Baird, T. Ebert, M. Hesse, A. Tebartz, D. R. Rusby, N. C. Woolsey, D. Neely, M. Roth, and P. McKenna. High Power Laser Science and Engineering, **7**, e2. (2018)

- **Enhanced laser intensity and ion acceleration due to self-focusing in relativistically transparent ultrathin targets**

  T. P. Frazer, R. Wilson, M. King, N. M. H. Butler, D. C. Carroll, M. J. Duff, A. Higginson, J. Jarrett, Z. E. Davidson, C. Armstrong, H. Liu, D. Neely, R. J. Gray, P. McKenna. Phys. Rev. Research **2**, 042015 (2020)

- **Enhanced brightness of a laser-driven X-ray and particle source by microstructured surfaces of silicon targets**

  T. Ebert, N. W. Neumann, L. Döhl, J. Jarrett, C. D. Baird, R. Heathcote, M. Hesse, A. Hughes, P. McKenna, D. Neely, D. Rusby, G. Schaumann, C. Spindloe, A. Tebartz, N. C. Woolsey, M. Roth. Physics of Plasmas **27**, 043106 (2020)

Contents

List of Figures

Chapter 1

Introduction

This thesis reports on work carried out in the field of ultra-intense laser plasma interactions, and in the following sections the background and motivations relating to this fascinating area of research is provided. An overview of the history and development of the laser, and a discussion about the strive for ever increasing laser intensities that made the field of research of laser-plasma interactions possible is provided. Subsequently, some of the key applications of laser-solid interactions that motivate research to continue to push the frontiers of this field of study are discussed.

1.1 History of the laser

The history of the laser (light amplification by stimulated emission of radiation) begins, as with many of the greatest scientific discoveries, with Albert Einstein. In 1917, his paper, *Zur Quantentheorie der Strahlung* (On the Quantum Theory of Radiation), laid out the foundations for the principle of operation of a maser (microwave amplification by stimulated emission of radiation), and subsequently the laser, by theorising that a photon could act to stimulate an excited atom to emit a photon of identical characteristics, thereby producing the phenomenon known as stimulated emission [1]. Unfortunately, Einstein never lived to see the laser become a reality, as it was many years later, in 1960, that the first working device was developed by Theodore Maiman at Hughes Research Laboratories, California [2]. There, using a flash-lamp driven ruby

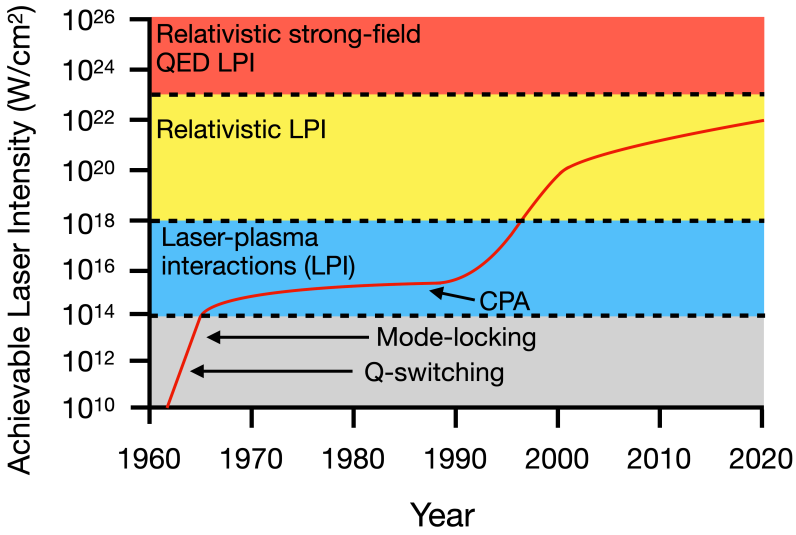

Figure 1.1: Plot showing advancement over time of peak laser intensity achievable, with the development of notable laser technologies shown.

crystal, he created the first laser, something that due to its natural monochromatic and coherent properties, and its ability to produce light of extreme brightness with very low input energy, has since evolved into one of the most important, and ubiquitous pieces of technology ever conceived. Lasers subsequently are now used in a staggering number of different applications, devices, and fields of research, and almost all of us rely on one at some point, in some form, every single day. However, upon announcement, his invention was immediately dismissed as being nothing but "a solution looking for a problem".

Fortunately, the story of the laser did not end there, but instead its development rapidly continued. New types of lasers, such as gas lasers, semiconductor lasers, and fibre lasers were produced, and importantly for the work presented in this thesis, the peak intensities of light that could be reached continued to increase, as illustrated in figure 1.1.

Following the first demonstration of the laser in 1960, several new technologies were discovered that facilitated significant increases in the peak laser intensities that were achievable. In 1961, a method of producing intense pulses of laser light known as Q-switching was developed, which allowed kilojoule, nanosecond pulses of light to

be produced [3]. This was closely followed by the development of mode-locking, which provided a means of reducing the achievable pulse durations down into the femtosecond range [4]. These technologies enabled intensities of up to 10^{16} Wcm^{-2} to be achieved, pushing past the ionisation threshold for solids, and marked the beginning of the study of laser-plasma interactions. Later, in 1985, the discovery of a method of laser amplification known as chirped pulse amplification [5], gave rise to a significant jump in the achievable peak laser intensities, pushing laser-plasma interactions well into the relativistic regime ($> 10^{18}$ Wcm^{-2}). This technique is discussed in more detail in section 3.1.1. More recently, advancements in the design of high-power laser facilities has enabled peak laser intensities of 10^{22} Wcm^{-2} to be reached [6,7], and plans for achieving intensities of 10^{23} Wcm^{-2} are well under way [8].

1.2 Motivations for the study of laser-plasma interactions

Due to the extreme intensities and energy densities of laser light that can be produced, many exotic phenomena that only occur naturally in astrophysical environments, can be studied in the laboratory. From this, many new branches of scientific research have been made possible, such as the study of high energy density physics [9], the propagation of shocks [10], and the creation of warm dense matter [11], as well as many more.

As well as enabling many new areas of scientific research, several other applications of laser-plasma interactions have been proposed. One of the envisioned applications that drove much of the initial research and development, was the aim of achieving nuclear fusion via a process known as direct-drive inertial confinement fusion, by using beams of intense laser light to compress a fuel pellet of deuterium and tritium to the point that fusion can occur. First proposed in Nuckolls *et al.* [12] in 1972, this process involves a spherical fuel pellet being evenly irradiated by multiple nanoseconds laser pulses simultaneously, rapidly heating the outer shell of the pellet and forming an outwards-expanding plasma. As it expands outwards, this coronal plasma imparts a reactionary force inwards, acting to compress the shell in towards the core of the pellet, producing immense, gigabar pressures, and temperatures of ~ 10 keV within the fuel

cell, reaching the criteria needed for fusion to occur [13].

In the years since, other variations of this scheme have been explored. A method known as fast ignition was proposed in 1994 [14], whereby the spherical fuel pellet is rapidly heated and compressed in the same manner as before, but just as the material in the pellet reaches peak temperature and pressure, an additional short, ultra-intense laser pulse is focussed into the coronal plasma surrounding the pellet. This pulse is absorbed into the dense plasma surrounding the core, transferring its energy into a beam of highly energetic electrons. These electrons then in turn penetrate into the core of the fuel pellet, depositing their energy and heating the material to the temperature required for fusion to occur ($\sim$ 5 keV). This method aims to overcome some of the issues that the direct-drive scheme has, such as the growth of instabilities due to the irregularity of the pellet surface or asymmetries in the irradiation of the pellet [15], which can lead to poor compression of the fuel cell. In addition, the compression densities that are required to be reached are lower than in the case of the direct-drive scheme, reducing the laser energies that must be employed. Other variations of inertial confinement fusion have been proposed and tested since, such as the indirect drive approach [16], and to this day achieving fusion remains one of the key motivations that drives researchers to understand better the complex dynamics of laser-plasma interactions.

Another of the key motivating factors in the research of laser-plasma interactions, is the use of highly intense laser pulses as a means of particle acceleration and high energy radiation generation. The acceleration of ions using a potential difference applied across a fixed electrode, typically involving RF drivers, has been an ongoing area of scientific research since the 1930s, and has seen significant progress over the years. Modern particle accelerators that are at the forefront of science today, such as the Large-Hadron Collider (LHC), are able to achieve proton energies that reach into the TeV range, the collisions of which generate exotic states of matter and allow for research to be conducted into the creation of antimatter, the Higgs boson, and quark-gluon plasmas, amongst many other phenomena [17].

These accelerators, although impressive in their capabilities, are also impressive in their scale. At tens of kilometres in circumference, accelerators such as the LHC are

few and far between, and even the more compact cyclotrons and synchrotrons that are in use today for applications such as proton beam therapy, are still fairly large ($\sim$ 20 m diameter) and expensive pieces of equipment. The cost and space requirements of these "conventional" accelerators, therefore, significantly restricts where they can be used, and subsequently, there has been much interest in developing novel schemes of particle acceleration which are cheaper and more compact. One avenue of research that has shown much promise in these regards, is the utilisation of the interaction between a high-intensity laser pulse and a plasma, to drive the acceleration of ions. In order to accelerate the ions, a significant accelerating gradient is required, which in the case of conventional accelerators can only reach a few tens of MVm^{-1} before the materials of the accelerator begin to break down. Laser-solid interaction based accelerators, however, can produce acceleration gradients that reach into the TVm^{-1} range, 4 or more orders of magnitude greater, and can produce energetic beams of ions with a low transverse emittance of < 0.004 mm·mrad [18], around 2 orders of magnitude better than other accelerators. Because of the greater acceleration gradients that plasma-based accelerators offer in comparison to conventional accelerator techniques, the acceleration distances that are needed in order to reach the particle energies required are greatly reduced. As a result, proton beams of tens of MeV can be produced from acceleration distances of just microns [19, 20], and although these laser systems are typically housed in fairly large facilities at the moment, continued efforts towards miniaturisation could allow for particle accelerators to be reduced considerably in size in the future. In addition, further increases to the achievable particles energies, and the ability to accelerate hadrons to hundreds of MeV, could allow for treatments such as proton beam therapy [21] to become much more readily accessible, which is currently an extremely expensive and technically difficult form of treatment to provide [22].

As well as particle acceleration, laser-solid interactions have also shown great promise as sources of various forms of electromagnetic radiation. Much work has been done on utilising these interactions as sources of UV and X-ray radiation [23, 24], as well as a means of generating THz radiation, which has potential as a means of non-invasive imaging for biological [25], industrial [26], and security applications [27].

1.3 Probing of laser-plasma interactions via measurement of laser light and X-ray emission

As a result of the new fundamental physics accessible, such as transient warm dense matter, high field physics, and shock physics, and the many potential applications of laser-plasma interactions, significant research into the physics of these interactions is ongoing, and many different methods have been developed to probe the physical properties of these interactions, and infer the behaviour of the plasma. In addition to probing the interaction physics, by measuring the properties of the particles and radiation emitted from the plasma, substantial new insights can be gained from the measurement of the light reflected from, transmitted through, or generated within the plasma. As a laser pulse irradiates a solid target, ionises it, and then interacts with the resulting plasma, the energy content, as well as the spatial, temporal, and spectral characteristics of the pulse are modified by the physical properties of the evolving plasma. The collection and measurement of this light, and analysis of how it has been modified during the interaction, can therefore be used in numerous ways to reveal information about the behaviour of the plasma, as well as the underpinning physics governing the interactions.

Subsequently, there have been many techniques developed over the decades to optically probe laser-plasma interactions. One technique that has been in use since the 1990s, known as K-alpha X-ray imaging, is a method for measuring the propagation of electrons through a plasma during irradiation by an intense laser pulse, via the use of a spherically curved quartz crystal [28, 29]. As energetic electrons, known as "fast electrons", are accelerated through the target plasma, they undergo collisions with the atoms of the target, emitting X-ray photons [30]. The energy of the X-ray photons that are emitted is related to the material from which they are generated, and so if a thin layer of a particular material, such as copper, is embedded within the target, then X-ray photons with an energy corresponding to copper K-alpha radiation will be produced from within that region. With careful selection of its physical properties, a spherically curved quartz crystal can be used to direct the copper K-alpha X-rays

towards a detector, such as a CCD camera or imaging plate, allowing for a 2D image to be produced of the region from which the X-rays are produced. By irradiating a series of targets with buried layers of copper located at different depths, the divergence of the beam of energetic electrons can be determined. As well as measuring the spatial properties of the fast electron beam, K-alpha X-ray imaging can be used to probe the temperature of the fast electrons [31]. This diagnostic technique has been employed on many laser-solid experiments, and has enabled researchers to gain valuable information about the processes occurring within the plasma. However, this technique is limited to measuring the temperature of only the fast electrons propagating through the target. Measuring the plasma temperature in the region of the laser focal spot can prove to be a significant challenge, and will be the focus of the work in the first study reported in this thesis.

As well as the use of a spherically curved quartz crystal to image the X-ray emission, another technique that has been developed is the use of a pinhole camera to measure the size of the source of X-ray emission on the front or rear surfaces of the target [32]. Through the measurement of this source size on the front surface of the target, the size of the laser focal spot can be inferred. Although a useful technique, pinhole imaging does not give a direct measurement of the size of the laser focus, as the region of X-ray emission on the target front surface is larger than the focal spot of the laser due to lateral expansion of the region of hot plasma during the integration time of the diagnostic [33]. Measuring the focal spot size of the laser during a full-power shot still remains difficult, which will also be addressed in the first study of this thesis.

Frequency-resolved optical gating (FROG), invented in 1991 by R. Trebino, was the first diagnostic technique developed that allowed for the spectral phase of an ultrashort laser pulse to be measured [34]. This method involves splitting the laser pulse required to be measured via a beamsplitter, and delaying one pulse in time relative to the other. The two pulses are then recombined at a focal point within a nonlinear crystal, which generates an output signal pulse when the two pulses overlap. By measuring this signal multiple times with different delays between the two components of the input pulse, a measurement can be made of the pulse duration of the original pulse. In addition,

the FROG technique can also resolve the spectrum of the pulse as a function of time, allowing for a more complete measurement of the properties of the laser pulse, and facilitating chirps in the wavelength of the pulse to be probed [35]. Since the invention of the FROG, many variants of the technique have been developed, each with their own benefits [36]. The polarisation-gated FROG is a variant that is easier to align than other methods, but requires a polariser with a high extinction ratio to operate. The self-diffraction FROG can be used with a wide range of wavelengths, but requires high laser energies to function. The second-harmonic FROG boasts greater sensitivity than other variants, but introduces an ambiguity in the direction of time of the measured pulse. Although these techniques are able to measure a great deal of information about the input laser pulse, in order to interpret the data, complex phase retrieval algorithms are required, often requiring specific computer software to implement.

Many other optical techniques have been developed for probing laser-plasma interactions, and continue to contribute to our understanding of the physical processes that occur. As a result, further development and optimisation of laser-plasma interactions can be sought, bringing the potential applications closer to reality. As such, this thesis reports on data measured during experimental investigations using optical diagnostic techniques, presents analysis and modelling that helps to provide a greater understanding of the physical processes that occur during laser-solid interactions, and demonstrates new diagnostic techniques that could be employed in the future.

1.4 Thesis outline

The following chapter presents some of the underlying physics of plasmas and laser-solid interactions and some key aspects of the propagation of a laser through a plasma, as well as discussing the nonlinear effects that come into play. Chapter 3 covers the methodology of using high power laser systems, and the diagnostic and simulation techniques used. Chapters 4, 5 and 6 introduce the key experimental findings as follows:

- Chapter 4 - A study of the interaction of high power laser light with structured targets is presented, and is part of an investigation of schemes to enhance laser

energy absorption and coupling to particles and radiation. Experimental measurements of spatial structure in the specularly-reflected light is analysed, and numerical modelling techniques are employed to explore a method of diagnosing the plasma temperature and laser focal spot size.

- Chapter 5 - An investigation into the formation of stripe patterns in the transmitted laser light is presented, as part of an ongoing study into the process of relativistic self-induced transparency. Analysis of spatial structuring in the laser light transmitted through an expanding, initially solid target undergoing relativistic self-induced transparency is presented. Modelling is carried out to investigate the influence that the size, ellipticity, and orientation of the plasma aperture has on the distribution of the patterns.

- Chapter 6 - A study into probing the motion of the plasma critical surface, due to the interaction of outwards thermal expansion, and inwards hole-boring, is reported. Analysis of measurements of the spectra of back-reflected laser light from the irradiation of ultra-thin foil targets by an ultra-intense laser pulse is presented, along with modelling to determine the cause of differences in the direction of wavelength chirp measured, when comparing p-polarised and c-polarised laser light. Additionally, the influence of self-phase modulation in these spectra is modelled and discussed.

A final conclusions chapter is then presented, giving a summary of the work reported in chapters 4, 5, and 6, along with some future avenues of research to potentially build upon this work.

Chapter 2

Fundamentals of laser-plasma interactions

2.1 Introduction to high power lasers

The laser systems that are being considered in this thesis, are petawatt class, pulsed lasers, which deliver all their energy into one, ultra-intense pulse. Although the total energy delivered by these lasers onto a target material is only a few tens or hundreds of Joules, enough energy to heat just a teaspoon of water by about 10 degrees, this energy is delivered near instantaneously, within less than a picosecond, and is focussed down to a spot with a diameter of just a few microns. The scenarios that are being considered in this thesis, are the interactions between an ultra-intense laser pulse and a solid density material (referred to as a "target"). These interactions are referred to "ultra-intense laser-solid interactions", where "ultra-intense" refers to the fact that the laser intensities being used at the upper end of what is achievable with current laser technology, reaching on-target peak intensities of $> 10^{20}$ Wcm^{-2}. The sudden deposition of energy into the target material rapidly heats and ionises it, forming a plasma, as will be discussed further in section 2.3. The resulting interaction of the intense laser pulse with this plasma state, across a wide range of temporal and density scales, results in myriad physical phenomena, including laser-energy coupling, field

generation and high energy radiation and particle production. In the following sections the key underpinning physics of these phenomena are detailed.

2.2 Self-phase modulation

Due to the high intensity, and short duration of these laser pulses, nonlinear optical effects often become a significant factor in the behaviour of the light. One such effect that will now be covered is known as self-phase modulation (SPM), which is of importance to the discussion in chapter 6. First demonstrated in the 1960s [37–39], this effect arrises due to the modulation of the refractive index of the medium caused by the optical Kerr effect where, as a laser pulse propagates through a material, it induces a variation in the refractive index of the medium, which in response acts to modulate the phase of the pulse that is propagating through. This phase shift results in the pulse of light causing a change in its own frequency spectrum, as the magnitude of this phase shift is related to the temporal intensity profile of the laser pulse. This modulation in the instantaneous frequency of the pulse can be examined by starting with the intensity of an ultrashort laser pulse propagating through a medium as a function of time:

$$I(t) = I_0 \exp\left(-\frac{t^2}{\tau^2}\right) \tag{2.1}$$

where I_0 is the peak intensity of the laser and τ is half of the pulse full-width-half-maximum (FWHM). As mentioned before, the optical Kerr effect induces a change in the refractive index of the material, such that:

$$n(I) = n_0 + n_2 \cdot I(t) \tag{2.2}$$

where n_0 is the linear refractive index of the material, and n_2 is the second-order nonlinear refractive index. As the pulse propagates through the material, the temporal profile of the laser intensity results in the medium having a time-varying refractive index due to the Kerr effect. For a simple Gaussian temporal intensity profile this can

be expressed as:

$$\frac{dn(I)}{dt} = n_2 \frac{dI}{dt} = n_2 \cdot I_0 \cdot \frac{-2t}{\tau^2} \cdot \exp\left(\frac{-t^2}{\tau^2}\right) \tag{2.3}$$

This time-variation in the refractive index that is induced in the medium acts to modulate the instantaneous phase of the laser pulse, $\phi(t)$ that is propagating through, such that:

$$\phi(t) = \omega_0 t - kz = \omega_0 t - \frac{2\pi}{\lambda_0} \cdot n(I)L \tag{2.4}$$

where ω_0 is the frequency, and λ_0 the central wavelength of the laser, L is the propagation distance through the medium, and wavenumber $k = 2\pi/\lambda_0$. This shift in the phase of the pulse in turn modifies the frequency, and so we can express the instantaneous frequency of the pulse as:

$$\omega(t) = \frac{d\phi(t)}{dt} = \omega_0 - \frac{2\pi L}{\lambda_0} \frac{dn(I)}{dt} \tag{2.5}$$

Using equation 2.3, we can finally obtain an expression of how the instantaneous frequency of the pulse varies with time, as it propagates through a medium:

$$\omega(t) = \omega_0 + \frac{4\pi L n_2 I_0}{\lambda_0 \tau^2} \cdot t \cdot \exp\left(\frac{-t^2}{\tau^2}\right) \tag{2.6}$$

This self-phase modulation of the laser pulse as it propagates through a medium acts to shift the leading edge of the pulse towards redder wavelengths, and the trailing edge of the pulse to bluer wavelengths, whereas at the peak of the pulse, where the gradient of the intensity is zero, there is no shift in the frequency of the pulse. This is illustrated in figure 2.1.

For a laser pulse that does not possess any frequency chirp initially, such that all the frequencies arrive simultaneously, or is positively-chirped, where the frequency increases with time, the effect of self-phase modulation as this pulse propagates through a medium acts to broaden the spectrum of the pulse. If however the pulse is negatively-chirped, where the frequency decreases with time, then SPM will act to compress the spectrum [40–43]. As the intensity of the pulse increases, the degree of self-phase modulation becomes more extreme, leading to the formation of so-called "side-bands"

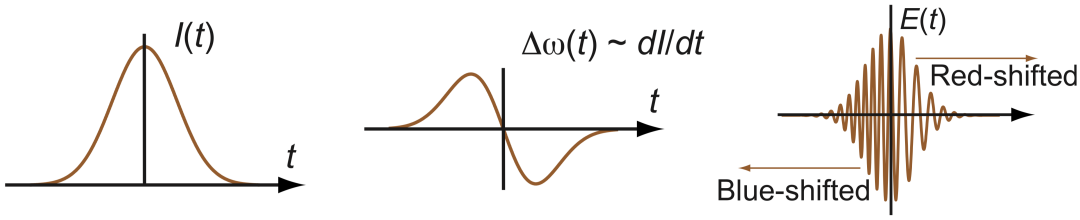

Figure 2.1: Plots showing the effect of self-phase modulation. Left - temporal profile of the intensity of a Gaussian pulse. Centre - frequency shift due to SPM as a function of time. Right - pulse after SPM. On the first half of the pulse, the rising intensity induces a red-shift of the pulse towards lower frequencies, and on the second half of the pulse, the falling intensity leads to a blue-shift towards higher frequencies. [44]

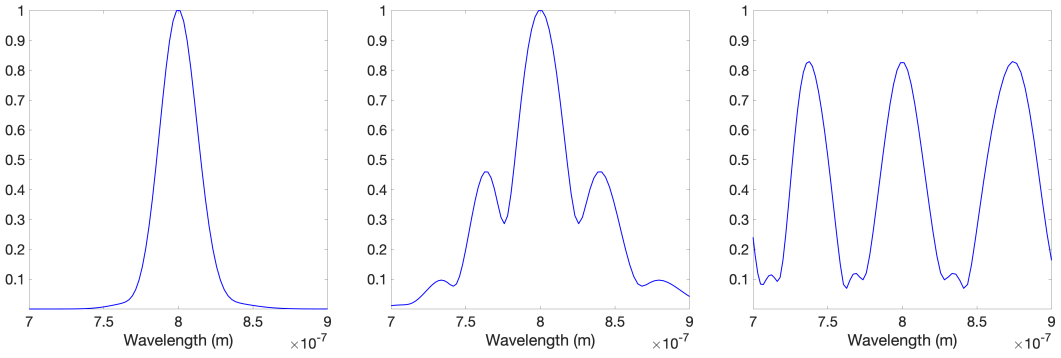

(a) (b) (c)

Figure 2.2: Plots showing the normalised spectrum of a laser pulse after passing through 2.5 cm of glass, highlighting the effect of self-phase modulation for a peak laser intensity of (a) 10^9 Wcm^{-2}, (b) 10^{10} Wcm^{-2}, and (c) 10^{11} Wcm^{-2}.

in the spectrum of the light, and eventually, if the effect of SPM becomes sufficient, the spectrum will develop periodic peaks ringing out over a large range of wavelengths [39, 45].

Figure 2.2 illustrates the formation of side-bands in the spectrum of a laser with a central wavelength of 800 nm, such as the Gemini laser at the Rutherford Appleton Laboratory (discussed more in section 3.2), due to self-phase modulation as the laser propagates through 2.5 cm of glass. For very high laser intensities, we can see that this modulation of the spectrum becomes so extreme, that these side bands develop into regular, periodic, structures that can extend over a very wide spectral range. This effect can be exploited for the purpose of the generation of a supercontinuum, where

laser light is passed through a medium such as a nonlinear crystal, or an optical fibre, with the aim of maximising the spectral broadening from self-phase modulation to such a degree that the light produced spans a large range of wavelengths, or even becomes a source of white light [46].

2.3 Laser-induced ionisation

Next, some of the processes of laser-induced ionisation will be covered, as this is an important aspect of the laser-target interaction. Ionisation is the process of an atom losing or gaining electrons, producing an ion with either a negative or positive charge respectively. This is a key process for laser-target interactions as this ionisation produces a population of free electrons on the front surface the target, which is necessary for the primary laser absorption mechanisms to occur, as discussed in section 2.7. The two ionisation processes that will be briefly discussed are multi-photon ionisation, which plays a significant role in ionisation of the target when the laser intensity is low $\approx 10^{10}$ Wcm^{-2} and was first proposed in 1931 [47], and barrier suppression, which becomes significant as the laser intensity increases past 1.4×10^{14} Wcm^{-2}.

2.3.1 Multi-photon ionisation

To understand the process of multi-photon ionisation, we first consider an electron trapped in the Coulomb potential well of an ion, where the electron needs to absorb a certain amount of energy in order to overcome that potential and escape the influence of the ion. If we consider an electron trapped in a hydrogen atom, then the electric field of this atom can be expressed as:

$$E_a = \frac{e}{4\pi\epsilon_0 a_B^2} \tag{2.7}$$

where e is the charge of an electron, ϵ_0 is the permittivity of free space, and a_B is the Bohr radius, which is the distance between the nucleus of a hydrogen atom and its electron and is equal to 5.3×10^{-11} m. This results in the electric field strength of a hydrogen atom being 5.1×10^{9} Vm^{-1}, and from this the atomic unit of intensity can be

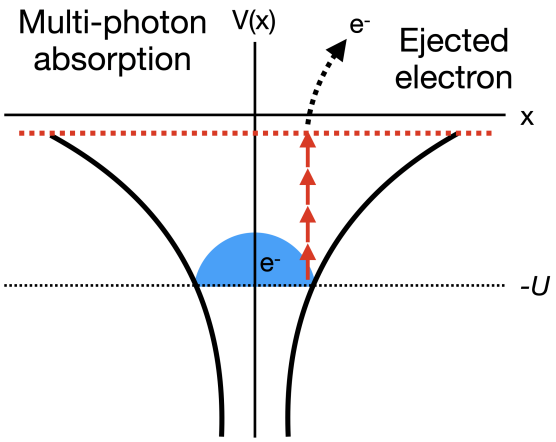

Figure 2.3: Schematic of multi-photon ionisation. Here the electron, shown in blue, is initially trapped in the potential well of an atom with an ionisation potential U, and absorbs the energy of multiple photons, shown in red, eventually gaining enough energy to overcome this potential energy barrier.

found:

$$I_a = \frac{\epsilon_o c E_a^2}{2} \tag{2.8}$$

This intensity is equal to $3.5{\times}10^{16}$ Wcm^{-2}, which is the intensity required to ionise a hydrogen atom, and in our context of using high power laser systems, this intensity of light will readily occur once the main pulse of the laser arrives and the intensity ramps up. Prior to the arrival of this main pulse, there is typically a certain level of background light that impinges on the target, known as amplified spontaneous emission, or ASE, which will be discussed in more detain in section 3.1.3. Each individual photon in this ASE light is of too low an energy to directly ionise the target material. However the arrival of many photons within a short period of time can lead to ionisation through the process of multi-photon ionisation.

Multi-photon ionisation occurs when the flux of incoming photons is high enough that, even although the energy of each individual photon is not sufficient to free the electron from its potential well, the addition of many lower energy photons can cumulatively transfer enough energy into the electron to free it from the ion, a schematic of which is shown in figure 2.3. As an example, a hydrogen atom will require 12 photons of 1 μm light to be absorbed by the electron within 0.5 fs in order for the atom to be

ionised. The final energy of this electron, E_f can be expressed as:

$$E_f = (n + s)\hbar\omega_L - U \tag{2.9}$$

where n is the number of photons required to ionise the electron, s is the number of additional photons absorbed, $\hbar$ is the reduced Planck constant, ω_L is the laser angular frequency, and U is the ionisation potential of the atom, i.e. the barrier energy it had to overcome. This process results in intensities of light of only around 10^{10} Wcm^{-2} being able to induce ionisation of the target.

2.3.2 Field ionisation by barrier suppression

The second ionisation mechanism that is relevant to the work presented in this thesis, is known as field-ionisation by barrier suppression. Considering again the example of an electron trapped in the Coulomb potential of an ion, in order for the electron to escape, it needs to have sufficient energy to overcome this potential, which it can get from gaining energy via the process described above. However, the electron can also overcome the Coulomb potential of an ion if the field of the ion is suppressed by an external electric field, such as the electric field of an intense laser pulse. This suppression of the Coulomb potential by an external field is known as barrier suppression, and if the intensity of the external field is great enough, such as 1.4×10^{14} Wcm^{-2} for a hydrogen atom, then the potential well can become suppressed sufficiently to allow for the electron to tunnel through the barrier via quantum tunnelling, or simply escape the well directly if the field is suppressed completely. This process of field-ionisation by barrier suppression requires higher laser intensities than multi-photon ionisation to occur. Each mechanism will dominate over the other depending on the intensity of the laser light on the target. These two ionisation mechanisms have been described in Keldysh *et al.* [48] who related them to each other via the Keldysh parameter γ_K, given as:

$$\gamma_K = \omega_L \sqrt{\frac{2U}{I}} \tag{2.10}$$

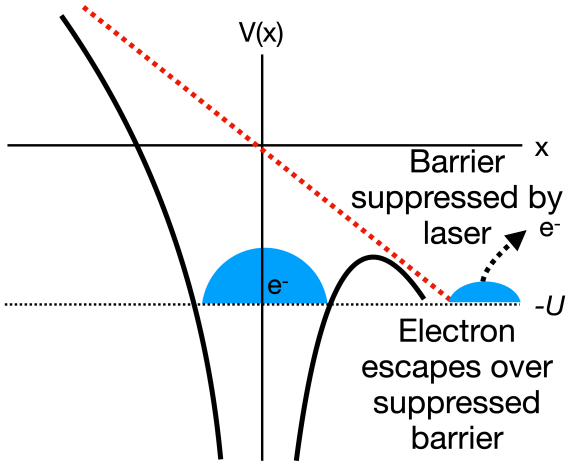

Figure 2.4: Schematic of ionisation by barrier suppression. Here the atomic potential field of the ion is significantly suppressed by an intense laser field, allowing the electron to escape over the barrier.

where I is the laser intensity. This parameter is a convenient way of differentiating between which of the two mechanisms is dominant as, if $\gamma_K > 1$, then multi-photon ionisation is the primary ionisation mechanism, and if $\gamma_K < 1$, then field ionisation by barrier suppression dominates.

2.4 Electron motion in an electromagnetic wave

2.4.1 Single electron motion in an infinite plane wave

In the previous sections, the formation of a plasma due to the irradiation of a target material by an ultra-intense laser pulse was described, along with some of the key parameters that are used. In this section the motion of a single electron in an infinite plane electromagnetic wave will be considered. When a free electron, that is an electron that is not bound to an atom, is placed in an external EM field, its motion is governed by the Lorentz force, $\mathbf{F}_L$. This force describes how an electric field and magnetic field will each exert a force on an electron, and is shown below:

$$\mathbf{F}_L = \frac{d\mathbf{p}}{dt} = -e(\mathbf{E} + \mathbf{v} \times \mathbf{B}) \tag{2.11}$$

In this equation, $-e$ is the charge of the electron, t is time, $\mathbf{E}$ is the electric field strength, $\mathbf{B}$ is the magnetic field, and $\mathbf{v}$ is the velocity of the particle. $\mathbf{p}$ is the momentum of the electron, which can be expressed as:

$$\mathbf{p} = \gamma m_e \mathbf{v} \tag{2.12}$$

where m_e is the electron rest mass, and γ is the Lorentz factor. From equation 2.11, it can be seen that there are two components to the Lorentz force that are responsible for the motion of the electron: there is the electric field component $-eE$; and the magnetic field component $ev \times B$. If the velocity of the electron is relatively low, such that $v \ll c$, then we can largely discount the influence of the $\mathbf{B}$ component of the Lorentz force. If we have an infinite, plane wave propagating through a vacuum, then a free electron will experience a force in one direction with the first half of each cycle of the electric field, and then on the returning half-cycle will experience an equal force in the opposite direction. This force results in the electron oscillating in space with each cycle of the plane wave, however it will always return to its initial starting position, and as such the net momentum of the electron is zero over time. If however, the electron velocity is large and is a significant fraction of c, then the magnetic field component of the Lorentz force which acts in the longitudinal direction will become important, and will in the case of a linearly polarised laser field will result in the electron adopting a figure-of-eight type motion, albeit still with no net transfer of momentum.

Introducing a useful parameter, known as the normalised laser amplitude, as being:

$$a_0 = \frac{eE_0}{m_e c \omega_L} = 0.85\sqrt{\frac{I\lambda^2}{1.37 \times 10^{18} W cm^{-2}}} \tag{2.13}$$

can aid in this description of the motion of the electron. This allows these two distinct regimes that our laser-plasma interaction can operate under to be properly defined. If $a_0 \ll 1$, then the interaction is said to be operating in the non-relativistic regime, which occurs when the electron velocity is a small fraction of c and the motion of the electron is primarily governed by the electric field component of the laser. If $a_0 \geq 1$, then the interaction is said to be in the relativistic regime, which as we will see later in section

2.6, can result in the properties of the plasma becoming significantly modified, where v is a significant fraction of c and the influence of the magnetic field component of the laser rapidly becomes important. The laser intensity at which this transition occurs, can be seen to be $I_L > 1.37 \times 10^{18}$ Wcm^{-2} for 1 micron laser light by considering the Poynting vector, which is the energy flux density, time averaged (denoted by $\langle\rangle$) over the fast oscillations of the laser field, defined as:

$$I_L = \left\langle \left| \mathbf{E} \times \frac{\mathbf{B}}{\mu_0} \right| \right\rangle = \frac{\epsilon_0 c}{2} E_0^2 \tag{2.14}$$

2.4.2 The ponderomotive force

In reality, it is not a simple plane wave that the electrons encounter, but a pulse of laser light which has both a temporal and a spatial profile. In order to understand how this changes the dynamics of a charged particle, we shall now consider the motion of an electron in a laser field with a Gaussian spatial intensity profile. As we discussed before, the force that a charged particle experiences in a non-relativistic laser field is primarily governed by the magnitude and direction of the electric field, which for a simple plane-wave results in the particle always returning to its starting position at the end of each cycle of the electric field. However, in reality a laser pulse does not have a flat spatial intensity profile, but at focus typically has a Gaussian profile. In terms of the influence this has on electron motion, this means that on the first half of the laser cycle an electron in this laser field will be pushed away from the region of highest laser intensity at the centre of the laser beam as before, but on the return cycle the electron will experience a lower magnitude returning force, due to now being in a region of lower laser intensity out at the edges of the laser focus. Over time this results in a net force expelling electrons transversely away from the centre of the laser beam. This resultant force is known as the "ponderomotive force", which is described in Gibbon *et al.* [49] as the "time averaged gradient of the electron oscillation". The non-relativistic form of this force can be expressed as:

$$F_p = \frac{e^2}{4 m_e \omega_L^2} \nabla E^2 \tag{2.15}$$

As the laser intensity increases, and a_0 becomes > 1, then the relativistic form of the ponderomotive force becomes important. Through using the normalised light amplitude parameter a_0 as defined previously in equation 2.13, the relativistic form of the ponderomotive force can be expressed as:

$$F_p = -m_e c^2 \nabla \sqrt{1 + a_0^2/2} = -m_e c^2 \nabla \gamma \tag{2.16}$$

As the electron is ejected from the centre of the laser focal spot, it has an energy $E_p = (\gamma - 1) m_e c^2$, and due to the influence of the magnetic field, is now ejected at an angle relative to the perpendicular direction.

2.5 Plasma

In section 2.3, the processes responsible for the ionisation of a material by a high power laser were covered, which act to create a plasma. A plasma can be described as a quasi-neutral gas of charged and neutral particles which exhibit collective behaviour [50, 51], and is often referred to as being the "fourth state of matter". This definition tells us that, on a macroscopic scale, a plasma can be considered to have an overall neutral electric charge, and that the motion of any one charged particle within the plasma will directly influence the motion of nearby particles through the formation of electromagnetic forces, therefore exhibiting a "collective behaviour".

There are typically three criteria which must be satisfied in order for an ionised gas to be considered a plasma: $\omega_p > \omega_c$ - the plasma frequency ω_p, which is the characteristic frequency at which the electrons in the plasma oscillate around their equilibrium position, must be higher than the frequency at which collisions between the electrons and other particles occur; $L \gg \lambda_D$ - the spatial dimensions of the plasma must by greater than the Debye length, λ_D, so that the plasma can be considered to be quasi-neutral; and finally $N = (4/3)\pi\lambda_D^3 \gg 1$ - the number of particles in the Debye sphere, an area of space with radius equal to the Debye length, must be high enough so that any changes to the electrostatic potential in one region of the plasma will be screened out, and will not influence the charge of the overall bulk plasma [52].

In the case of short-pulse laser plasma interactions, plasmas are typically described by the properties of the plasma electrons, often using parameters such as the plasma electron density, n_e, plasma electron temperature, T_e, or $k_B T_e$, and plasma electron frequency, ω_p. The reason that it is the electrons which primarily determine the parameters used to describe a plasma and not the ions, is due to the fact that the charge-to-mass ratio of the ions is so much smaller than that of the electrons, and therefore the time they take to respond to any changes in the electrostatic potential is very much greater than that of the electrons. If we consider the placement of a positive test charge within a plasma, the surrounding electrons will respond to this change in the electrostatic potential very quickly, surrounding the test charge and shielding it from the rest of the plasma, before the ions can have a significant response. This means that under typical conditions, the ions can be considered to be immobile, and the properties of the plasma will be primarily influenced by the electrons.

Considering an ion within a plasma, the Coulomb potential, V_c of this ion will decrease exponentially with distance, such that:

$$V_c(r) = \frac{Z}{4\pi\epsilon_0 r} \exp\left(-\frac{r}{\lambda_D}\right) \tag{2.17}$$

where Z is the charge state of the ion, ϵ_0 is the permittivity of free space, r is the distance from the ion, and λ_D is the Debye length. The Debye length is defined as the distance over which the Coulomb potential drops by $1/e$, where e is Eulers number [53], and can be described in terms of the density, n_e and the temperature, T_e of the electrons in the plasma, where:

$$\lambda_D = \sqrt{\frac{\epsilon_0 k_B T_e}{n_e e^2}} \tag{2.18}$$

From this, it can be seen that the Debye length is proportional to $\sqrt{T_e}$, meaning that as the temperature of the plasma electrons increase, their oscillations grow in magnitude and the shielding effect on the charge of the ion decreases, allowing the Coulomb potential of the ion to reach further into the plasma. Additionally, it can be seen that as the number of electrons in the plasma, i.e. the plasma density increases, more electrons become available to screen the charge of the ion from the rest of the

plasma, reducing the reach of this Coulomb potential.

Another important parameter in a plasma is the plasma frequency. When an electron is displaced from its equilibrium position within an electrostaticaly-neutral plasma, it will be subjected to a restoring force due to the formation of a charge separation, which acts against its motion. Upon returning to its starting position, the electron will overshoot the point of equilibrium resulting in it experiencing a restoring force in the opposite direction [54,55]. This causes the electron to oscillate around this equilibrium position, and it is the frequency of this oscillation that is known as the plasma frequency, ω_p. This plasma frequency is dependent on the electron density of the plasma, such that:

$$\omega_p = \sqrt{\frac{e^2 n_e}{\epsilon_0 m_e}} \tag{2.19}$$

When describing the motion of the plasma electrons in the context of the interaction between a plasma and an ultra-intense laser pulse, as we will later in section 2.7, the plasma electrons gain significant energy from the laser. In this scenario, the velocity at which the electrons are moving becomes so great that it approaches a significant fraction of c, and as such the behaviour of the electrons become relativistic. This means that the effective mass of the electrons begins to increase, and therefore it becomes necessary to consider the relativistically-corrected plasma frequency, which is given by:

$$\omega_p = \sqrt{\frac{e^2 n_e}{\epsilon_0 \gamma m_e}} \tag{2.20}$$

where $\gamma = \left(1 - \frac{v^2}{c^2}\right)^{-1/2}$ is the Lorentz factor.

The plasma frequency, and its transition into the relativistic regime, is a parameter which is of great importance when describing the transparency of a plasma to an incident laser, as will be discussed in section 2.6, and is key to many of the more complex mechanisms that occur during laser-plasma interactions. These mechanisms will be discussed further in section 2.10.

2.6 Electromagnetic wave propagation in plasma

The plasmas that we are considering in this thesis have a sufficiently high plasma electron density to be considered "overdense". This description refers to a property of the plasma known as the "critical density", which is the plasma density at which the plasma frequency, ω_p, and the laser frequency, ω_L, are equal. If the plasma density is greater than this value, and the electrons in the plasma have an oscillation frequency greater than the laser frequency, then the plasma becomes opaque to the laser light preventing its propagation. We can see how this arises by considering the dispersion relation:

$$\omega_L^2 = c^2k^2 + \omega_p^2 \tag{2.21}$$

where k is the wavenumber. For a plasma that is at critical density, such that the laser and plasma frequencies are equal, we can see that the wavenumber must drop to zero, meaning that the plasma becomes reflective and prevents the propagation of the laser. Using this condition and equation 2.20, we can define this critical density as:

$$n_c = \frac{\gamma m_e \epsilon_0 \omega_L^2}{e^2} \tag{2.22}$$

From the dispersion relation we can also derive this in terms of the refractive index of the plasma:

$$n = \frac{c}{v_p} = \frac{ck}{\omega} = \sqrt{1 - \frac{\omega_p^2}{\omega_L^2}} \tag{2.23}$$

where v_p is the phase velocity. From this we can see that if the plasma frequency is greater than the laser frequency, then the refractive index becomes imaginary, causing the laser to be reflected from the critical destiny region, or "critical surface". A plasma which meets this criterion is considered to be overdense, whereas if the plasma frequency is less than the laser frequency, then the plasma is referred to as being under-dense, and appears transparent to the laser light. It is important to note, however, that even in the case of an over-dense plasma, the laser can penetrate a short distance into the plasma before its electric field decays exponentially to zero. As shown in equation 2.20, as the velocity of a plasma electron increases to a significant fraction of c, then

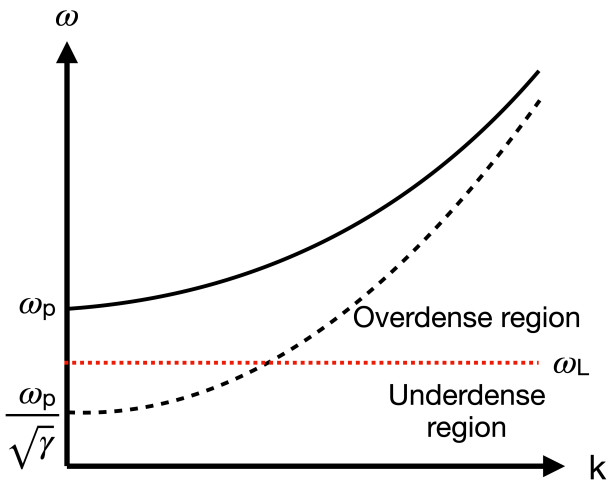

Figure 2.5: Plot showing the dispersion relation for an electromagnetic wave in a plasma, with the solid black line depicting the non relativistic case, and the dashed black line the relativistic case. The influence of the gamma factor acts to reduce the plasma frequency below the laser frequency (shown as the red dashed line), enabling the laser to propagate through a region of plasma that would otherwise be opaque.

the electron mass, and therefore plasma frequency become modified by the Lorentz factor. This is the reason why γ is included in equation 2.22, and means that as the electron velocity, and therefore the Lorentz factor increases, the electron density at which the plasma is considered to be overdense is increased. The consequence of this is that, as the motion of the plasma electrons becomes increasingly relativistic, then the critical surface at which the laser is reflected occurs at a higher plasma density. If we consider the density of the plasma to follow a gradient from solid density at the surface of the target material, down to vacuum some distance away from the front surface, as described in the previous section, then it follows that the position of the critical surface, where $\omega_p = \omega_L$, will lie somewhere on this density gradient. As the density required for the plasma to become overdense increases due to the relativistic motion of the electrons, then the critical surface will occur deeper into the plasma density gradient, allowing the laser to propagate further into the plasma than it would otherwise be able to. A plot of the dispersion relation depicts this in figure 2.5. If the target is sufficiently thin, then this enhancement of the penetration of the laser into the plasma can become sufficiently significant that the target becomes transparent to the peak of the laser pulse, allowing

the laser light to propagate all the way through [56–58]. This process which allows the laser to propagate through a region of plasma which would classically be considered to be overdense is known as relativistic induced-transparency, and much research has been carried out looking to utilise this as a means of boosting the particle energies that can be achieved [59]. This phenomenon will be discussed further in section 2.10, as well as in chapter 5.

2.7 Laser-plasma absorption mechanisms

As discussed previously in section 2.4.1, an electron oscillating in a plane wave does not gain any net energy, as each time it is displaced by the first half of the cycle of the wave, the second half of the cycle will return it to its starting position. Consequently, net energy gain averaged over a laser period in an infinite plane wave is not possible, as summarised by J. D. Lawson in the so-called "Lawson-Woodward theorem" [60]. This theorem states that the net energy gain of an electron interacting with an electromagnetic field in vacuum is zero, assuming that the laser field is in vacuum with no walls or boundaries present, no static electric or magnetic fields are present, the region of interaction is infinite, and ponderomotive effects are neglected. This means that in general, in order to impart a net energy gain into the electron, one or more of these conditions must be broken so that the restoring action of the laser is inhibited, preventing the electron from returning to its initial position. As discussed in section 2.4.2, the ponderomotive force is one way that the restoring action of the second half of the laser cycle can be broken. However this can also occur when a medium such as a plasma is present.

As such, we will now discuss some of the mechanisms by which the laser energy can be transferred into the electrons of a plasma, as this is critical for the production of the high energy particles needed for any potential application. There are a variety of different mechanisms responsible for the absorption of the laser into the plasma, and each of these will become more dominant or less dominant depending on the particular laser and target parameters being used. Absorption mechanisms can largely be grouped

into two broad categories: collisionless absorption mechanisms, such as resonance absorption, vacuum heating, and $\mathbf{j} \times \mathbf{B}$ heating; and collisional absorption mechanisms, such as inverse-bremsstrahlung absorption.

2.7.1 Collisional absorption mechanisms

For plasmas where the mean free path of the electrons is less than the spatial dimensions of the plasma, the plasma can be considered as being collisional, as there are a significant number of collisions that occur between the plasma electrons and the ions. This is the case for laser-solid interactions involving a relativity low laser intensity of $< 10^{15}$ Wcm^{-2}, where the primary collisional absorption mechanism that occurs is known as inverse-bremsstrahlung absorption. This process is where electrons accelerated by the laser field collide with other electrons or ions in the plasma, and in the process absorb a photon of light. This absorption raises the energy of the free electrons, leading to heating of the plasma. The frequency at which these collisions occur, v_{col}, is given by:

$$v_{col} \propto \frac{n_e Z}{T_e^{\frac{3}{2}}} \tag{2.24}$$

For the laser systems being discussed in this thesis however, the peak laser intensities are typically well in excess of 10^{18} Wcm^{-2} and therefore the plasma temperature that is reached is sufficiently high that this collision frequency is low [61, 62]. Therefore, in this case the transfer of energy from laser to plasma is dominated by collisionless mechanisms, although some collisional absorption may still occur in the low intensity wings of the laser focus [63].

2.7.2 Resonance absorption

The first absorption mechanism to be mentioned is known as "resonant absorption" [64]. This mechanism occurs when an incoming p-polarised laser is incident at an angle oblique to the target, and reflects from the angle-modified critical surface, given by $n_\theta = n_c \cos^2\theta$. This modification of the point of reflection arises by adding the angle

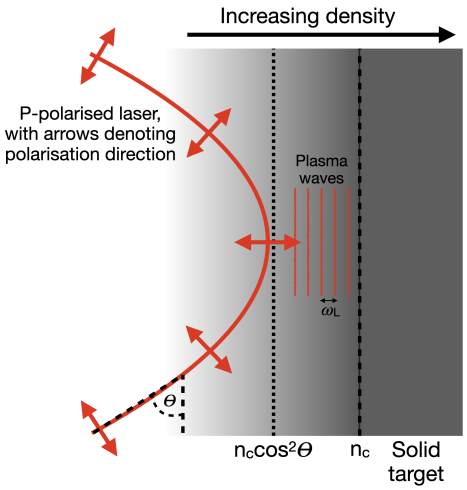

Figure 2.6: Schematic showing a depiction of resonance absorption, where the laser is incident at an angle θ on to a target with a long density scale-length, and undergoes reflection at the density surface $n_\theta = n_c \cos^2\theta$. Plasma waves, shown by the vertical red lines, are generated by the oscillation of the laser in the plasma, eventually driving electrons across the critical surface.

of incidence to the k-vector of the laser, such that:

$$k_y = \left(\frac{\omega_L}{c}\right) \sin\theta \tag{2.25}$$

Following this, the dispersion relation can rewritten as:

$$\omega_L^2 = c^2 k_x^2 + \omega_p^2 + \omega_L^2 \sin^2\theta \tag{2.26}$$

The laser is reflected when $k_x^2 < 0$, and $n_e > n_c \cos^2\theta$, and at this point of reflection, the polarisation direction of the laser is perpendicular to the direction of the plasma density gradient, as shown in figure 2.6. The oscillating electric field of the laser thus acts to resonantly drive waves in the plasma, pushing electrons further into the density gradient. Eventually, typically over many cycles, the plasma oscillations will have grown sufficiently that the electrons are pushed past the critical surface of the plasma and into the region of over-dense plasma. Here, the electric field of the laser becomes evanescent and subsequently the restoring force experienced by the electrons becomes very much weaker, preventing them from being pulled back by the laser and resulting

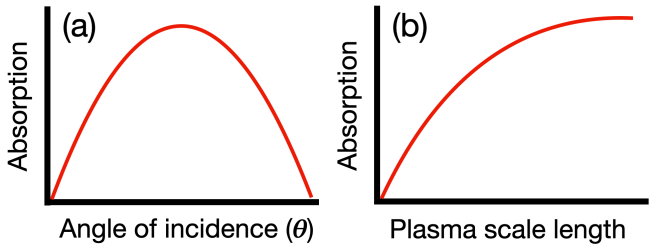

Figure 2.7: Illustrations showing the approximate scaling of resonance absorption with angle of laser incidence (a), and plasma scale length (b).

in them being ejected into the dense plasma at or below the laser frequency. This mechanism requires the plasma to have a long density scale length relative to the laser wavelength, and typically dominates as the primary laser absorption mechanism for laser intensities of between 10^{12} Wcm^{-2} and 10^{17} Wcm^{-2}, as below this intensity the electron energies are low and therefore collisional absorption dominates, and above this range the relativistic effects of the interaction become more dominant [65–68]. Under these conditions, resonant absorption can achieve absorption of the laser into the plasma electrons with an efficiency of up to 50% [69]. Approximate scalings of resonance absorption with angle of laser incidence and plasma scale length are illustrated in figure 2.7.

2.7.3 Vacuum heating

Similarly to resonant absorption, vacuum heating, also known as Brunel heating, occurs when a p-polarised laser is incident on a target at an angle [70]. The primary difference is that, unlike resonant absorption, vacuum heating occurs in plasmas with a very short density scale-length relative to the amplitude of the electron oscillation. In this case, electrons are pulled away from the front surface of the plasma into vacuum by the first half of the laser cycle, and then the returning part of the cycle directly drives the electrons across the critical surface, and out of the influence of the vast majority of the returning force of the laser. An illustration of this is shown in figure 2.8. Vacuum heating is most efficient when the laser is at a 45° angle of incidence, such that the combination of the incident and reflected waves maximise the electron field component

that is normal to the surface of the target [71].

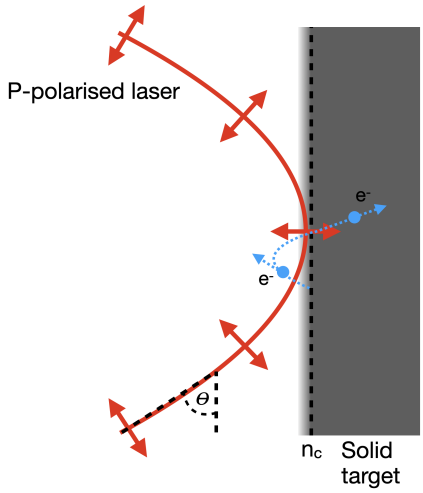

Figure 2.8: Schematic showing a depiction of vacuum heating, where an obliquely angled laser light is incident on a target with a density scale-length which is short relative to the amplitude of the electron oscillation. Electrons are pulled off the surface of the plasma and into vacuum in one half-cycle of the laser, before being pushed directly across the critical surface by the next half-cycle. A representation of this electron motion is shown in blue.

2.7.4 JxB heating

As seen in section 2.4.2, when operating in the relativistic regime, the motion of the electrons becomes driven primarily by the quickly oscillating $\mathbf{v} \times \mathbf{B}$ component of the Lorentz force which acts to drive electrons in the direction of laser propagation. This $\mathbf{v} \times \mathbf{B}$ force acts on the plasma electrons until they are eventually pushed past the critical surface, transferring the energy from the laser into the plasma at twice the laser frequency. Due to the longitudinal component of the relativistic ponderomotive force, $\mathbf{J} \times \mathbf{B}$ heating is most effective when the laser light is incident at normal incidence to the target, unlike resonant absorption and vacuum heating which requires the laser to be at an angle to the target [72]. Another difference is that unlike the other mechanisms, $\mathbf{J} \times \mathbf{B}$ heating will occur with both a p-polarised and s-polarised laser, whereas with resonance absorption and vacuum heating only p-polarised light will work. Circularly polarised light, however, will not lead to $\mathbf{J} \times \mathbf{B}$ heating, the reason for which can be

seen by expressing the ponderomotive force in equation 2.16 as:

$$F_p = -\frac{e^2}{4m_e\omega_L^2}\nabla E^2\left(1 - \frac{1-\epsilon^2}{1+\epsilon^2}\cos 2\omega_L t\right)\hat{x} \tag{2.27}$$

where ϵ is the degree of ellipticity in the polarisation of the laser and $\hat{x}$ is the propagation direction [49,66,73]. In the case where the laser light is circularly polarised, $\epsilon = 1$, and so the second term in equation 2.27 vanishes and the quickly oscillating component of the ponderomotive force does not occur.

Each of these laser absorption mechanisms play an important role in the interaction between a laser and a plasma depending on the laser parameters. However for most of the work covered in this thesis, $\mathbf{J} \times \mathbf{B}$ heating will be the dominant mechanism.

2.8 Front surface plasma expansion

As previously described in section 2.3, the irradiation of a target by a high-intensity laser pulse causes the material to be rapidly ionised and heated, forming a hot plasma which quickly expands due to thermal pressure out into vacuum, away from the target front surface. This region of plasma in typically referred to as a "pre-plasma", and its formation is one of the key parts of the interaction of the laser and the target, as many of the mechanisms responsible for the transfer of energy from the laser into the plasma are dependent on this feature, as will be discussed in section 2.7. The expansion of this preplasma can be quantified by using a parameter known as the plasma scale length, L, such that the density profile of the expanding plasma drops off exponentially as:

$$n_e(z) = n_0 \exp(-\frac{z}{L}) \tag{2.28}$$

where n_0 is the initial electron density, and z in the distance from the front surface of the target. The plasma scale length is therefore defined as the distance over which the electron density drops by 1/e, where e is Euler's number, and a "short" scale length typically refers to this distance being smaller than the laser wavelength, and a "long" scale length usually refers to it being larger. This scale length can also be approximated

by considering the laser pulse duration, τ_L and the ion acoustic velocity, c_s, so that,

$$L \approx c_s \tau_L \tag{2.29}$$

The ion acoustic velocity, c_s is the approximate speed of expansion of this preplasma, and can be defined as,

$$c_s = \sqrt{\frac{k_B(ZT_e + T_i)}{m_i}} \tag{2.30}$$

where Z is the effective charge state, k_B is the Boltzmann constant, T_e and T_i are the electron and ion temperatures, and m_i is the ion mass [74, 75].

2.9 Electron temperature scaling

As we have seen in section 2.7, the laser acts to cause considerable heating and acceleration of the electrons in the plasma. This produces a population of forwards-propagating "fast electrons", resulting in a strong, mega-ampere electron current. The energies of these fast electrons will typically cover a large range of values, but will lie in a Maxwellian distribution for lower laser intensities [76], and a two-temperature Maxwell-Juttner distribution when dealing with relativistic laser intensities. Typically, the fraction of the laser energy that is coupled into the electrons is in the region of 20-40% [77–79], and the average energy of these fast electrons, also known as the fast electron temperature, is denoted by T_e. There are a wide variety of different functions which help describe the scaling of the fast electron temperature with respect to laser intensity, such as that which is described in Beg *et al.* [80], that which is in Wilks *et al.* [65], and that which is from Chen *et al.* [78]. The scaling function derived in Beg *et al.* comes from experimental measurements of γ-ray emission, and shows that the hot electron temperature scales as:

$$k_B T_e = 215 \left(I_{18} \lambda_{\mu m}^2\right)^{\frac{1}{3}} \tag{2.31}$$

where I_{18} is the intensity of a 1 μm laser in units of 10^{18} Wcm^{-2}. The scaling in Wilks *et al.* comes from an analytical model, and describes the hot electron temperature scaling as

$$k_B T_e = 511 \left(\sqrt{1 + 0.73 I_{18} \lambda_{\mu m}^2} - 1 \right) \tag{2.32}$$

Finally, the scaling function in Chen *et al.*, which like the Wilks function comes from experimental observations, is given as:

$$k_B T_e \propto (I_L \lambda_L^2)^{0.34} \tag{2.33}$$

In each these cases, the fast electron temperature scales with $I_L \lambda_{\mu m}^2$ despite being derived in different ways. There are various other studies that have been carried to try and determine this fast electron temperature scaling, but it remains an extremely difficult task to get an accurate measurement of the fast electron temperature experimentally, and obtain a definitive scaling law. This is due to the fact that the current methods for measuring the temperature of the hot electrons, or the temperature of specific regions within the plasma, are often limited in the range of electron energies that they can resolve, or depend on time-integrated measurements. Probing the temperature of the electrons in the plasma within a specific region of the plasma, such as the region of laser focus, and within the time-frame of the pulse duration, poses a complex challenge, and will be visited further in chapter 4.

2.10 Laser propagation in a plasma

So far the relevant mechanisms whereby energy is transferred from the laser into the solid target, ionising it and forming a plasma have been discussed. As the plasma is heated, it undergoes thermal expansion, dropping the density of the bulk plasma, until eventually the plasma becomes underdense and the remaining part of the laser can freely propagate through. However, there are numerous mechanisms by which the optical response of the plasma can be altered by the high intensity nature of the interacting light, forming a channel, or aperture, through the high-density plasma.

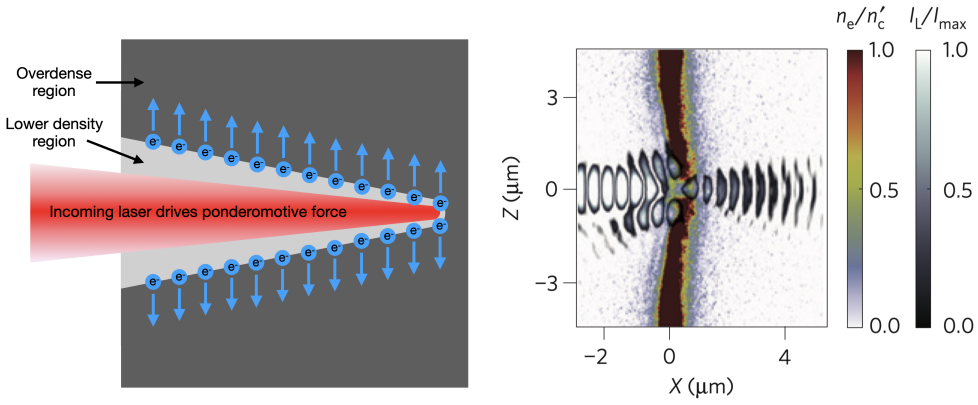

(a) (b)

Figure 2.9: (a) Illustration of the expulsion of electrons, where the ponderomotive force acts to drive electrons transversely away from the centre of the beam, reducing the electron density and enabling the continued propagation of the laser. (b) Particle-in-cell simulation showing the laser intensity and plasma electron density, as the laser propagates from left to right. An aperture consisting of underdense plasma can be seen, allowing the laser to propagate through. [84]

2.10.1 Ponderomotive plasma channelling and aperture formation

In section 2.4.2 we described the ponderomotive force, and how it acts to eject electrons away from the high intensity region at the centre of the laser beam. As the laser propagates through the plasma, this force acts to expel electrons out of the way of the pulse, reducing the plasma electron density and therefore the plasma frequency as per equation 2.20. An illustration of this is given in figure 2.9(a). As described in section 2.6, this reduction of the plasma frequency will enable the laser to propagate further into the plasma that it otherwise would have been able to, helping to form a channel through the plasma [81–83].

Also mentioned previously in section 2.6, is the process of relativistic induced transparency, where the strongly relativistic nature of the electron motion leads to the plasma frequency dropping sufficiently that the laser can propagate all the way through the target and out the other side. This leads to the formation of an aperture through the overdense region of the plasma, inside of which is filled with underdense plasma. This formation of a plasma aperture can be seen in figure 2.9(b), as reported in Gonzalez-Izquierdo *et al.* [84], which shows a particle-in-cell simulation of a laser propagating

through an aperture in a dense plasma. The properties of this plasma aperture can have significant implications of the behaviour of the transmitted laser light, as will be discussed further in chapter 5.

Chapter 3

Methodology: Lasers, diagnostics and simulations

In this chapter, some of the key technologies and techniques that are employed in the high power pulsed laser systems used in this thesis will be discussed, followed by an overview of the three laser systems employed in the measurements presented in chapters 4, 5, and 6. A description of some commonly used target designs will be given, as well as an overview of the use of a diffuse scatter screen, which is a key diagnostic tool used in the experimental work discussed in chapters 4 and 5. Finally, the particle-in-cell simulation method that is used in this thesis, along with some of the other modelling techniques are discussed.

3.1 Key laser technologies and techniques

3.1.1 Chirped-pulse amplification

One of the most important developments in pulsed laser technology that has occurred since the first demonstration of the laser [2], is the development of a method of laser amplification known as chirped-pulse amplification (CPA) [5], which enabled a significant increase in the focused laser intensities that were able to be achieved. This method of laser amplification helped overcome the main limitations in laser design at the time,

which was the formation of large B-integrals and heat in the amplifying materials. The B-integral is a parameter that denotes a measure of the nonlinear phase shift of light, and is related to the nonlinear effects such as self-focusing and filamentation that occur as a high-intensity laser propagates through a material, and is defined as:

$$B = \frac{2\pi}{\lambda_L} \int_0^L n_2 I_L(z) dz \tag{3.1}$$

where n_2 is the nonlinear coefficient of the refractive index of the material the laser pulse is propagating through, I_L is the laser intensity, and L is the propagation distance through the media. As the development of these laser systems progressed, and the energies achieved grew ever higher, the magnitude of these nonlinear effects rapidly became a limiting factor in any further increase of laser intensity, as when left unchecked, they can cause significant damage to the optics in the amplifier chain and breakup of the near field spatial-intensity distribution of the laser beam. The advent of chirped-pulse amplification in 1985 allowed for a significant increase in the laser energies that were able to be achieved without damaging the optics in the laser chain, and allowed for the peak laser intensities brought onto the target to be pushed well into the relativistic regime ($> 10^{18}$ Wcm^{-2} for a laser wavelength of 1 micron).

This process of laser amplification helps prevent the formation of adverse nonlinear optical effects which can arise when the B-integral is high, by taking the short input laser pulse from the initial stages of laser amplification and adding dispersion, often by passing it through a pair of diffraction gratings, before the damage threshold of the optics is reached, a schematic of which is shown in figure 3.1. These two diffraction gratings act as a temporal pulse-stretcher, stretching the laser pulse in time by a factor of 10^3 to 10^5, therefore causing a significant drop in the power further down the amplifier chain. This stretched, lower intensity pulse is then passed through a series of amplifier stages, bringing the fluence back up to just under the damage threshold for the amplifying materials, before being passed through a second pair of diffraction gratings with an opposite direction of dispersion as the first. This second grating pair acts to recompress the high energy, temporally-stretched pulse back down to a similar

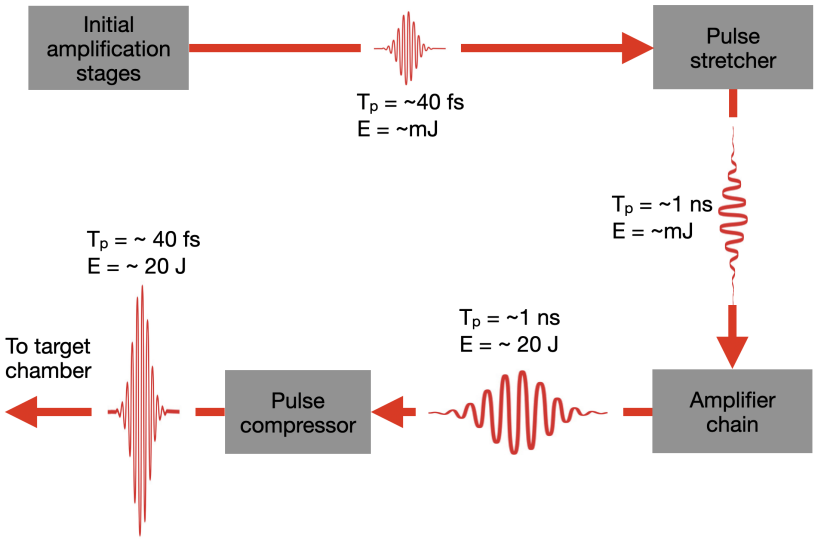

Figure 3.1: Illustration of chirped-pulse amplification (CPA). Numerical values are for illustration purposes only.

pulse length as the original input pulse, leading to a dramatic increase in the peak intensity, which is now well above that which would have been able to be safely propagated though any amplifying material. The remaining parts of the laser chain which bring this beam into the target chamber, and onto the target, therefore usually have to use turning and focusing mirrors, rather than lenses, due to the high B-integrals that would otherwise be generated.

3.1.2 Optical parametric chirped-pulse amplification

A disadvantage of CPA is that it is typically done together with multi-pass amplification, which requires multiple passes through the gain media in order to reach the intensities required, and as such has a tendency to cause significant amplification of spontaneously emitted light (ASE), as will be discussed in section 3.1.3. This can result in the generated pulses from a CPA system having issues with regards to poor laser temporal-intensity contrast, which is the signal-to-noise ratio of the peak intensity of the pulse, relative to the background intensity of light (usually quoted at a particular time before main pulse arrival). This can be extremely problematic for laser-solid experiments, as will be explored in section 3.1.3.

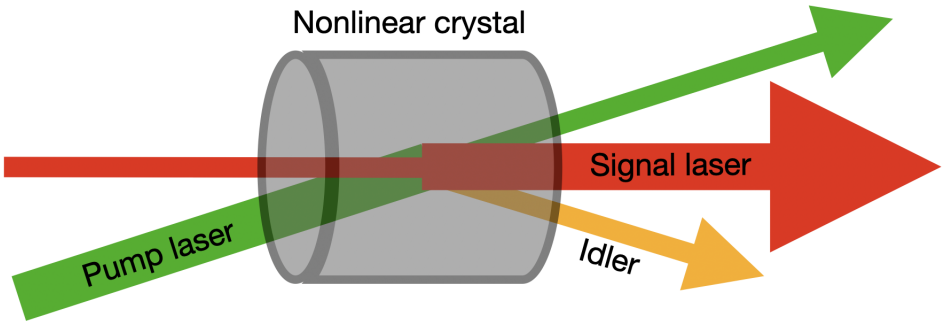

Figure 3.2: Illustration of optical parametric chirped-pulse amplification. A lower frequency signal beam is passed through a nonlinear crystal along with a higher frequency pump beam. Energy is transferred from pump to signal, and a third beam, the idler, is produced.

One technique that can be employed to somewhat mitigate this, is optical parametric chirped-pulse amplification (OPCPA) [85], which is a technique of laser amplification that exploits the nonlinear properties of certain crystalline materials, such as lithium niobate ($LiNbO_3$) and β-barium borate (β-BaB_2O_4) [86–89]. Through one of these crystals, the low-intensity seed that is to be amplified is propagated, along with a higher intensity, and higher frequency, pump beam, which may come from a conventional CPA amplification system [90]. As these two beams pass through the nonlinear crystal, energy is resonantly transferred via optical parametric amplification from the high intensity pump beam to the lower frequency signal beam, providing amplification with a high gain of $\sim \times 1000$. Due to conservation of energy, a third beam, the idler, is also produced such that $\omega_{pump} = \omega_{signal} + \omega_{idler}$. A schematic of this is shown in figure 3.2.

This process relies on the pump beam and signal beam being phase-matched in order to produce significant amplification, meaning that any additional noise in the system, such as the ASE, is not amplified due to the efficiency of energy-coupling to non phase-matched components being low. Additionally, because there is no need for gain materials to be pumped with high energies in order to drive a population inversion of the electrons, there is significantly less heat generated in the optical components of the system. This means that the likelihood of components becoming damaged is

significantly reduced, and the repetition rate of the laser system can be increased, as time is not needed to wait for gain media to cool.

3.1.3 Laser temporal-intensity contrast and plasma mirrors

Low laser temporal-intensity contrast ($< 10^8$) can be extremely detrimental to the running of an experiment, as any significant intensity of laser light irradiating the target early in time, prior to the arrival of the main pulse, can result in the target becoming prematurely deformed, ionised, or even destroyed. One mechanism that can cause low laser temporal intensity contrast, as briefly mentioned previously, is ASE. The laser systems employed in the experiments reported in this thesis, use flash-lamp pumped glass amplifiers as part of their amplification process, which operate on a much longer timescale than the laser pulse. This means that the glass amplifiers become energised many nanoseconds prior to the main pulse arriving. During this time, energised electrons in the amplifier medium will spontaneously decay and produce photons, which in turn can induce stimulated emission of more photons within the gain medium, some of which be emitted along the central axis, and can therefore travel further down the laser chain. This results in a certain amount of background light to be present in the amplifiers, which needs to be filtered out in order to prevent it from propagating all the way down the laser chain and destroying the target, as even this ASE light can reach intensities of $> 10^{12}$ Wcm^{-2} when focussed. This temporal filtering is often done by using Pockel cells, which act as shutters at the end of the amplifier cavity, preventing any light from escaping prematurely. However, when the Pockel cell opens to allow the main pulse of light to leave the amplifier cavity, some of this background light will also leave. This can result in the main pulse sitting on top of a "pedestal" of background light, which can often extend several nanoseconds before and after the arrival of the peak of the pulse. In addition, any unwanted leaks or reflections from optical components can sometimes propagate down the laser chain producing so called "prepulses", which can arrive at the target prior to the main pulse. Therefore, if either the ASE pedestal or the prepulses are of sufficient intensity to ionise the target, then target can undergo significant heating and expansion before the main

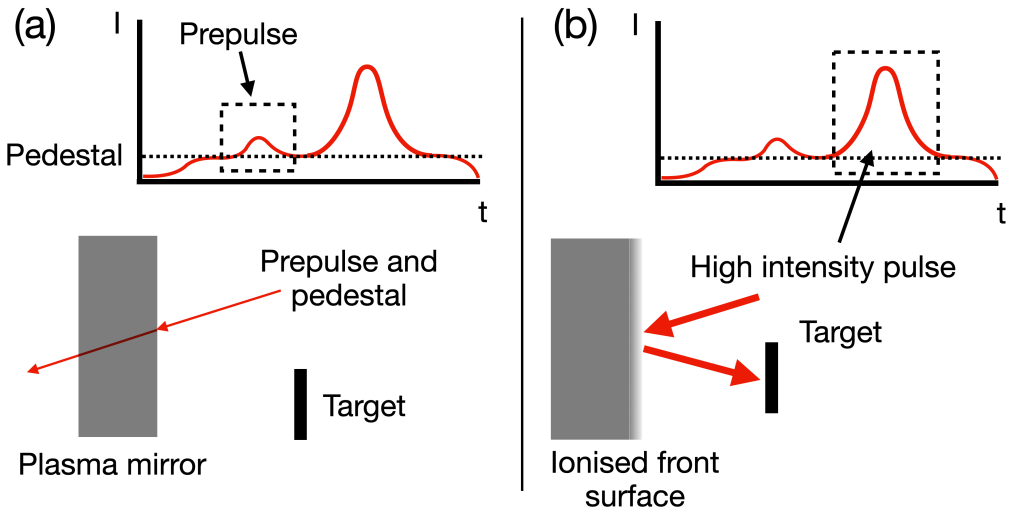

Figure 3.3: Schematic of the principle of operation of a plasma mirror as a tool to improve the temporal-intensity contrast of a laser. (a) The majority of the low intensity ASE component of the laser pulse is transmitted through the plasma mirror. (b) The rising edge of the high intensity main pulse irradiates the plasma mirror, ionising its front surface, and reflects from this plasma onto the target.

pulse arrives, complicating the dynamics of the interaction.

A commonly employed technique to improve the temporal-intensity contrast between the main laser pulse and the ASE pedestal or any prepulses, is the use of a plasma mirror [91–93]. These optics are placed prior to the target in the path of the beam and reflect the laser light onto the target. They are typically made of glass, and as such are highly transparent ($\sim 4\%$ reflectivity) at the central wavelength of the laser [94]. As the pedestal or any prepulses irradiate the plasma mirror, the light is of a sufficiently low intensity that it does not ionise the mirror surface, and the majority ($\sim 96\%$) of the light passes through the transparent optic, reducing any premature irradiation of the target. However, as the rising edge of the main pulse arrives, the intensity becomes high enough ($> 10^{13}$ Wcm^{-2}) that the front surface of the plasma mirror rapidly ionises, forming a reflective overdense plasma, as discussed in section 2.3. This causes the main pulse to be reflected onto the target, separating it out from the background ASE light or any prepulses, a schematic of which is shown in figure 3.3. However, losses in the plasma mirror results in typically only around 70% of the

main pulse being reflected [92], but despite the loss in energy, this intensity-gating of the main laser pulse can result in a significant boost in the temporal-intensity contrast between the peak of the laser and the background ASE or prepulse, allowing for the target to remain mostly preserved until the arrival of the main pulse. This is of particular importance when utilising targets with microstructured front surfaces, such as those described in section 3.3.1 and investigated in chapter 4, as these structures are extremely sensitive to premature deformation from heating by any light preceding the main pulse. On such experiments, often multiple plasma mirrors are employed, placed in series to further boost the contrast of the laser up to 10^{11} - 10^{12} [95]. More recently, new designs of plasma mirrors with ellipsoidal geometries have been employed to provide additional focussing of the laser onto the surface of the target, as well as improving the temporal-intensity contrast of the pulse [94, 96, 97].

3.2 High power laser facilities

Over the last 30 years, there has been a rapid increase in the intensities of laser light that can be achieved, and scientific interest in the field of ultra-intense laser-plasma interactions has increased significantly. As such, there has been a significant growth in the number of laser facilities around the world capable of producing these ultra-intense laser pulses. For this thesis, we will focus on the three following laser facilities: the PHELIX laser at GSI Helmholtzzentrum für Schwerionenforschung, in Darmstadt, Germany, the Gemini laser at the Rutherford Appleton Laboratory (RAL) in the UK, and the Vulcan Petawatt laser, also located at RAL.

3.2.1 PHELIX GSI

The petawatt-power class laser, PHELIX, located at GSI, is a flashlamp-pumped Nd:glass laser that can deliver around 200 J before the compressor, which compresses the pulse duration down to $\sim$ 500 fs FWHM before irradiating the target. A schematic of the laser system can be seen in figure 3.4. The PHELIX laser is seeded by a femtosecond oscillator which produces a train of 100 fs pulses, each with around 4 nJ of energy.

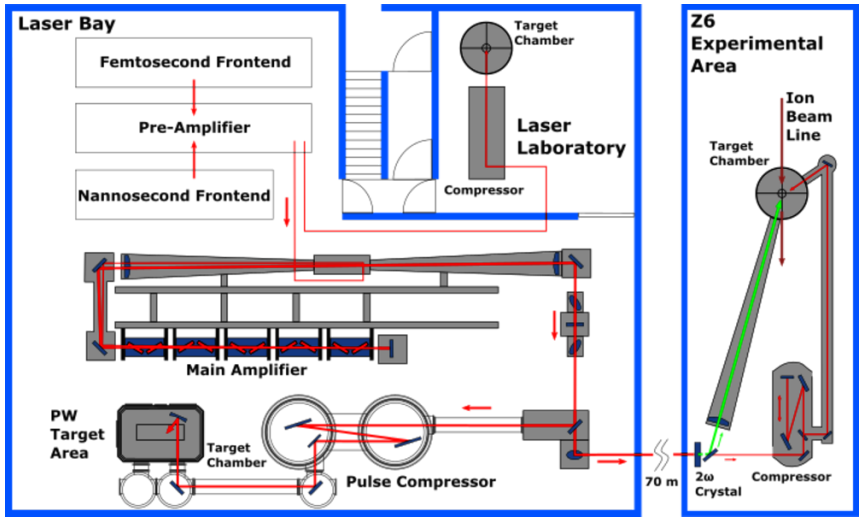

Figure 3.4: Overview of PHELIX laser, and petawatt target area [98]. Credit: GSI.

These are then passed through an optical parametric amplifier, bringing the pulse energies to around 100 μJ as well as allowing some degree of pulse cleaning to prevent the ASE from the initial stages of laser generation from being further amplified.

This pulse train, operating at 10 Hz, is then passed through a pulse stretcher prior to being amplified by both a linear, and a ring regenerative amplifiers, bringing the energies up further to $\sim$ 30 mJ. Next, one of the pulses is transported into the main amplifier hall, which consists of five flashlamp-pumped Nd:glass amplifier cassettes, arranged in a double-pass configuration. This brings the pulse energy up to around 250 J, but results in a significant cool down period of approximately 90 minutes being required for the subsequent shot. After amplification, the pulse is passed into the compressor, which uses two optical gratings in single-pass configuration to compress the pulse duration back down to $\sim$ 500 fs before it is passed into the target area. Here, it passes through a series of steering mirrors before finally being focused down onto the target by a f/1.5 off-axis parabolic mirror (OAP), forming a focal spot of around $\sim$ 4 μm in diameter (FWHM), and at a central wavelength of 1053 nm [98].

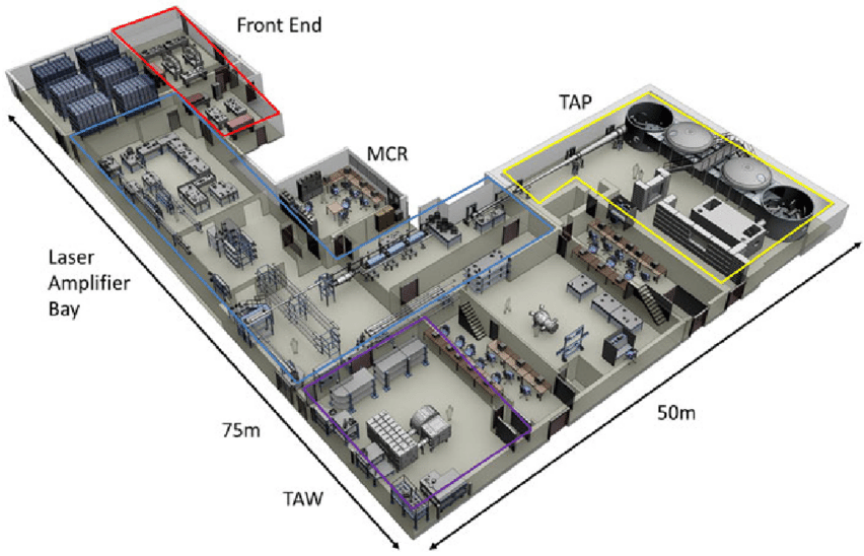

Figure 3.5: Schematic of overview of Vulcan laser system, with the petawatt target area highlighted in yellow. Credit: CLF. [99]

3.2.2 Vulcan

The Vulcan laser is also a petawatt class laser system. The laser system begins with an oscillator which produces a train of $\sim$ 200 fs pulses each with a few nanojoules of energy, one of which is then gated out and passed through a pulse stretcher, increasing its pulse duration to $\sim$ 3 ns. Next, the pulse enters the first stage of amplification, which is OPCPA system, before it passes through the pulse stretcher for a second time, bringing the pulse duration up to 4.8 ns. The pulse then passes into the main amplifier area, which consists of a series of flash-lamp driven rod and disk amplifiers. This brings the energy of the pulse up to $\sim$ 600 J, but similarly to the PHELIX laser, requires a significant cooldown time of around 90 minutes between subsequent shots. After being amplified, the pulse is compressed to $\sim$ 500 fs, before being focused onto the target by a f/3.1 OAP. This results in on-target intensities of $\sim 5 \times 10^{20}$ Wcm^{-2} with a focal spot diameter of $\sim$ 4 µm and a central wavelength of 1053 nm [99]. A schematic of the Vulcan laser is shown in figure 3.5.

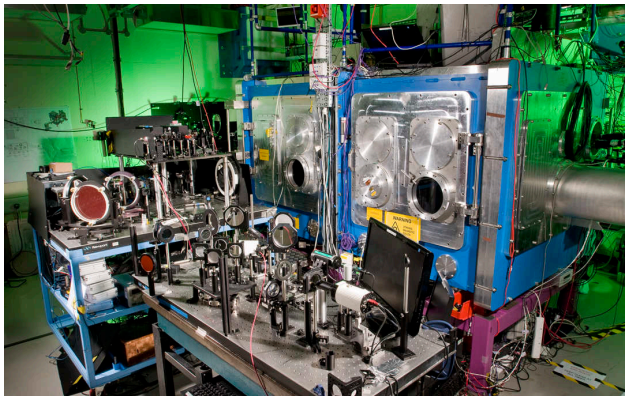

Figure 3.6: Photograph of Gemini target chamber. Credit: STFC.

3.2.3 Gemini

The final laser system that will be discussed is the Gemini laser, which is also located at the Central Laser facility [100]. Similarly to the previous systems, the laser starts with an oscillator producing a train of $\sim$ 500 mJ pulses each with a pulse duration of around 12 fs (FWHM), which are then stretched to around 500 ps by a pulse stretcher. The pulses are then passed through the various amplifying stages, which in the case of Gemini comprise of Ti:Sapphire based amplifiers, rather than the Nd:Glass based design of Vulcan and PHELIX. This provides the amplifier with a large gain bandwidth [101] so that a large range of laser frequencies to be amplified, allowing for much shorter pulses to be produced during compression. As a result, the output pulses are of around 40 fs in duration, with a central wavelength of 800 nm, and deliver $\sim$ 15 J before compression. A photograph of the Gemini target chamber is shown in figure 3.6. Another key difference of Gemini compared to the other laser systems, is that it can operate at a much higher repetition rate, and is able to produce a full power shot once every 20 seconds, rather than once every $\sim$ 90 minutes.

3.3 Targetry

There are a wide variety of different target materials and designs used during experiments, including gasses, aerogels, and foams. However in this thesis we are investigating laser interactions employing solid density targets, which are often thin metal foils or

plastic targets. The targets being discussed are typically a few millimetres in transverse dimensions, and have a thickness ranging from as low as 10 nm up to hundreds of microns. These targets are often mounted on a stalk, which in turn is connected to the rest of the target mounting apparatus, such as a multi-axis translation stage, to allow for precise alignment between the target and the focal spot of the laser. A schematic of a simple flat foil target mounted on a target stalk is shown in figure 3.7(a). The target stalks are frequently made from metal, but more recently, plastic target stalks have become desirable, as they provide two advantages: first, plastic allows for the target stalks to be quickly produced in large numbers via 3D printing, which is important as the repetition rate of laser systems becomes increasingly higher; and secondly, the plastic helps to reduce the generation of strong electromagnetic pulses (EMP) produced during the laser-target interaction. The generation of this EMP during the interaction occurs due to the strong charge separation produced in the plasma, which draws a significant return current up the metal target stalk in order to neutralise the charge of the plasma [102–104]. This EMP field can be of sufficient magnitude that it disrupts the operation of any electronic equipment that is being used to measure the interaction, negatively affecting the measurements or even permanently damaging the equipment. Therefore, significant research has been carried out to look at ways of minimising the EMP field generated, such as using plastic target stalks as mentioned, or more intricate stalk designs such as coils and helical-shaped posts [105].

Developments in high power laser technology are enabling modern laser facilities to operate at higher shot repetition rates, with hundreds, or even thousands of shots potentially being taken in a single day. This poses a huge challenge for experiments involving solid-density targets, as manufacturing that many targets is difficult, let alone being able to align, shoot, and then replace each one quickly enough. This means that the typical target design of a single foil mounted on a stalk for each laser shot is no longer viable, and so novel designs of solid targets are being developed to address this problem. Some of these new target designs include ideas such as having an array of a relatively large number of targets mounted on a frame, such as that depicted in figure 3.7(b), with the x-y-z positions for the alignment of each individual target preprogrammed, allowing

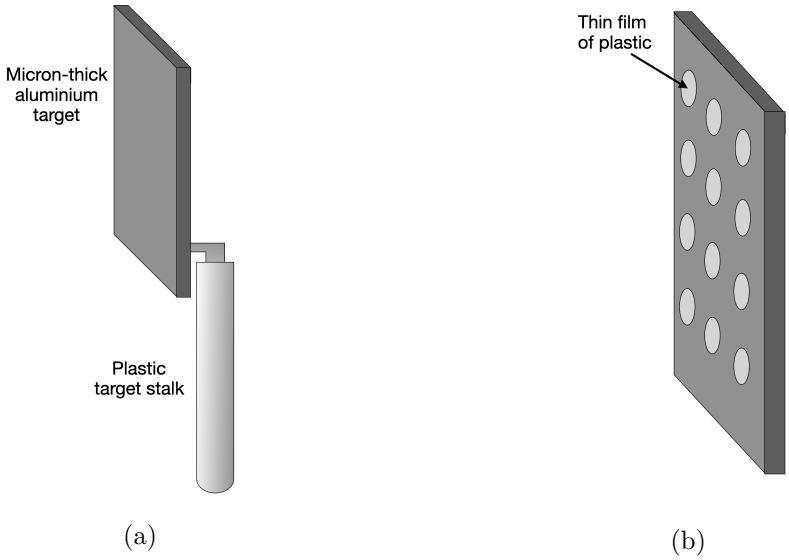

Figure 3.7: Schematics of some typical target mounting designs. (a) Aluminium foil target, mounted on top of a plastic stalk. (b) Array of ultra-thin plastic foils, often of around a few tens of nanometers in thickness, held in place by a supportive frame.

the system to automatically scan through each target position in quick succession as each shot is taken [106]. With a target design such as this, it is likely that precautions would need to be taken to protect each target from debris as the adjacent targets are irradiated, which could potentially be addressed by manufacturing the array of targets such that each one has a shroud surrounding it, to act as a shield against any potential debris from hitting it. One issue that is often encountered when aligning solid targets is the positional accuracy that is needed to place the target at the focus of the laser, as even a small shift of a few microns in the direction of the laser propagation can result in a significant reduction of the laser intensity of the surface of the target. One target design that has been tested which aims to increase the possible repetition rate, as well as potentially the stability of the alignment shot-to-shot, is a continuous tape drive much like a VHS tape, which can be shot at a high rate as it is driven along. This has an advantage over using multiple individual targets, as there is minimal realignment needed in-between shots, and so the tape can simply be driven at a constant speed, allowing for very high repetition rates to be achieved [107].

3.3.1 Microstructured targets

As we have seen in section 2.7, the energy of the laser is transferred into the target as the laser propagates through the underdense region of plasma on the front surface and is absorbed, before the remaining light is reflected from the plasma critical surface and lost. It follows from this, that in order to maximise the degree of absorption of the laser into the plasma, it can be beneficial to engineer ways of reducing the reflectivity of the target, therefore reducing the loses due to reflection. One way of

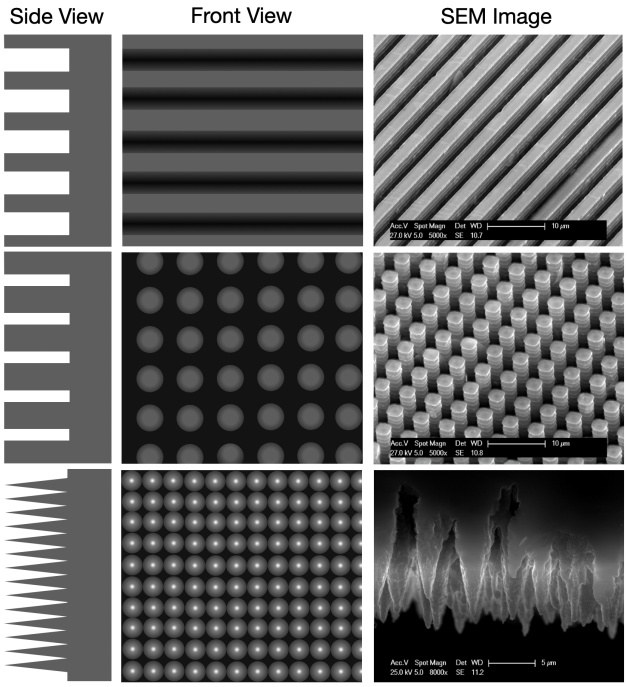

Figure 3.8: Schematics of a variety of microstructured target surfaces. Laser-etched grooves, pillars, and needles are shown top, middle and bottom respectively, with side view, front view, and images taken via scanning electron microscope (SEM) shown left, middle, and right respectively. SEM images courtesy of Institut für Kernphysik, Darmstadt.

doing this is to use targets which have a microstructured front surface, such as grooves, nanowires [108], microbeads [109], or needles, along with many others. Schematics of a few examples of microstructured targets are shown in figure 3.8, which will be investigated further in chapter 4. As the target is irradiated, the structuring on the front surface acts to increase the effective surface area of the target due to the laser

undergoing multiple reflections as it travels down to the bottom of the microstructures, increasing the probability for the light to be absorbed. This results in a significant reduction in the amount of light lost due to reflection compared to a flat-surfaced target, and has been shown to provide a significant enhancement to laser absorption and X-ray and particle flux [95]. In addition, previous research has demonstrated that the microstructures on the surface of the target can act to strongly modify the local electromagnetic fields and guide the accelerated electrons between the structures and into the base of the target, narrowing their angular distribution. This process could also potentially lead to increased heating of the plasma, and a subsequent increase in laser absorption [108]. Fabrication of these microstructured targets can be done through a variety of methods, such as electrochemical etching [110], electron beam lithography [111], chemical vapour deposition [112], and via laser-etching [113].

3.4 Diffuse scatter screen

The results to be discussed in this thesis consist of spatial and spectral measurements of the laser light, as it either is reflected from, or transmitted through the target. As such, a brief description and overview will be given of the diffuse scatter screen imaging technique that was used to obtain the results presented in chapters 4 and 5.

Diffuse scatter screens are a useful tool for capturing light escaping from the target during irradiation by the laser pulse, so that the spatial-intensity distribution of the light can be imaged. It is also a very versatile imaging technique, and can be easily used to image light as it is specularly reflected from, diffusely scattered from, emitted from, or transmitted through the target, with very little change in the required equipment needed. These scatter screens are made from a material that diffusely scatters light as it is incident on the screen, such as ground-glass or polytetrafluoroethylene (PTFE), an example image of which is shown in figure 3.9. This diffuse scattering of the light means that precise angular alignment of the screen and imaging cameras is not required, allowing for much more freedom in the placement of the equipment, which is beneficial when dealing with target chambers consisting of numerous other diagnostic equipment.

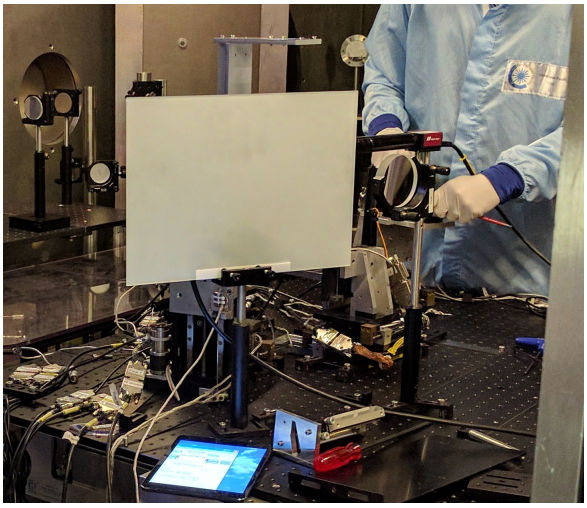

Figure 3.9: Photograph of a ground-glass scattering screen, as used for imaging the specularly-reflected light in chapter 4.

With appropriate placement of the scatter screen, the light expands up to fill the screen as it propagates from the target, preserving the spatial profile of the light as it does so. This means that by imaging the spatial-intensity distribution of the light as it is reflected from, or transmitted though the target, information can be obtained relating to the spatial properties of the target, since any spatial structuring of the reflective target surface, or the plasma through which the laser is propagating, modulates the distribution of the light. This is the key principle behind the experimental measurements made in the first two experimental chapters, and so will be discussed in more detail there. In addition to providing a measurement of the spatial changes in the light, the scatter screen diagnostic can also be used to obtain information about the energy content of the light that is incident on the screen, and by observing changes in this measured intensity shot-to-shot, some useful insight can be gained into changes occurring in the reflectivity or transmission of the target, depending on what is being imaged. This can be used to provide an estimate of the total laser absorption into the plasma, although complications can arise due to light being scattered from other objects and surfaces within the target chamber, and adding to the light on the screen that is being imaged. Significantly more robust measurements can be made by using techniques such as employing the use of an Ulbricht sphere [114].

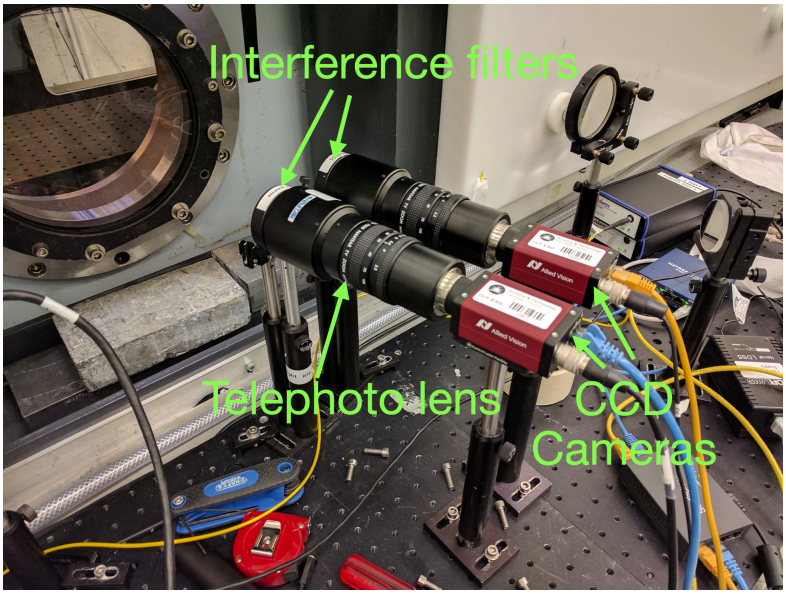

Figure 3.10: Photograph showing CCD cameras with telephoto lenses and interference filters as used for imaging a scatter screen through a window in the target chamber.

In order to image the light scattered by these screens, CCD cameras are typically used to capture a time-integrated image (usually in the ms range) of the spatial-intensity distribution of the light on the screen. Using zoom lenses allows for the cameras to be placed relatively far away outside the target chamber, as long as line-of-sight to the scatter screen can be achieved through a window in the chamber wall. This is of great benefit when imaging light during the most high-intensity laser interactions, since as mentioned in section 3.3, EMP can cause significant issues for electronic equipment placed close to the interaction.

When imaging the light captured by a scatter screen, it is often desirable to restrict the bandwidth of the the detected light to filter out the light generated during the interaction, and ensure that it is only the laser light, whether being reflected or transmitted, that is being imaged. This is typically done by using bandpass, or interference filters, which have a high degree of transmission ($\sim 50\% - 95\%$) at the desired wavelength of light, but are largely opaque over the rest of the spectrum. In addition, it can be useful to have a second camera with an interference filter to select for the second harmonic of the laser light, as shown in figure 3.10. Imaging this 2ω light can be used to gain

valuable insight into the dynamics of the reflective plasma surface during interaction with the peak of the laser pulse, as this is the location, and point in time, at which this light is typically produced [115]. An application of measuring this second harmonic light will be discussed further in chapter 4.

3.5 Simulation and modelling techniques

In this section, a description will be given of the particle-in-cell simulation technique, and some of the other modelling methodologies that are used throughout the analysis in chapters 4, 5, and 6. Due to the complexity and cost of designing, setting up, and then running experiments involving high power laser systems, as well as the time required, extensive simulation work is usually undertaken in order to prove the viability of the proposed investigation, as well to give some affirmation to the results that are obtained. There are a variety of different simulation models that are used in the laser-plasma community, such as kinetic particle-in-cell (PIC) models [116], fluid models [117], and models which are a hybrid of the two. In this thesis however, the focus will be on kinetic PIC models, specifically one such code, the Extendable Particle-in-cell Open Collaboration (EPOCH) [118].

3.5.1 EPOCH

EPOCH is a numerical modelling tool which models the kinetic properties of the particles, grouped into macroparticles, rather than modelling the overall bulk properties of the plasma as is the case with the hydrodynamic simulation techniques. This kinetic approach allows for PIC simulations to model the dynamics of each of these macroparticles, as well as how the electric fields are created and modulated by the motion of these particles. PIC simulations are particularly suited to modelling the intense laser-solid interactions being investigated in this thesis, as they can model the rapidly evolving particle motions that occur over femtosecond timescales, whereas other simulation approaches, such as the hydrodynamic codes, tend to be best suited to running over much longer nanosecond timescales.

As a PIC simulation progresses, the movement of each charged particle needs to be calculated. The motion of these particles is governed by the Lorentz force, as discussed in section 2.4.1, and the relevant equations of motion can be expressed as:

$$\frac{dr}{dt} = v \tag{3.2}$$

where r is the position, v is the velocity, and t is time, and

$$\frac{du}{dt} = \frac{q}{m}(E + v \times B) \tag{3.3}$$

where $u = \gamma v$, $\gamma = (1+(u/c)^2)^{1/2}$, E is the electric field strength, and B is the magnetic field, and:

$$\frac{\partial B}{\partial t} = -\nabla \times E \tag{3.4}$$

and

$$\frac{\partial E}{\partial t} = c^2 \nabla \times B - \frac{j}{\epsilon_0} \tag{3.5}$$

where j is the current density and ϵ_0 is the permittivity of free space. When the simulation is initialised, the particles are distributed onto a coordinate grid system with the desired spatial distribution, and a variety of starting parameters, such as charge state, electron and ion temperatures, and electron number density, in order to define the target. The initial motion of each particle is determined using equations 3.2 and 3.3, and the current density in each grid-cell can be calculated from the flux of particles crossing each grid boundary. This allows for the EM fields to be updated using equations 3.4 and 3.5, which can in turn be used to recalculate the new particle velocities by reusing equations 3.2 and 3.3. This allows the simulation to progress by running these calculations in a loop, progressing through each time step [119]. A flow diagram of the operation of a PIC code is shown in figure 3.11. The resulting equations for the updated electric and magnetic fields are as follows:

$$\frac{E^{n+3/2} - E^{n+1/2}}{\Delta t} = c^2 \nabla \times B^{n+1} - \frac{j^{n+1}}{\epsilon_0} \tag{3.6}$$

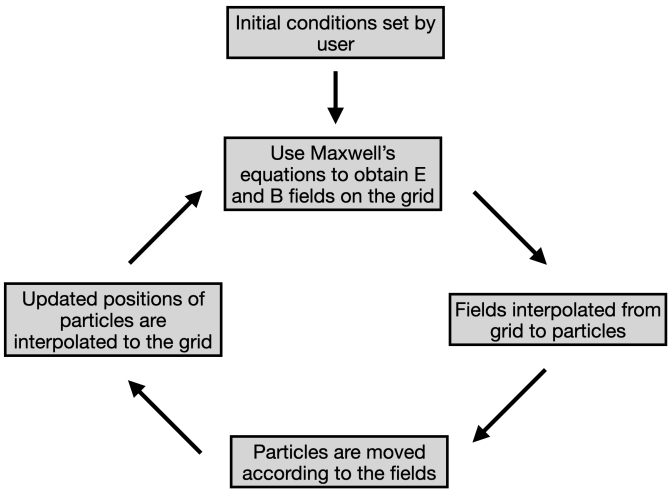

Figure 3.11: Flow diagram of the operation of a PIC simulation. The initial conditions, including the distribution of the particles are set by the user and are loaded into the simulation. From this particle distribution, the EM fields are calculated using Maxwell's equations, and then used to move the particles accordingly. The new particle positions are then used to recalculate the fields, completing the loop, which then moves forward to the next time step.

$$\frac{B^{n+1} - B^n}{\Delta t} = -\nabla \times E^{n+1/2} \tag{3.7}$$

where Δt is the time step between iterations. As long as $\nabla \cdot B = 0$ at the start of the simulation, then only the Maxwell–Faraday equation and the Ampère's circuital law of Maxwell's equations need to be included, since Gauss' Law of magnetism will remain true throughout the simulation [118].

PIC simulations are an extremely useful tool for the study of laser-plasma interactions, particularly when considering solid density targets, and have become an integral part of investigations that are conducted in this field of research. Although they are capable of modelling the complex physics of these interactions with a high degree of accuracy, they are not without their limitations.

One of the main complications with using the PIC approach to simulate the laser-plasma interactions, is the computational power that is often required. In order to ensure that the simulation is as representative as possible of what is being modelled, a large number of particles is required, potentially reaching into the hundreds of thou-

sands. The motion of each of these particles due to the presence of the laser field has to be calculated, as well as the fields that are generated by the motion of the particles themselves, and this vast number of calculations has to be computed, and recomputed many thousands of times throughout the duration of the simulation. Depending on how many spatial dimensions are simulated, and the spatial resolution that is required to obtain the desired results, the required computational resources for PIC simulations can vary by an enormous degree. Some of the more simple simulations are able to be run very quickly in a matter of minutes on a desktop computer or laptop, but as the spatial resolution and number of spatial dimensions that are modelled increases, the hardware needed can very quickly scale up to necessitating the use of large-scale cluster computing, with potentially hundreds of hours being needed to complete the simulation. This is often exacerbated by the fact that these simulations often do need to be run with a high, nanometer spatial resolution, thereby increasing the computing resources required, in order to mitigate an effect known as numerical self-heating [116, 120]. This self-heating is due to numerical inaccuracies that can occur when running PIC simulations if the spatial resolution is too low, and results in the plasma gaining thermal energy even without a laser pulse being present. This arises due to the spatial resolution being larger than the Debye length, resulting in the electric fields becoming aliased across neighbouring cells, and the artificial heating of the plasma until the Debye length becomes resolved. This can result in the plasma undergoing more thermal expansion than it should during the simulation, which in turn can have a significant impact on the calculations of other mechanisms such as laser absorption, for example.

As well as having these limitations, there are a few assumptions that PIC codes have to make. The primary assumption made is that collisions between particles in the plasma are usually discounted, thereby allowing for the assumption that the plasma is entirely collisionless. Most of the time this assumption is not particularly problematic as long as care is taken to ensure that the resolution of the simulation is set high enough, and the Debye length is therefore resolved. In some circumstances, however, this can cause issues such as an exaggerated growth of the magnetic fields due to collisional dissipation not being accounted for. Recently, additions have been made

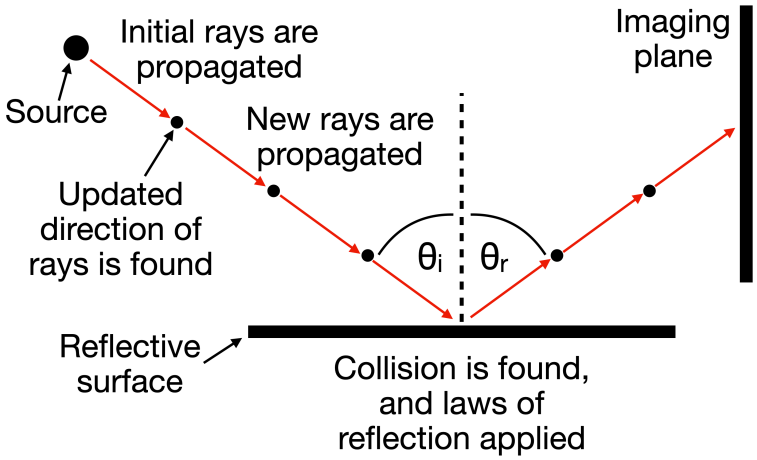

Figure 3.12: Schematic showing the basic principles of a ray tracing model, where a source emits an initial bundle of rays and the direction of propagation is iteratively updated, until reaching the boundary of the simulation. Upon collision with a reflective surface, the laws of reflection will be applied.

to EPOCH that allow for particle collisions to be included in the calculations [121], allowing for effects such as Bremsstrahlung radiation to be modelled, albeit at increased computational cost.

3.5.2 Ray-tracing modelling

A useful method for modelling the propagation of light, is the use of ray tracing techniques, such as the Zemax software [122]. Ray-tracing is used in the analysis in chapters 4 and 5, and so a brief overview of the basic principles is given here.

Ray tracing is a modelling method whereby the light emitted by a source is assumed to be comprised of a number of narrow rays, which are allowed to propagate for some distance in a straight line. Then, depending on the physical properties of any medium that the rays are propagating through, such as the refractive index, approximate solutions to Maxwell's equations are found, and new rays are generated with an updated direction. This process is then repeated until the ray leaves the confines of the simulation area, or reaches a predefined imaging plane. If, during propagation, the ray collides with an object that has been added to the model, such as a reflective surface,

then the appropriate behaviour of the ray is calculated, such as applying the laws of reflection to the path it takes. A schematic depicting this is shown in figure 3.12, where θ_i is the angle of incidence, and θ_r is the angle of reflection. Following from this, more complex transmissive and reflective structures can be added to the ray tracing model, for example, to build an understanding of how light interacts with microstructures on the front surface of a target, or how the spatial-intensity distribution of a laser focal spot is modified after passing through an aperture, as will be discussed in the following chapters. These rays can then be collected at an imaging plane set some distance away, producing an image of the spatial-intensity distribution of the light.

Chapter 4

Diagnosing plasma electron temperature and laser focal size via analysis of specularly-reflected light from microstructured solid targets

4.1 Introduction

In this chapter, experimental results and modelling that demonstrate spatial structuring in the intensity-distribution of the light specularly reflected from microstructure targets during irradiation by a high intensity laser will be investigated. These results are then used to develop a novel method for diagnosing the temperature of the plasma electrons, localised spatially to the region of the focal spot and temporally to the peak of the interaction. In addition to this, the influence that the irradiating focal spot size relative to the size and spacing of the target structures has on the reflected light spatial structure is also investigated, highlighting the potential to use this approach to diagnose the size of the laser focus on high intensity laser shots. Both of these parameters are key

to the physical processes that occur during the interaction between the laser pulse and the overdense plasma, as plasma temperature will influence the motion of the particles and the energies that can be achieved. Furthermore, the size of the laser focal spot will influence the peak intensity achieved, and give insight into which regime of particle acceleration is dominant.

There are currently a variety of methods that have been developed to measure the temperature of the plasma electrons, as well as photons that are generated in intense laser-solid interactions. These methods usually involve measuring spectra through use of diagnostics, such as electron and ion energy spectrometers [123], stacked dosimetry film [124] or by using nuclear activation techniques [125]. Although these methods are useful for measuring the temperature of the particles emitted out of the target, measuring the temperature of the plasma as it is irradiated by an intense laser and rapidly heated is often significantly more complex, and usually requires the measurement of the ratio of intensities of discrete X-ray emission lines [126, 127]. Methods such as this can provide a measurement of the temperature of the plasma, but are rather limited in that they typically only provide a measure of the temperature of the overall bulk plasma, as they involve taking a spatially-averaged measurement of the X-ray emission. Although still useful, this method is not able to resolve the plasma temperature specifically within the region of laser focus, and at the moment in time of peak laser intensity on target, which is the point in space and time that is of the greatest interest when considering how rapidly the plasma dynamics evolve within the laser focus. Diagnosing the plasma temperature specifically within this spatially localised region of the laser focus, near the critical density surface of the plasma, i.e. the laser-plasma interaction region, and also at a time limited to the laser pulse interaction time, remains a very difficult task to achieve. Achieving this, however, would provide a useful tool when conducting high-power laser experiments.

As well as measuring the front surface temperature of the plasma within the region of laser focus, another property that is challenging to measure is the on-shot laser focal spot size. This is of particular significance for tightly focussed geometries, i.e. small f-number focusing, where the divergence of the beam before and after focus is large,

and even a small shift in the position of the focal spot along the laser propagation direction can have a significant impact in the focal spot size, and subsequently the intensity. Measurements that are made of the focal spot size are typically made at low power, and are not necessarily representative of the focussing conditions during a full power shot, as various thermally-induced aberrations in the laser amplifiers, or laser self-focussing as the beam propagates through the preplasma can drastically alter the size and quality of the focal spot interacting with the front of the target. Being able to make this measurement during a full power shot would add confidence that the focal spot size being measured was representative of the focal conditions experienced by the target on a data shot, and would also help in more accurately determining the intensity. This is of particular importance when investigating physical processes that scale non-linearly with intensity, such as ultra-thin targets undergoing relativistic self-induced transparency, a process which is extremely sensitive to the laser intensity and where having a more reliable measurement than the typical method would greatly aid the experiment. In addition, laser scientists developing new laser systems are continuously looking to increase the laser intensities that can be achieved [128, 129], and one way of achieving this can be by employing tighter focussing geometries in their design. Tight focusing geometries however, are sensitive to small changes in the collimation of the laser beam [94, 97], and thus more robust focal spot measurements would be highly advantageous.

4.2 Concept of diagnostic

Before covering the specific details of the experimental analysis and modelling, a brief description of the concept that is being discussed in this chapter will be given, with a schematic shown in figure 4.1. A solid target with a microstructured front surface is irradiated by a high power laser pulse, and the specularly reflected light is collected on a scatter screen placed some distance away, in this case 50 cm. As well as the laser light, the scatter screen will also collect second harmonic light that is generated at the plasma critical surface. As the target is ionised by the laser, and the plasma heated, the

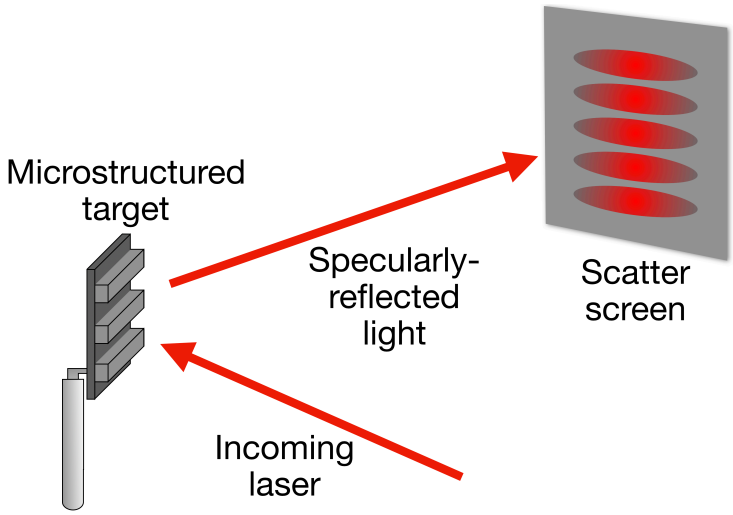

Figure 4.1: Schematic showing an overview of the concept being discussed in this chapter. A target with a microstructured front surface is irradiated, and the specularly reflected light captured on a scatter screen, displaying structure in the spatial-intensity profile of the measured light.

structures on the front surface will start to deform and the spaces between them will fill with plasma, resulting in the spatial profile of the plasma critical surface to transition from the step-like profile of the cold target, to a more sinusoidal profile. This in turn will cause the distribution of the reflected laser light and generated light on the scatter screen to vary. Since the second harmonic light is being generated during a period of time which encompasses only the irradiation of the target by the highest intensity part of the pulse, measuring this frequency of light temporally restricts the target conditions being probed to the time at which the peak of the pulse is incident on the target surface. The resulting measurements of the spatial-intensity profile of the second harmonic light captured on the scatter screen, therefore contain information relating to the spatial profile of the plasma critical surface at the point in time of the generation of this light. By firstly modelling how the spatial profile of the structures, in this case the depth of the grooves, varies as a function of plasma electron temperature measured at a fixed time, i.e. the incidence of peak laser intensity, and secondly, modelling how this variation in the profile of the structures influences the spatial intensity distribution of the light collected on the scatter screen, a model can be formed which relates the

plasma electron temperature at peak laser intensity to the spatial profile of measured light.

4.3 Experimental configuration

The experimental data that will be discussed were measured during an experiment using the Vulcan petawatt laser system, discussed in section 3.2.2, which was investigating the use of microstructured targets as a means of increasing the degree of absorption of the laser energy into the target compared to just using a flat foil, and enhancing the resulting particle energies. More information about this experiment is available in Ebert *et al.* [95]. As mentioned in section 3.2, the Vulcan laser is a petawatt-class laser which produces pulses of light with a FWHM of 500 - 1000 fs and central wavelength of 1053 nm. In this case, after focussing from an F/3 off-axis parabolic mirror, the laser was reflected from two plasma mirrors consecutively in order to improve the temporal intensity contrast significantly, and help prevent the microstructures on the targets from being prematurely destroyed, as discussed in section 3.1.3. An overview of the experimental arrangement that was used is shown in figures 4.2(a) and (b). This configuration resulted in laser pulses with energy (160 ± 30) J focused to a spot diameter of $\sim$7 μm FWHM, which are incident onto a target mounted at an angle of 20° to the target normal, and the resulting laser intensity is subsequently calculated to be $(5 \pm 0.5) \times 10^{19}$ Wcm^{-2}.

Four types of microstructured target were tested on the experiment, with each microstructure being present on the front surface of silicon targets. The structures that were used, which are illustrated in figure 4.2(c) were: flat silicon foils to act as a reference; silicon foils with parallel grooves etched into their front surface; silicon foils with both vertical and horizontal grooves etched into their front surface, forming pillar-like structures; and silicon foils with conical, needle-like structures. The groove and pillar-like targets were produced via laser etching whereas the needle targets were produced at the Detector and Target Laboratory, at the Technical University of Darmstadt, using repetitive femtosecond laser pulse irradiation in a sulphur hexafluoride

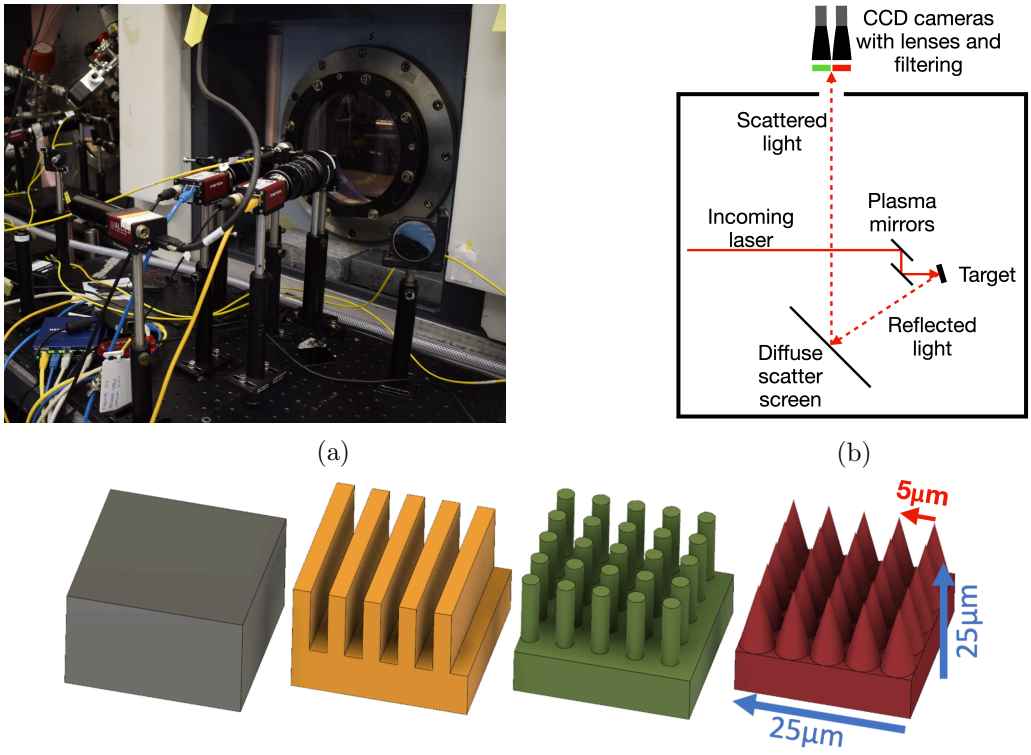

Figure 4.2: (a) Photograph of CCD cameras looking into the target chamber, with zoom lenses and filtering, in order to image the 1ω and 2ω light specularly reflected onto the diffuse scatter screen. (b) Schematic showing the path of the incoming laser beam (solid red line), from the double plasma mirrors onto the target front surface. The specularly reflected light and scattered light is denoted by the dashed red lines, and the diffuse scatter screen and imaging cameras are shown. (c) Schematic illustrating the four types of targets employed, here after referred to as; From left to right: flat foil, grooves, pillars and needles.

environment [130]. This fabrication method is described in reference [131]. The pillar and groove targets were all made from 25 μm-thick silicon wafers with the structures etched into front surface, so that the resulting target comprised of 15 μm-high structures sitting on top of a 10 μm-thick base. The pillar structures had a 3 μm diameter, and were arranged in a grid with one pillar every 5 μm, and similarly the groove structures had a width of 2 μm and were spaced every 5 μm.

In order to determine if these microstructured targets were indeed providing an enhancement to the laser absorption, the intensity of laser light that was specularly

reflected from the front surface of the target, i.e. the unabsorbed light, was measured by means of capturing it on a diffuse scatter screen scatter screen, as described in section 3.4, and imaging with lenses and CCD cameras. The scatter screen that was used was a pane of ground-glass placed 50 cm from the target, which acts to diffusely scatter the laser light incident on its surface, allowing for the spatial-intensity distribution to be easily imaged. This imaging was done by using two CCD cameras mounted outside the target chamber, one filtered for the fundamental wavelength of laser light and the other filtered for the second harmonic, by use of interference filters.

4.4 Experimental measurements of specularly reflected light

This method of probing the absorption of the laser into the plasma proved to be successful, as discussed in Ebert *et al.* [95], and helped highlight that the structured targets provide a significant increase in the degree of laser absorption compared to the flat foil target and subsequently give an enhancement in the flux of energetic particles accelerated from the target. Another interesting observation from this experiment came from measuring the spatial distribution of the specularly reflected light captured on the scatter screen, as the different types of microstructured targets each produced distinctly different patterns of reflected light. Examples of these patterns are shown in figure 4.3, where the distribution of both the reflected 1ω and generated 2ω light can be seen for each target type. For the flat reference foil targets, a relatively smooth, circular disc of light is seen in both wavelengths of light; for the groove targets the light forms a repeating pattern typical of the diffraction patterns formed by light reflecting from a grating structure; for the pillar target, this repeating pattern is seen in two dimensions, due to the periodicity of the structures along the orthogonal axes. For both the groove and the pillar-type targets, the spatial frequency of the patterns in the reflected 2ω light is double that of the structures contained in the 1ω light. This is in agreement with Fraunhofer diffraction theory, where halving the wavelength of the light will result in the diffraction maxima to repeat with half the period [132]. In the case of the needle targets, however, instead of measuring a clear, periodic pattern in the reflected light, a

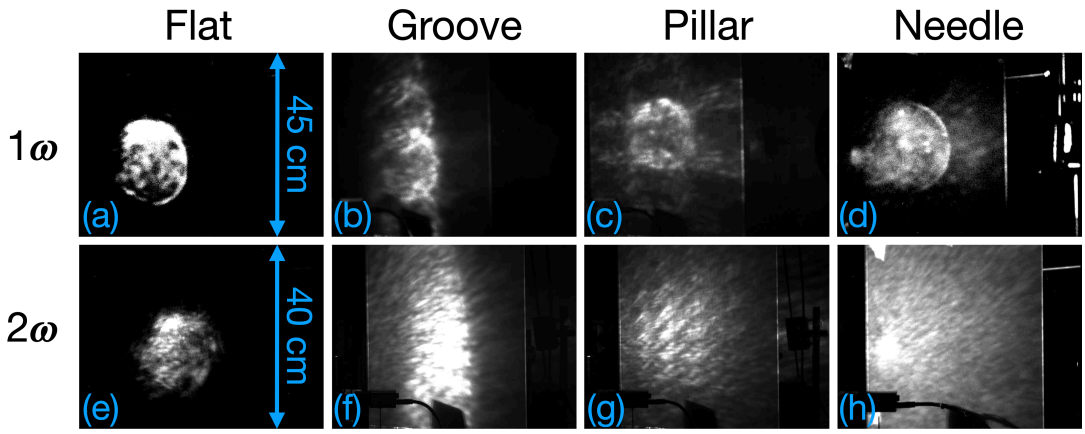

Figure 4.3: Measurements of the spatial-intensity distribution of the laser light specularly reflected from the plasma critical density surface, in fundamental and second harmonic frequencies, as captured on a scatter screen. The top row corresponds to the 1ω signal and bottom row corresponds to the 2ω signal for a flat foil target (a) and (e), groove target (b) and (f), pillar target (c) and (g), and needle target (d) and (h). The scale presented in (a) and (e) is the same for all 1ω and 2ω images displayed.

more diffuse speckle-like pattern is observed. This is most likely due to the fact that the light undergoes multiple reflections from the sides of the needle structures as it travels down to the base of the target, and thus leads to a much higher degree of scattering of the reflected light.

We can see the periodicity of the structures in the reflected light more clearly in figure 4.4, and how the spatial period halves from $\sim$ 13 cm in the 1ω case, shown in figure 4.4(a), to $\sim$ 6.5 cm when looking at the 2ω light, shown in figure 4.4(b). Here we can see lineouts taken through the centre of the structures on the scatter screen for both the 1ω and 2ω light and the dashed lines mark the position of the diffraction fringes that would be expected from diffraction theory, emphasising the expected doubling of the frequency when going from 1ω to 2ω. Since the 2ω light is primarily generated at the critical surface of the plasma, during the peak of the laser pulse when the intensity is at its highest [133], the fact that periodic structure can be seen in the 2ω light tells us that the critical surface of the plasma must retain some of the shape of the initial structure as the peak of the laser pulse interacts with the target. This conclusion is of significant interest, as it leads to the potential use of the structure in the reflected

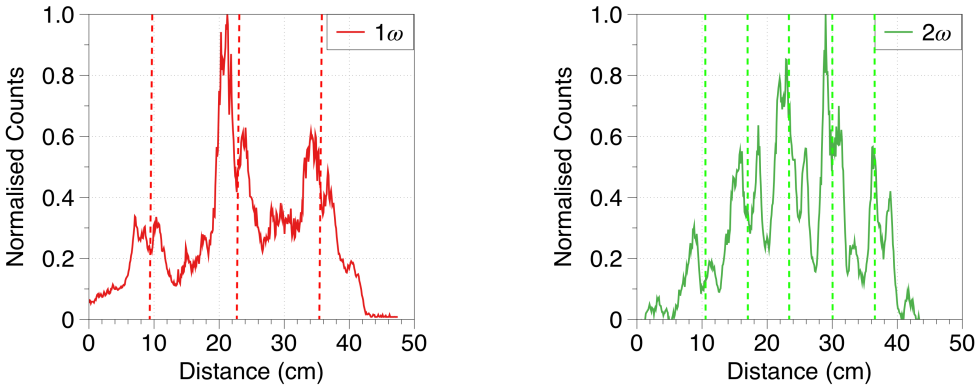

(a) (b)

Figure 4.4: Normalised lineouts taken through the centre of the measured (a) 1ω and (b) 2ω reflected light patterns produced by the groove target. The dashed lines correspond to the expected positions of light maxima from diffraction theory for a grating with a spacing of 5 μm.

light as a way of gaining valuable information about the evolution of the critical plasma surface within the region of the laser focus and over the time scale of the pulse of the laser, which is something that is very difficult to achieve by other means. We will now move on to investigate this in further detail, by looking at numerical modelling of an interaction between a laser and a groove-structured target in order to explore the evolution of the plasma critical surface, and will use a simplified optical ray-tracing model to investigate the potential of using the specularly reflected light as a tool to diagnose the temperature of the plasma.

4.5 Modelling of the evolution of structure depth and maxima separation in reflected light

To investigate this potential, firstly 2D PIC simulations were performed to investigate how the target critical density surface profile changes with time as it is irradiated by a high-intensity laser pulse. The 2D EPOCH [134] PIC code was used to model the interaction between a groove-structured target and a Gaussian laser pulse focused to a spot diameter of 7 μm (FWHM) and with a Gaussian temporal profile of 500 fs FWHM, which are the parameters that were used experimentally. The time $t = 0$ fs is defined

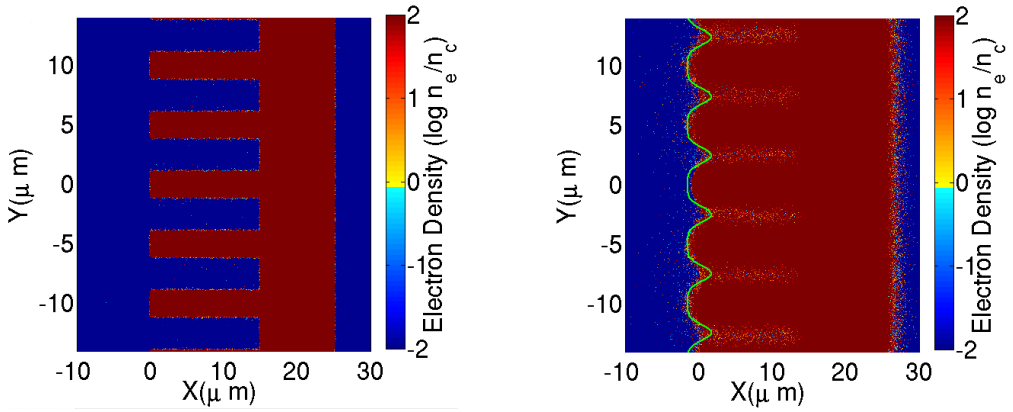

(a) (b)

Figure 4.5: PIC simulation results showing electron density spatial distribution (and thus the groove expansion) for a laser intensity of $5{\times}10^{19}$ Wcm^{-2}, pulse duration of 500 fs (FWHM) and 7 μm focal spot (FWHM), for (a) t=-500 fs, and (b) t=0. Overdense plasma is shown in red while underdense plasma and vacuum is shown in blue. The green line in (b) shows the critical density trace as used in the ray-tracing model.

as the time at which the peak of the pulse interacts with the target front surface, and the peak intensity of the laser pulse was 5×10^{19} Wcm^{-2}. The simulations were run with a 40 μm $\times$ 28.8 μm simulation box, with a mesh resolution of 2 nm $\times$ 2 nm, for a total simulation time equal to 1.2 ps. The plasma comprised of Si^{12+} ions, in order to replicate a partially ionised silicon target, with the electron and ion densities selected to ensure overall neutrality. The initial electron density was set to $200n_c$, which was chosen as it is sufficiently high to be a close approximation to a solid density target, but not so high that the computational requirements would become too extreme, and the groove target structure was initialised with the same periodicity and other dimensions as the targets used in the experiment.

In figure 4.5(a) we can see the distribution of electrons for a cold groove target, as it is initialised by the simulation, at t=-500 fs, and figure 4.5(b) shows the corresponding profile at t=0, the point at which the peak of the laser pulse hits the target. From this we can see that as the laser heats the plasma, the structures on the target become deformed and the spaces in between them become filled with plasma due to plasma thermal expansion, as discussed in section 2.8. Because of this, the shape of the critical surface of the plasma alters with time from an initially step-like profile, to a much

smoother sinusoidal-like profile. As this critical surface is the point in the plasma which the laser light is reflected from, this change in time of the profile of the reflective surface will result in a variation in time of the structure in specularly reflected light, and since the 2ω light is produced in the most intense part of the laser pulse, the distribution of the reflected light at this wavelength should provide a snapshot of the shape of the critical surface at that moment in time.

Having established that the heating of the plasma by the laser modifies the profile of the critical surface, we now look at how fast this change occurs as a function of plasma temperature. To do this, the evolution of the critical surface of the plasma was modelled without the presence of a laser, so that the temperature of the plasma could be carefully controlled without any additional laser heating. PIC simulations with no laser were conducted and the initial plasma temperature was systematically varied between 30 keV and 80 keV, and the critical surface was extracted after 500 fs in order to replicate what the peak of the pulse would experience. As well as the PIC simulations, a simple numerical model was created, where a total of 10^8 particles are distributed such that they match the geometry of the unexpanded groove target. For a chosen average plasma temperature, the average particle velocity is calculated through use of the plasma extension model as described in Mora *et al.* [75,135] and discussed previously in section 2.8, where the particles move at the ion acoustic velocity. From this average velocity, a normal distribution of momenta are assigned to the particles, and they are subsequently allowed to propagate ballistically with time. After a chosen duration, the resultant spatial distribution of particles can be observed, and the particles placed onto a coordinate grid system allowing for the distribution of particle number density to be found. By scaling the maximum particle density at time $t = 0$, to match the starting density of $200n_c$ from the PIC simulations, the critical density can be approximated to be the point when the particle density drops by 1/200 of the initial maximum. The resultant critical density surface can then be extracted, and its profile traced as a function of time for a given starting plasma temperature, so that once again the shape of the reflective surface that the peak of the laser would experience can be determined. In order to quantify the evolution of the shape of this surface, the effective depth of the

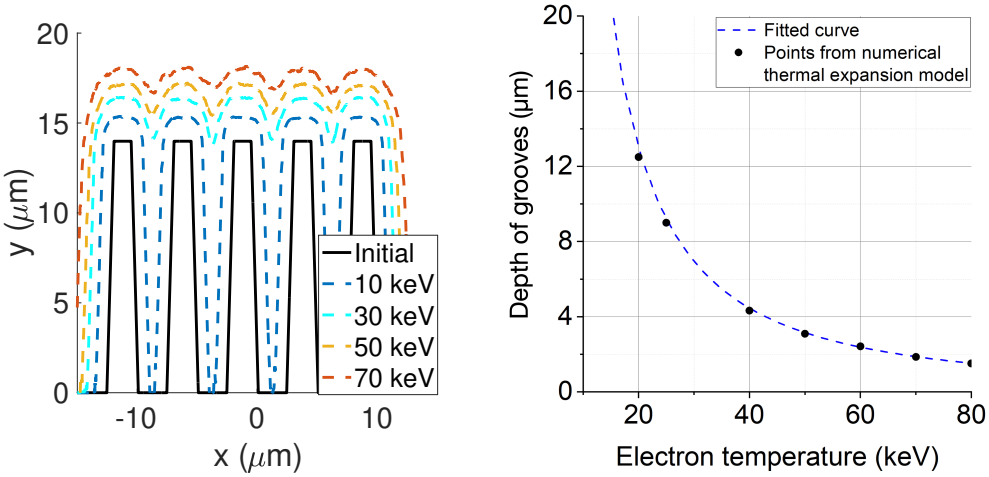

Figure 4.6: (a) Contour plot showing the spatial profile of the plasma critical density surface after 500 fs (t=0) with increasing plasma electron temperature, as determined from numerical modelling. (b) Groove depth as a function of electron temperature, as determined from the numerical thermal expansion model.

groove structure, that is the difference in height between the peak and the trough, was chosen as the key measurement, as it is fairly simple to quantify. Plots of the critical surface profile after 500 fs, for different plasma electron temperatures are shown in figure 4.6(a), where the evolution of the surface from the sharp step profile of the cold target, to the smooth sinusoidal-like surface of the hot, expanded target can be seen as the plasma temperature is increased. Measurements of the depth of the groove structures as a function of electron temperature are shown in figure 4.6(b).

This numerical model combined with the PIC simulations, provides insight as to how the shape of the critical surface of the plasma changes with time, and how this evolution is related to the plasma temperature. The final piece of modelling that is required is to link the observable changes in the patterns of reflected light, to the temperature of the plasma, through their mutual relationship to the depth of the groove structures. In order to do this, a simplified ray-tracing model was made by developing further on a model that is available from the MathWorks File Exchange [136] to enable investigation into how the spatial profile of reflected light at a detector screen evolves as the depth of the grooves in a reflective surface is changed. This ray-tracing model

traces rays of light as they reflect from a custom, user-defined, mirror surface, and the resulting spatial distribution of the reflected light is measured. A mirror surface closely matching that of the critical surface of the expanded groove structures in the PIC simulations at the peak of the interaction (t=0) was created. The profile is defined as $F(y) = A\sin((\pi/S)y + \phi)^C$, where A, S and C are parameters that vary the groove depth, spacing and shape, respectively, and ϕ is the phase of the structure. As these parameters are varied, the shape of the mirror surface can be made to transition from a sharp, step-like profile mimicking the profile of the cold, unexpanded target when C is large, to a much smoother sinusoidal profile, representative of the expanded target, when C is low ($\sim$1). As the profile of the reflective surface is varied, the direction of reflected light rays will change, modifying the spatial distribution of light as viewed on an imaging plane placed some distance away. When the light is collected on this imaging plane, the subsequent spatial distribution is seen to contain a series of intensity maxima, the spacing of which depend upon A, S and C.

Figure 4.7(a) shows a magnified view of the top of the grooves from the ray-tracing model, with arrows illustrating how the local curvature, and thus the degree of plasma expansion, changes the direction of light rays that are incident vertically from above. The example shown is for $A = 3.7$ μm, $S = 5$ μm, $C = 6$ and $\phi = \pi$, which results in the separation between the maxima to match that which was measured in the example from the experiment, shown in figure 4.3(c). This profile can then be overlaid onto the expanded plasma in figure 4.5(b), as shown by the green line, and it is found that for a given plasma electron temperature, this profile matches very closely the surface of the plasma in the PIC simulation. This provides the crucial link between the separation of the maxima in the reflected light and the degree of expansion of the plasma, and by extension the plasma temperature. From the ray tracing, a model which describes how the separation of the reflected maxima varies with the depth of the groove structures can be obtained, shown in figure 4.7(b).

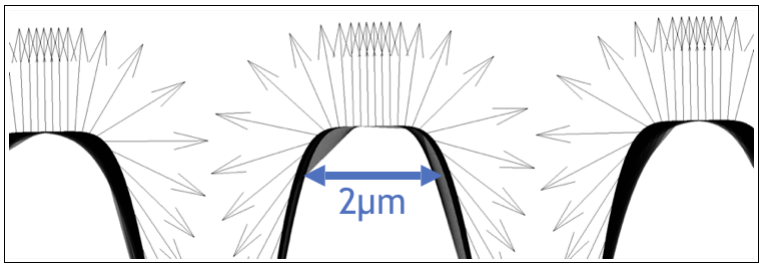

(a)

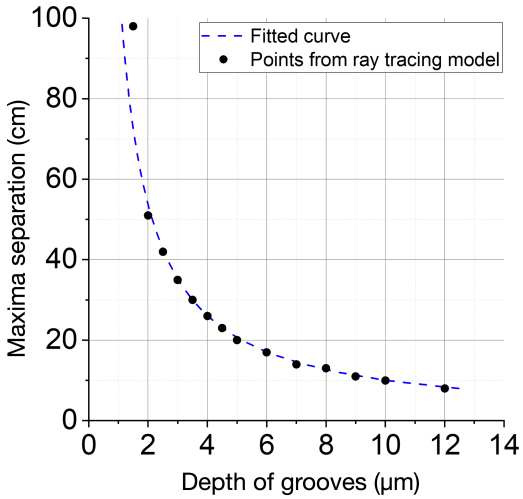

(b)

Figure 4.7: (a) Magnified view of the top of three groove structures with arrows showing the reflected light rays, for light incident vertically downwards. (b) Separation of light maxima at the distance of the scatter screen as a function of the groove depth, as determined from the ray-trace model.

4.6 Diagnosing plasma temperature and focal spot size

There are now two separate models: the PIC simulations with no laser and the numerical model, which helps to relate the plasma temperature to the evolution of the groove structures as shown in figure 4.6(b); and the ray-tracing model, which relates the evolution of the groove structures to the behaviour of the observable patterns in the reflected light, shown in figure 4.7(b). Combining these two models provides us with a composite model that can describe how the observed structure in the reflected light depends on the plasma temperature, a plot of which is shown in figure 4.8. Also shown on this plot are the data points from PIC simulations that were run with the

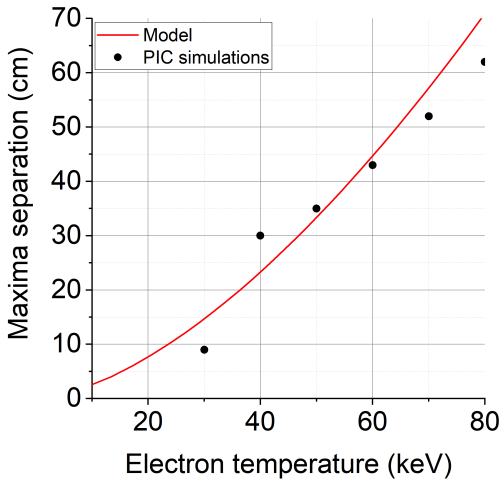

Figure 4.8: Plot of results from numerical modelling, showing expected separation between maxima in reflected light (at the distance of the scatter screen) as a function of plasma electron temperature. The red line represents the numerical model and black dots are data points from the PIC simulations.

laser present to heat the plasma, rather than manually setting the plasma temperature as before. As can be seen, there is a strong agreement in regards to the electron temperature needed to produce the required groove depth between this final model and the PIC simulations, which demonstrates the ability of this model to be used as a method of diagnosing the plasma temperature within the region of the laser focus, and at a time centred around the peak intensity of the pulse.

In the case of the experimental data presented here, and the measurements shown in figure 4.4(a), the spatial-intensity distribution of the light detected on the scatter screen displayed structuring with a spatial period of $\sim$ 13 cm, which when combined with the model presented in figure 4.8, suggests that the plasma electron temperature within the focal region is $\sim$ 28 keV.

As well as using the simple ray-tracing discussed previously, the influence of the shape of the structures on the target on the structure in the reflected light was also investigated by considering the wave behaviour of the light, and employing a diffraction model based on the Huygens-Fresnel principle [137,138]. Through the assumption that each point on the surface of the structured target emits light as a spherical wave, each with a Gaussian intensity profile, it is possible to numerically integrate the resulting

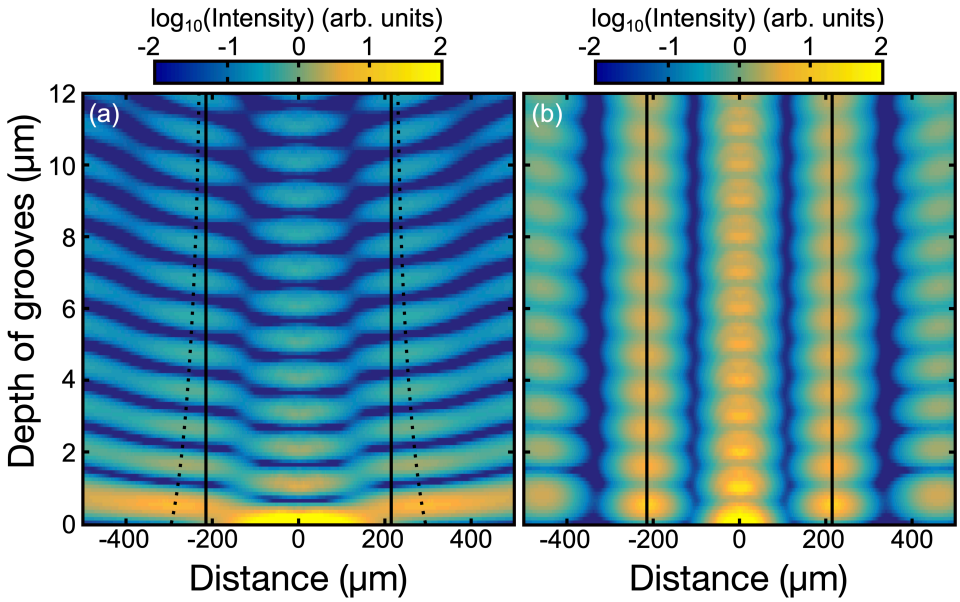

Figure 4.9: Intensity distribution map determined from a Huygens-Fresnel model at a plane 1 mm from an evolved groove structure as a function of A, with S=5 μm and laser focal spot FWHM equal to (a) 2 μm and (b) 7 μm. The solid lines indicate the expected first order diffraction position and the dashed lines correspond to the results determined from the model.

intensity distribution at a set distance from the target. In figure 4.9(a) we can see the behaviour of the intensity distribution for a focal spot size of 2 μm as the groove depth, A, is varied in the same manner as the ray-tracing model. As the depth of the groove structures is increased, we can see that the spacing between the maxima in structure of the reflected light decreases, and tends towards the separation expected from simple diffraction theory.

This behaviour is very similar to that seen by the ray-tracing model in figure 4.7(b), but the expected destructive interference that is produced as A varies over one wavelength can also be seen, which results in the diffraction pattern appearing to oscillate as A is increased. Experimentally, this behaviour, could, however lead to ambiguous results as A evolves over the course of the interaction with the laser pulse. When the focal spot diameter is increased to 7 μm, there is no change in behaviour with A, as shown in figure 4.9(b). This indicates that in order to observe the changes in the diffraction pattern seen in the ray-tracing model, the focal spot size must be reduced

to the order of the groove spacing or below.

Although this demonstrates a limitation in the use of this Huygens-Fresnel model to diagnose the expansion of the groove targets, and subsequently the plasma temperature, the relationship between the size of the focal spot of the laser, or rather the ratio of the focal spot diameter to the groove separation, and the observed spatial distribution in the reflected light suggests that this method could potentially be used to diagnose the size of the laser focus on a full power shot.

To investigate this possibility further, the effect that increasing the groove spacing, S, has on the spatial profile of the reflected light for a fixed focal spot FWHM of 7 μm is shown in figure 4.10(a). Here we can see that as S is increased, the periodic structure in the reflected light becomes less pronounced, until disappearing entirely for values significantly greater than the size of the focal spot. This shows that the presence of structure in the reflected light depends on the ratio of the laser focal spot size to the spacing between the grooves, and therefore it is entirely possible that targets could be engineered to have specific values of S, so that the size of the focal spot could be determined by analysing whether or not the reflected light contains a periodic structure.

In the Huygens-Fresnel model used, an assumption is made that the focus of the laser is centred on the middle of the groove spacing. In reality the position of the laser focus with respect to the structures on the target will vary shot-to-shot due to fluctuations in the stability of the laser pointing, and will therefore have some degree of random variation. The effect that this could have on this potential diagnostic method can be investigated by varying the transverse position of the laser focus relative to the groove structure, where the structured target surface is defined as a $\sin^2$ function and the position is varied by shifting the phase of this function through π. In figure 4.10(b) we can see how the distribution of the reflected light varies as this phase is shifted. For a focal spot size significantly smaller than S, when the centre of the focus moves away from the middle of the groove structure the reflection from the structure slope dominates, resulting in a displacement of the central maxima in the reflected pattern and additional maxima are observed, skewed in one direction. As the displacement is increased further and the laser focus moves onto the side of the next

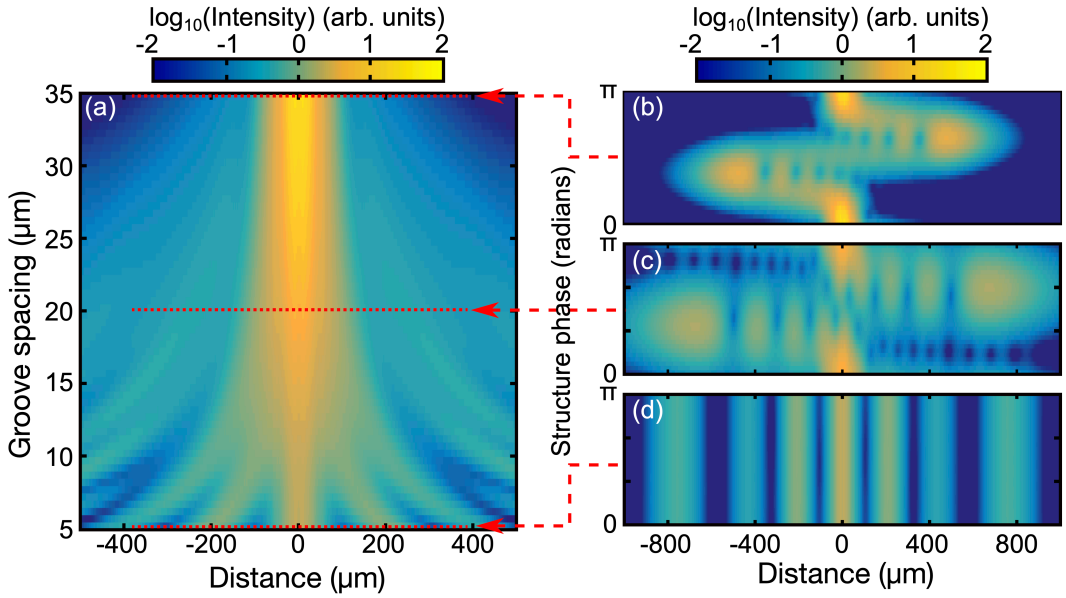

Figure 4.10: Intensity distribution map determined from a Huygens-Fresnel model at a plane 1 mm from an evolved groove structure as a function of S, with A=4 μm and laser focal spot FWHM equal to 7 μm. (b-d) The intensity profile as the phase of the structure is varied for (b) S=35 μm, (c) S=20 μm and (d) S=5 μm.

adjacent structure, the slope of the structure changes direction resulting in the central maxima displacement inverting. This suggests that despite there being a variation which depends upon where on the structure the focal spot is centred, this variation is predictable. When S is reduced to 20 μm, as shown in figure 4.10(c), the central maxima is displaced to a similar extent, but the diffraction effects begin to become more pronounced. Finally, as shown in figure 4.10(d), reducing S to 5 μm, a value smaller than the focal spot size, the relative position of the focal spot has no effect on the diffraction pattern, as expected.

4.7 Conclusions

The study reported in this chapter illustrates the possibility to use the spatial structure in the laser light specularly reflected from a micro-structured target to diagnose the plasma temperature localised spatially to the region of the focal spot at which the laser intensity is highest. Although the plasma surface evolves over the laser-target

interaction, the temporal window over which the expansion is probed is reduced by using second harmonic light, which is primarily produced at the peak of the intensity profile of the pulse. This allows for the expansion of the groove structures and therefore the critical surface of the plasma, and by extension the plasma temperature, to be probed specifically within the region of the laser focus and at peak laser intensity, which is otherwise exceedingly difficult to do on a shot-to-shot basis. Using the experimental measurements presented here, a plasma electron temperature of $\sim$ 28 keV is estimated to be achieved within the focal spot region. 2D PIC simulations carried out by A. J. Kemp and L. Divol [139], have shown surface plasma temperatures of $\sim$ 10 keV being reached within the plasma skin depth, for a similar laser intensity as being reported here. However, in that case, a short pulse duration of 40 fs was being modelled, so it is possible that the longer pulse durations being utilised here, and therefore the longer time over which the plasma is being heated, could account for the higher temperature being estimated.

This technique, through modelling, also demonstrates the possibility of estimating the on-shot focal spot size, by using targets of specifically engineered groove periodicity. These techniques are limited, however, to laser intensities below the threshold for which the laser radiation pressure exceeds the thermal plasma pressure. Above this, plasma expansion is replaced by laser hole-boring into the target, resulting in additional deformation of the critical density surface, preventing meaningful spatial information from being extracted from the reflected light [140]. This interplay between the plasma expansion and hole-boring is investigated further in chapter 6.

Chapter 5

Analysis of the spatial-intensity distribution of laser light transmitted through a plasma aperture

5.1 Introduction

Measuring the degree of transmission, due to self-induced relativistic transparency, of the laser passing through an expanding foil target is of great importance during experiments, and is a key measurement that helps with the understanding of which regime the laser-plasma interaction is operating under, as regimes such as target-normal sheath acceleration (TNSA) [141,142], light-sail acceleration [143,144], and relativistic induced transparency will exhibit differing degrees of laser transmission, due to the optimal target thickness being different for each mechanism. Measuring the energy of laser light that is transmitted can also aid in determining the degree of laser absorption [145], along with methods such as measuring the reflected light as discussed in chapter 4. Knowing which mechanisms are playing the dominant role in the acceleration of the charged particles, in turn allows for better optimisation of the interaction conditions and diag-

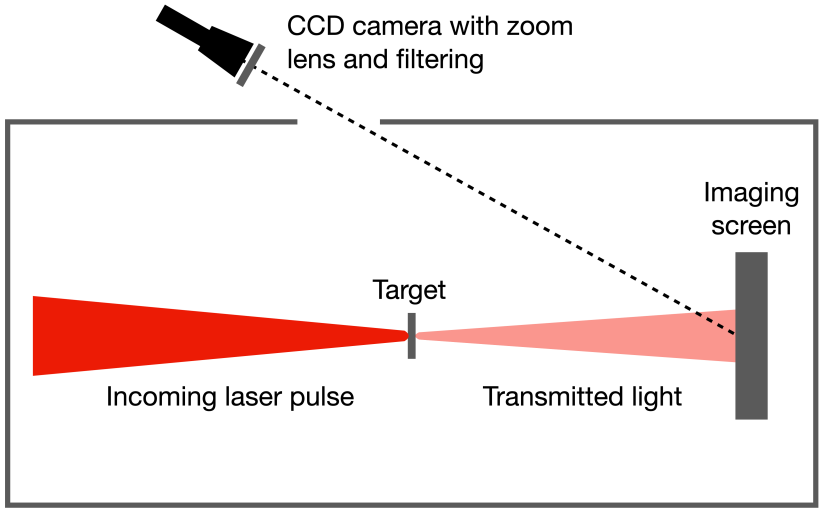

Figure 5.1: Schematic showing a typical experimental setup to image the transmitted light, with a scatter screen placed downstream from the target. A CCD camera positioned outside the chamber is used to image the screen through a chamber window, with any required filtering, such as bandpass filters or neutral-density (ND) filters.

nostic methods employed. As such, similarly to the specularly-reflected light imaging diagnostic discussed in the previous chapter, a commonly used diagnostic technique is to have an imaging screen placed downstream of the target to capture the transmitted laser light, which is subsequently imaged using CCD cameras mounted outside the chamber, as was discussed in section 3.4. A schematic of this setup is illustrated in figure 5.1.

This transmission diagnostic has been run on multiple experiments in the past, and has been used to build an understanding of how the laser forms an aperture in the plasma through which it can propagate, and how the degree of laser transmission through this aperture varies with parameters such as target thickness and laser energy [59, 84]. This diagnostic can also be used to observe changes in the divergence of the beam as it propagates through the target due to effects such as self-focussing, by looking for changes in the diameter of the transmitted beam on the imaging screen. This self-focussing of the laser can in turn act to boost the peak intensity of the laser, and enhance the energies of the accelerated particles [146], therefore characterisation of this phenomenon is crucial. However one aspect of the transmitted light that has

been observed but has not been fully explored or explained before, is the formation of stripe patterns in the spatial structure of the transmitted light. Across multiple experiments and on different laser systems, these stripe patterns have been observed to appear intermittently in the intensity distribution of the transmitted light, but the cause of their formation has not yet been determined. The formation of stripe patterns in the plasma electron density and electric field within the plasma aperture has been reported previously in Gonzales-Izquierdo *et al.* [84]. Continued investigation into why the stripe patterns in the transmitted laser light occurs is important, as their presence could provide new insight into the dynamics of how the laser forms an aperture and propagates through a plasma, and aid in the continuing development of ion acceleration techniques.

5.2 Experimental observations

In figure 5.2, a selection of images of the transmitted light is shown, as captured by the transmission imaging diagnostic on three separate experiments. The top set of images is from an experiment conducted at the PHELIX laser facility at GSI in 2019 (experiment A), the middle images are from an experiment at the Vulcan laser (TAP) in 2016 (experiment B), and the bottom images are from a second experiment at TAP in 2018 (experiment C). In each case, the laser parameters are nominally similar, with a laser wavelength of 1053 nm, a pulse duration FWHM of 500 - 1000 fs, and focal spot sizes of 5-15 μm, with a laser intensity of $> 1 \times 10^{20}$ Wcm^{-2} typically being produced. The target designs in each case are also similar, comprising of flat foil targets made from plastic, copper, or aluminium, and with thickness of up to 200 nm. For each data set, images captured from shots with varying target thicknesses are shown after background-subtracting a reference image with no laser light, and these images are grouped into either a “no stripes” or a “stripes” row, with the colour scaling being normalised across the images. From this, the stripe patterns that form in the transmitted light can be seen, as well as the fact that they appear for a range of different target thicknesses on each of the experiments. However, for many of the shots which do exhibit stripe

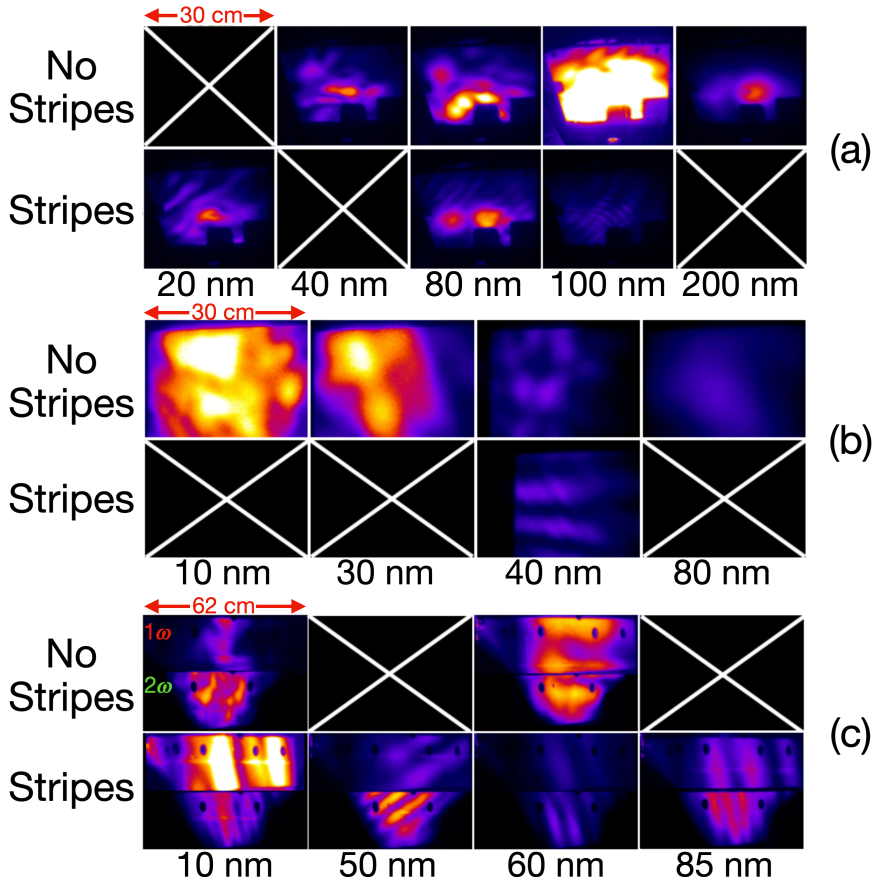

Figure 5.2: Matrix of images of the transmission screen on 3 different experiments: (a) - experiment A, (b) - experiment B, (c) - experiment C. In each case, the top row highlights shots that did not produce stripe patterns, and the bottom row highlights shots that did for nominally the same conditions. For experiment C, both 1ω and 2ω images are shown.

patterns, there are also comparable shots (in terms of target and laser conditions) that do not display any stripe patterning at all.

The first step in investigating the formation of these structures, is to determine if the appearance of these stripe patterns is related to any laser or target parameters, which may give an indication of the mechanism responsible for their creation. The first parameter that will be investigated is the degree of transmission of the laser through the target, by plotting the laser transmission, that is the proportion of the input laser light that is transmitted, as a function of target thickness, and highlighting the data-points on this plot that correspond to shots on which stripes are observed. The degree of laser

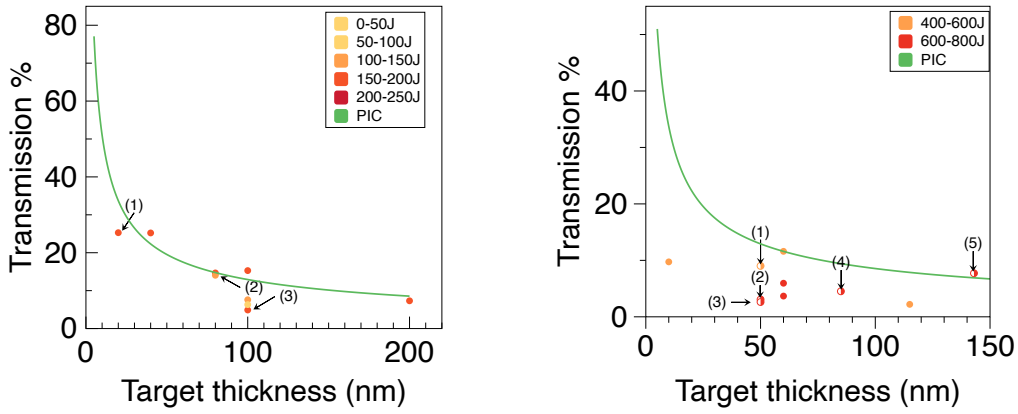

(a) (b)

Figure 5.3: (a) Plot showing the percentage of input light transmitted as a function of target thickness. Shown in yellow, orange and red, are the data-points from experiment A, and the green line is from PIC modelling. (b) The same plot as in (a), but for experiment C. In both plots, shots that displayed stripe patterns are numbered, and the colour of the points corresponds to different laser pulse energies.

transmission as a function of target thickness is a useful trend to employ for this, as it is a trend that has previously been characterised [59], and so any deviation from this trend could indicate a change in the behaviour of the interaction. These trends are shown in figure 5.3, with the data from experiment A in (a), and experiment C in (b). The post-compressor energy of each shot is represented by the colour of the datapoint as shown in the legend. A trend of transmission versus target thickness is also shown in green, which was produced by running a series of 2D PIC simulations for different target thicknesses and summing up the total laser energy transmitted through the target, and taking this as a percentage of the input energy. More details on the PIC modelling is given later in section 5.3. A selection of the shots on which stripes were observed are highlighted by arrows, and in both cases, it can be seen that almost all of the shots that demonstrate stripe patterns sit at low transmission values of less than 20%, and the vast majority of these sit at 10% or lower. Looking at how the data-points in each case sit relative to the trend from the PIC model, it can be seen that the data from experiment A generally fits well: however, for the experiment C data, many of the points sit at significantly lower transmission than expected. This experiment also had by far the

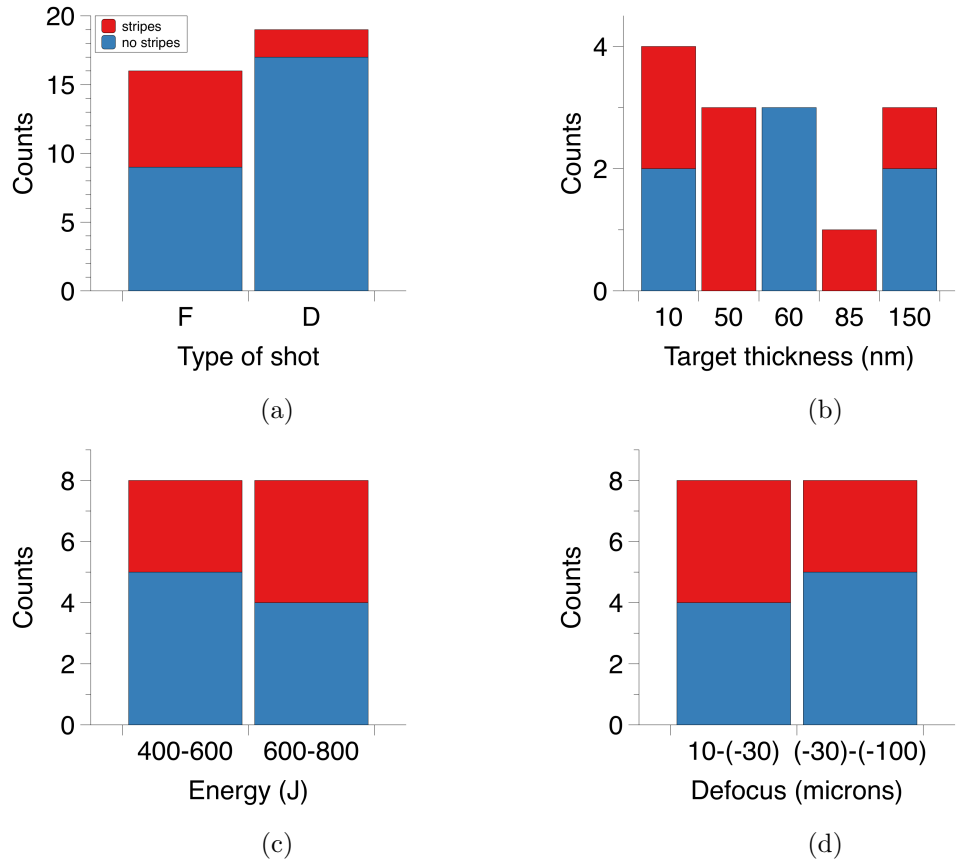

Figure 5.4: (a) Bar plot showing the distribution of shots with stripes and without stripes, for all shows separated into "full"shots (F) and "double pulse" shots (D). (b) Bar plot showing distribution of stripes and no stripes for "full" shots, separated by target thickness. (c) Bar plot showing distribution of stripes and no stripes for "full" shots, separated by laser energy. (d) Bar plot showing distribution of stripes and no stripes for "full" shots, separated by defocus distance.

highest occurrence of stripe patterns that were observed out of any of the experiments, suggesting that there is a correlation between low transmission values and an increased chance of observing stripe patterns. The reason that experiment C appears to have consistently lower than expected levels of laser transmission is unknown, but may be due to a reduced on-shot intensity compared to other campaigns as a result of a less optimised, astigmatic focal spot. Looking at these plots, however, it is clear that there is no direct correlation between the occurrence of stripes and the target thickness, as the data-points with stripes are not grouped in any particular region of the plot.

Since there is no obvious correlation between the appearance of stripes and the

target thickness, and so far the only correlation is there being a link between low levels of laser transmission and the formation of the stripes, an investigation into whether or not any correlations can be seen with other parameters is carried out. Firstly, the data are separated by which laser configuration was used on each shot, which in the case of experiment C, is either full laser shots, or temporally-separated double pulsed shots, and the number of shots that produced stripes is recorded, as well as the number that did not. Looking at figure 5.4, it is seen that there is a significantly higher probability of observing stripes for the full shots (43% of the time) than the double pulsed shots (10% of the time). The fact that stripes are not seen frequently with the double-pulse setup, could potentially be due to the plasma becoming significantly more expanded relative to single pulse irradiation [147], suppressing whichever mechanism is responsible for the stripes. Next, the double pulse shots are discounted and only the the full laser shots are considered, to see if the occurrence of stripes sits predominantly within a certain region of the other parameters. When these shots are grouped by target thickness, post-compressor laser energy, and laser defocus distance (that is the shift from the nominal position of the focal spot along the propagation direction), it is seen however, that the probability of observing stripes seems to be even across these parameters, with no clear trends emerging.

Since no correlations between these laser or target parameters, and the occurrence of stripes can be made, the next step is to look at the physical properties of the stripe patterns, and investigate if there are any correlations between those and the experimental parameters that can be seen. The two physical properties of the stripes that will be used, are the average spatial separation of the stripes in each image, and the rotational angle relative to a vertical orientation. In figure 5.5 the spatial separation of the fringes for the 1ω signal is displayed, as a function of laser transmission (a), energy (b), and defocus distance (c), and fringe angle for the 1ω signal against the same parameters is displayed in plots (d)-(e). In each case it is once again quite difficult to draw any conclusions from the plots as the data-points all tend to lie in either fairly flat, or scattered distributions. The one point of interest, however, is the plot of fringe angle as a function of defocus distance, shown in (f), where we see that the stripes have

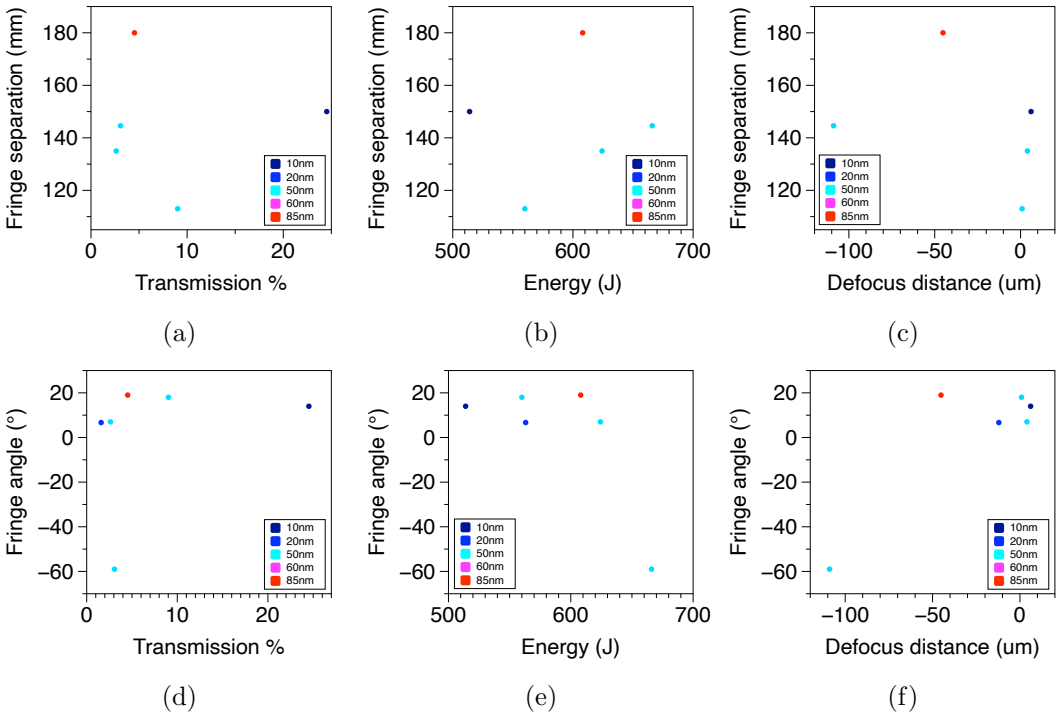

Figure 5.5: Plots of fringe separation (a-c) and fringe angle (d-e) as functions of laser transmission, post-compressor laser energy, and laser defocus distance. Target thicknesses in each case are denoted by the datapoint colours.

a fairly constant positive angle relative to the vertical for a range of defocus distances, but at the extreme of -100 μm defocus, the stripes suddenly rotate almost 90°. This behaviour could be an indication of astigmatism in the wavefront of the focusing pulse as it comes off of the parabola, which will be explored in more detail in section 5.3.

Figure 5.6 shows the separation and angle of the fringes for the 2ω light. In this case, similar overall behaviour as the 1ω light is observed, but there are differences in the positioning of some of the data-points. These differences may be due to the fact that the 2ω light is produced within a smaller region of the plasma and also results from a shorter period in time during the interaction between the laser and the target, (when the laser intensity is sufficiently high), whereas the 1ω light is present during the entire interaction [148, 149].

In figure 5.7 a lineout taken across the screen image, perpendicular to the rotational angle of the stripes, is displayed, with both the 1ω signal and the 2ω signals shown.

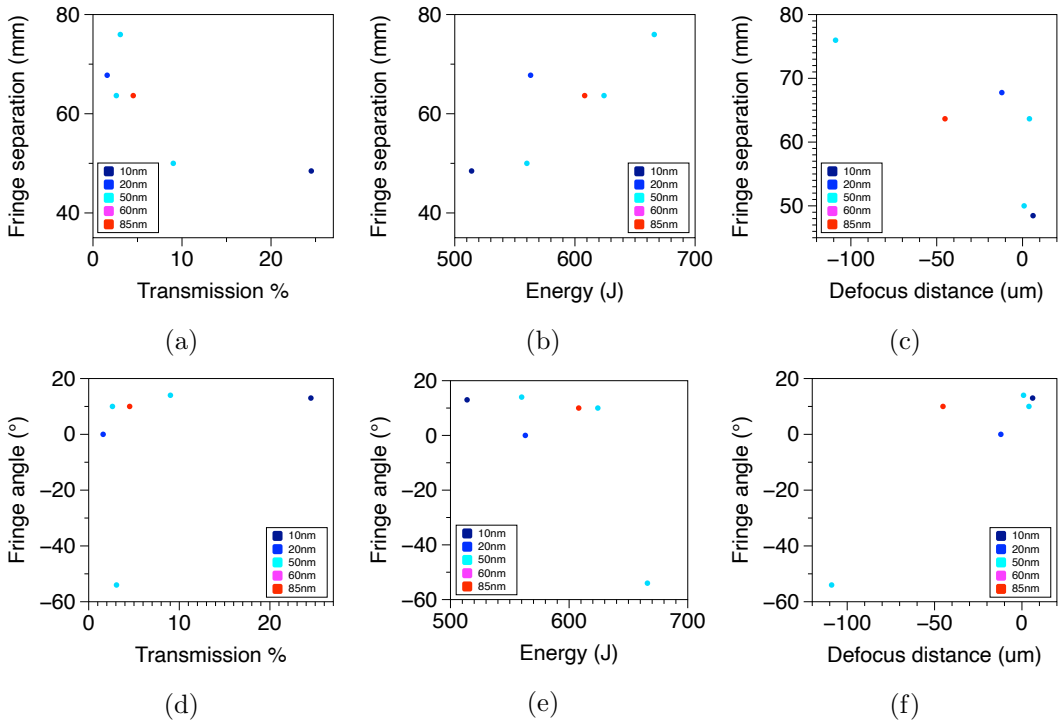

Figure 5.6: Plots of fringe separation (a-c) and fringe angle (d-e) for the 2ω light, as functions of laser transmission, post-compressor laser energy, and laser defocus distance. Target thicknesses in each case are denoted by the datapoint colours.

The fringes in this transmitted light are clearly visible, and it can also be seen that the distance between the fringes in the 2ω light is approximately half (70 mm) that of the 1ω light (145 mm). This is similar to the behaviour that would be expected of interference fringes according to aperture diffraction theory, where a halving of the wavelength of the light will half the separation distance of any fringes produced [150]. This suggests that what is observed experimentally could be some form of diffraction of the laser as it passes through the plasma, resulting in fringes to form in the intensity distribution further downstream.

Figure 5.8(a) shows the average separation distance between the stripes for both the 1ω and 2ω light as a function of the laser transmission. The 1ω data is rather scattered, and does not provide us with any clear trends, but the 2ω data exhibits much clearer behaviour, as the distance between the stripes decreases as the degree of laser energy transmitted increases. This would suggest that the diameter of the

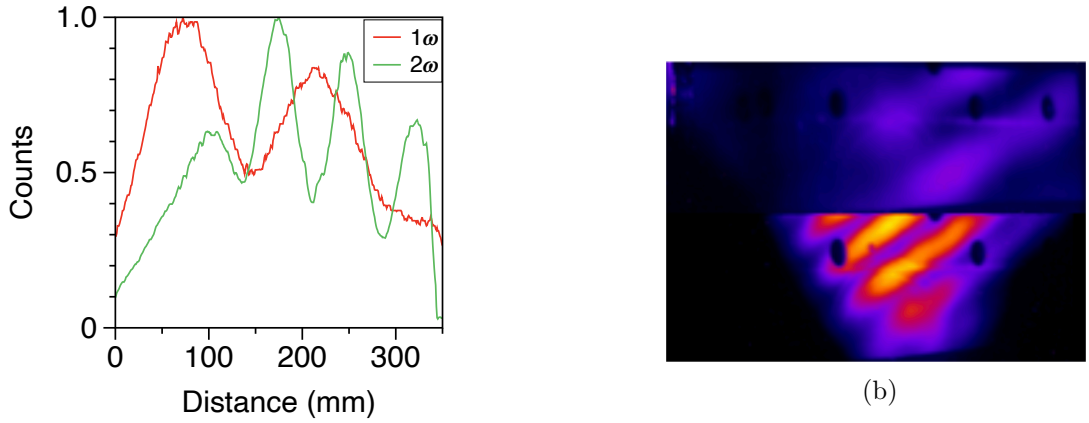

(a) (b)

Figure 5.7: (a) Lineouts taken across the screen image of the 1ω and 2ω light from the example shot from experiment C with stripe patterns shown in (b). Signals in (a) are normalised.

aperture in the plasma is increasing with the laser transmission, as a larger aperture diameter would result in diffraction maxima (i.e. the stripes) that are placed tighter together. From a plasma physics point of view, this also makes sense as with a higher degree of transmission, it would be expected that the aperture in the plasma would have to be larger to allow the greater amount of light through.

In figure 5.8(b) the ratio of the 1ω separation distance to the 2ω separation distance as a function of transmitted laser energy is displayed, along with data-points from PIC simulations. For low values of laser transmission, the ratio between these two distances is approximately 2:1 as expected by diffraction theory. However, as the laser transmission increases, this ratio diverges from 2:1, with the distance between the 1ω fringes increasing to $\times 4$ that of the 2ω fringes, as seen in figure 5.8(a). If the fringes in the transmitted light are being produced by diffraction through the plasma aperture, then this divergence in the ratio would suggest that the two wavelengths of light are experiencing different sizes of apertures. If this is the case, then it points to the occurrence of an optical phenomenon which is rather unique to the timescales of laser plasma physics, where the effective aperture size that light is diffracting through is evolving temporally and, due to the difference in the critical density between the 1ω and 2ω light, is also wavelength dependent. This is a phenomenon which can potentially

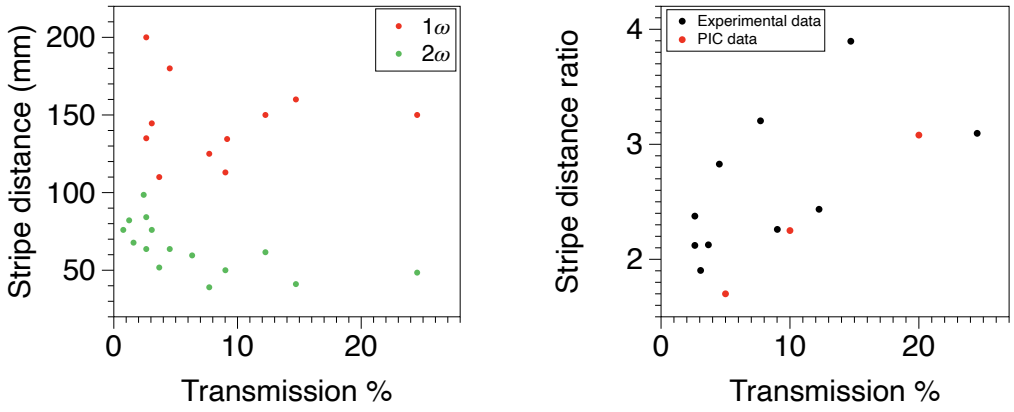

(a) (b)

Figure 5.8: (a) Plot showing the average distance between stripes as a function of the percentage of transmitted laser energy, for both the 1ω and 2ω light. (b) Plot showing the ratio of 1ω and 2ω stripe separation as a function of transmitted laser energy. Experimental data is in black, and PIC data is in red.

only be observed in this manner, and so further study could lead to being able to diagnose the temporal growth of the plasma aperture.

5.3 Modelling the spatial properties of an aperture and the subsequent influence on transmitted light

So far, the occurrence of the stripe patterns in the transmitted light has been linked to low levels of laser transmission, but exactly what causes the stripes to form in the first place has not yet been established, although diffraction through an aperture seems to be a promising candidate. To investigate the formation of the stripes further, an investigation of the underpinning physics via simulation is conducted. The initial route of investigation is to begin with the idea of the patterns being a result of diffraction as the laser passes through an aperture in the plasma, and to observe if stripes in the transmitted light also form in the PIC simulation of the laser-foil interaction. In order to do this, the ray tracing software Zemax, described in section 3.5.2, is firstly used to model an optical system with dimensions matching the experimental setup used in experiment C as accurately as possible, with a collimated beam of light reflecting from

a F/3.1 off-axis parabola and focussing through a pre defined aperture [122]. The shape and size of this aperture can be varied, and the resulting transmitted light downstream measured to determine how varying the spatial properties of the aperture affects the transmitted light, and if any patterns form.

Looking at the distribution of the transmitted light that we see experimentally in figure 5.2, however, it is clear that the laser cannot be diffracting through a simple circular aperture, as the formation of airy disc patterns is not observed, and instead stripe patterns are seen. A potential explanation for this is that the aperture in the plasma being formed by the laser is not circular, but elliptical. This is a reasonable assumption to make, as it is highly improbable that the aperture in the target would ever be a perfect circle. Any ellipticity present in the focal spot shape of the laser would act to drive the formation of an elliptical aperture [84]. Additionally, the linear polarisation of the laser would exaggerate heating of the plasma in that axis, widening the aperture in one direction more than the other [64]. Also, the presence of any astigmatism in the wavefront of the focusing beam can induce ellipticity in the focus, or if the target is mounted at an angle relative to the laser propagation direction, then the focal spot will be stretched into an ellipse. It is therefore highly likely that the focal spot will end up with some degree of ellipticity, and it is thus important to investigate how the distribution of the transmitted light behaves as both the overall size, and the ellipticity of the aperture is varied.

Figure 5.9 shows the effect that changing the size and shape of the aperture has on the distribution of the transmitted light downstream, as a matrix of images with increasing ellipticity going left to right, and increasing diameter, irrespective of ellipticity, going top to bottom. The dimensions of the region displayed in each image is cropped to match the area of the experimental imaging screen, so that the distribution of transmitted light is representative of what would be seen in experiment C. In the first column, the transmitted light is shown after passing through a circular aperture of increasing diameter and we see the formation of the outer rings of an airy disc as would be expected from diffraction theory [151]. As the aperture diameter increases from 4 μm, to 6 μm, and then to 8 μm, it is seen that the central spot decreases in

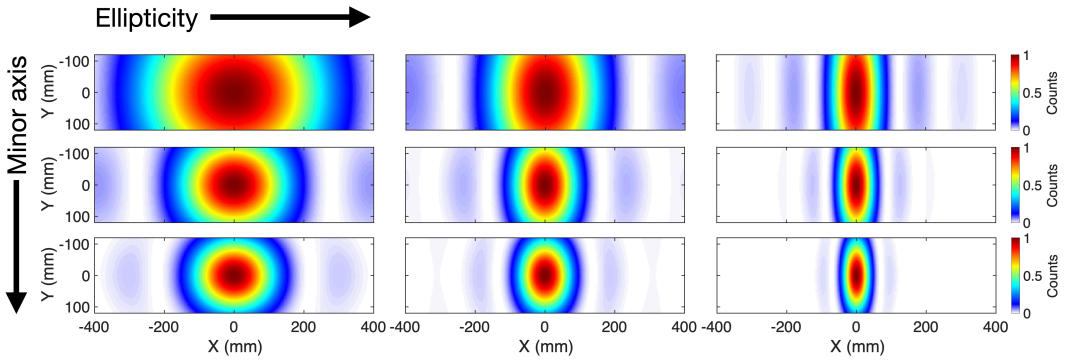

Figure 5.9: Matrix of images showing the profile of the transmitted light after passing through an aperture, modelled in Zemax. Images are shown for increasing values of ellipticity and width of ellipse minor axis. Minor axis widths are 4 μm, 6 μm and 8 μm. Degrees of ellipticity are ϵ=0 (circular aperture), ϵ=0.56 and ϵ=0.89.

size, and the outer ring increases in brightness. In the second and third columns, the ellipticity of the aperture, defined by $\epsilon = \sqrt{\frac{b^2-a^2}{b^2}}$, where a and b are the lengths of the major and minors axes, is increased, with the second column showing the result of apertures of ellipticity ϵ=0.56, and the third column for apertures of ellipticity ϵ=0.89. As the length of the major axis of the ellipse, and therefore the ellipticity increases, the diffraction pattern becomes more elongated along one axis, and the outer rings start to be transformed into more stripe-like shapes, with the upper right example in particular closely resembling some of the examples seen experimentally, shown in figure 5.2.

To verify that the behaviour observed in Zemax is plausible and the ray-tracing model is working correctly, the separation between the diffraction maxima is plotted as a function of aperture diameter (minor axis diameter in the case of elliptical apertures, with the major axis being fixed), and compared to the behaviour expected from Fraunhofer diffraction theory. As can be seen from figure 5.10, the scaling of the stripe separation from the ray-tracing model matches closely the trends expected from diffraction theory.

Another aspect of the stripe patterns that is worth investigating is the angle at which they form relative to the vertical axis of the detection plane, as this angle was observed to have slight shot-to-shot variations throughout the experiment, but for one shot in particular a very large shift of around 90° was measured. This was shown previously in

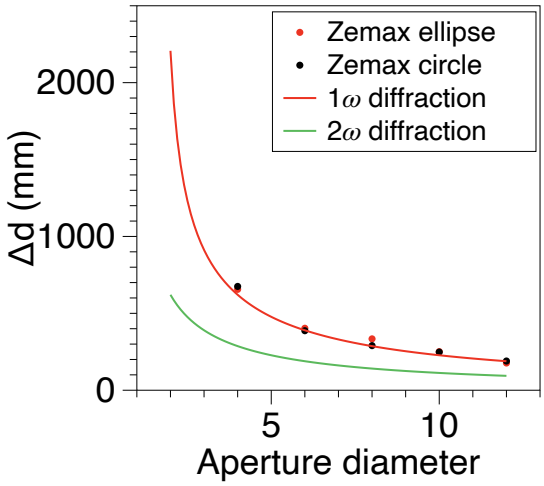

Figure 5.10: Plot showing fringe separation and aperture diameter. Zemax results with an elliptical aperture are shown in red, and circular aperture in black. Curves from the Fraunhofer diffraction, are also shown in red and green, for 1ω and 2ω respectively.

figure 5.5(e). The laser and target parameters for this shot were all nominal relative to the others, however this shot was also deliberately defocussed so that the focal point was shifted by 100 μm from nominal focus, along the laser propagation direction, in order to obtain a large focal spot. As mentioned previously, there may be a link between this rotation in the stripe patterns and the defocus of the laser due to unoptimised alignment of the OAP. When an astigmatism is present and the focal position shifts along the laser axis in one direction, an ellipticity will be induced in the spatial intensity distribution. As the focal position is then moved in the opposite direction relative to the position of best focus, an ellipticity will again be induced in the spot; however, it will have flipped by 90° [150, 152]. This is shown in figure 5.11, where we see this effect both experimentally, and through ray-trace modelling. This elliptical focal spot will in turn act to drive an elliptical aperture in the plasma [84], which should result in the angle of the stripes to also be rotated. To verify that this behaviour does indeed occur, an elliptical aperture in the ray tracing model was rotated by both positive and negative 45°, for aperture diameters of 4 μm, 6 μm and 8 μm. In figure 5.12(a) it is seen that when the aperture is rotated, the central lobe in the transmitted light rotates to match the aperture orientation, and the outer lobes tilt to the same degree. This

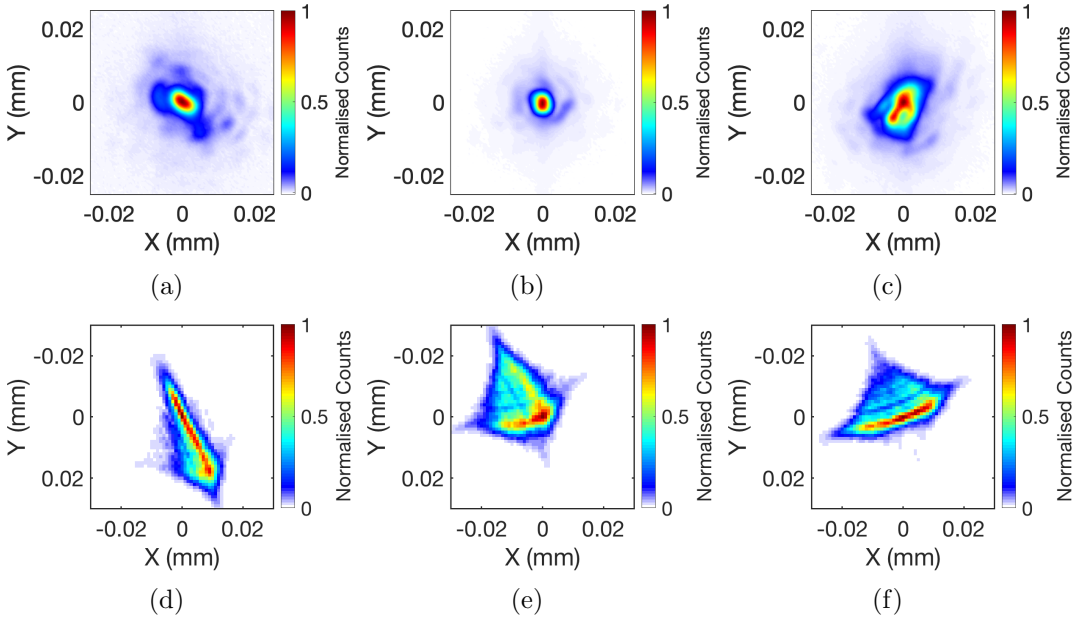

Figure 5.11: Top - Images of focal spots taken during a previous experiment on TAP, showing the angle of ellipticity rotating as the defocus distance changes. Bottom - Images from Zemax, showing how the intense region of the focal spot flips by 90° as the imaging plane is scanned along the laser propagation axis. Defocus values are: (a) +87.5 μm, (b) +0 μm, (c) -83.5 μm, (d) +40 μm, (e) +0 μm, (f) -40 μm.

gives an explanation for the small variations in the angle of the stripes, where small variations in the distribution of the focal spot causes an elliptical aperture to form at slightly different angles, and it also gives us a possible explanation for the dramatic change in angle when the laser spot is defocussed.

Up until now the modelling conducted has involved predefined apertures for the laser to propagate though, but in reality it is the laser itself that creates this aperture. To verify that the formation of stripes are seen when modelling a more realistic scenario, high resolution 3D PIC simulations were run with an overdense plasma target. However, due to limits on the computational resources available, the laser pulses being modelled had to be restricted to ∼60 fs. The simulations were run with $1440 \times 1620 \times 225$ cells, forming a $100 \times 100 \times 8$ μm box, containing an overdense plasma target. Into this box a p-polarised laser with a pulse duration of 60 fs, and intensity of 6×10^{20} Wcm^{-2} was propagated. After propagating through the plasma, the position of the laser was tracked by using a moving window, such that its spatial profile could be sampled as

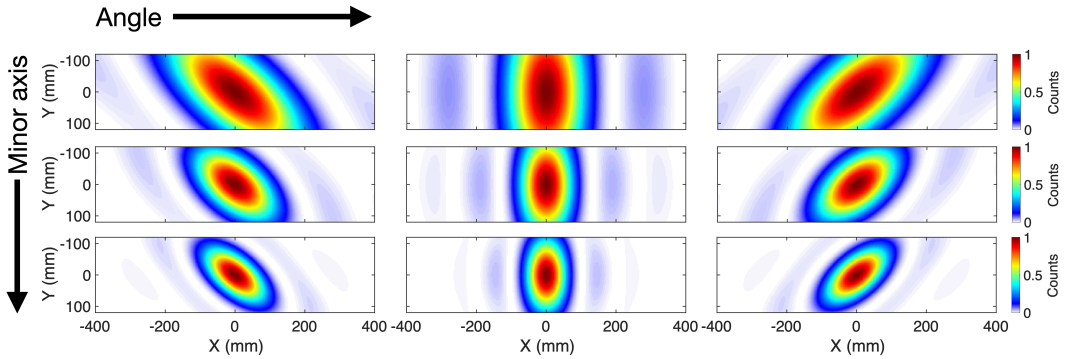

Figure 5.12: Matrix of images showing the profile of the transmitted light after passing through an aperture with ellipticity, as modelled by ray-tracing. Images are shown for ellipse angles of -45°, 0°, and +45°, and increasing width of minor axis.

a time-integrated image, a significant distance downstream to ensure that the near-field electric field was being imaged. This time the target did not have any preformed aperture, but rather the focal spot of the laser was given an ellipticity to resemble the elliptical spots seen from previous experiments, which in turn creates an elliptical aperture in the plasma. In figure 5.13, 2D slices taken through the 3D simulation box are shown, with the electric field of the focal spot of the laser, the electron density of the target plasma, and the time-integrated electric field 90 μm after the target, shown in figures (a), (b), and (c) respectively. The formation of an elliptical aperture can be clearly seen in figure 5.13(b), and in figure 5.13(c), it can be seen that the time-integrated distribution of the transmitted light after passing through the target does indeed exhibit stripe patterns, verifying that the structures are not simply a product of manually preforming the aperture, but do occur in more realistic simulations of the laser pulse interaction with a simple planar foil target.

This aperture diffraction model, so far, has explained the observations well: it can explain how the presence of ellipticity in the focal spot of the focal spot results in the formation of an elliptical aperture in the plasma, and subsequently stripe patterns in the beam further downstream. The ellipticity of the laser can be explained by the presence of astigmatism in the focussing of the laser wavefront, as well as simply having a poorly optimised focal spot. It can also show that the spacing of these stripes scales as expected from diffraction theory, and that a rotation in the laser focal spot spatial

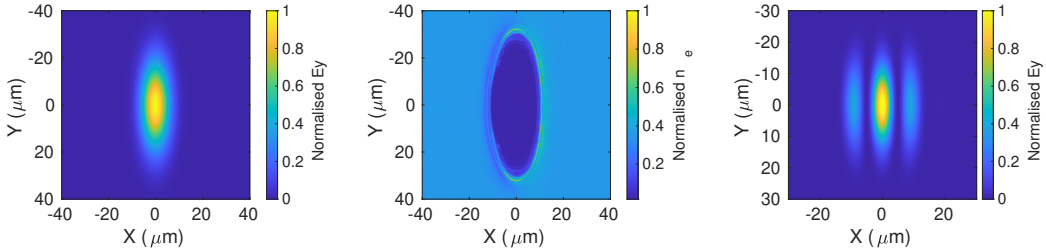

Figure 5.13: PIC modelling showing the electric field distribution of the propagation of a laser pulse with an elliptical focal spot, passing through an overdense target. (a) plot of electric field at the laser focus. (b) plot of electron density after laser propagation, taken as a slice through the target. (c) plot of time-integrated electric field 90 μm after the target, displaying stripe pattern. Each plot is normalised to the maximum value.

distribution, and subsequently the aperture, can induce a rotation in these stripes.

In figure 5.14(a), the lineout of the experimental data from before is shown once again, and in figure 5.14(b), a lineout of the profile of the light from the high resolution PIC simulation is displayed. It is when comparing these two plots that the biggest issue with the aperture diffraction hypothesis as being the explanation of the formation of the stripe patterns can be seen. The distribution of the intensity across the screen of the experimental data does not match the Gaussian intensity profile demonstrated by PIC modelling, and that is expected from the diffraction theory, but rather we see a much flatter intensity profile of the fringes. This means that either the idea of aperture diffraction is correct but with some additional plasma physics that has not been accounted for, such as longer timescale effects that do not have time to occur in the short-pulse simulations, or a different process entirely is responsible.

The simulations that have been conducted to understand the formation of the stripe patterns have all been run for short ∼40 fs pulses due to computational constraints. However, experimentally longer pulse lengths of up to ∼1 ps are used. It is possible that the mechanism responsible for the formation of the stripe patterns with the flatter intensity distribution that we see experimentally is only dominant when considering these longer pulses. The short-pulse PIC simulations may therefore never show the desired effect due to there simply not being enough time for the mechanism responsible to be established. Although this explanation is plausible, it is not definitive and so we

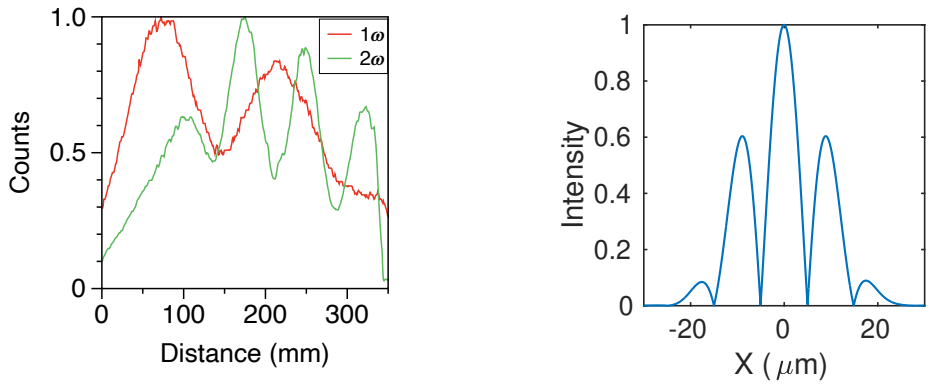

(a) (b)

Figure 5.14: (a) Plot showing lineouts of the 1ω and 2ω light from an example TAP 2018 shot with stripe patterns, normalised to their maximum. (b) Plot showing a lineout of the intensity profile of the stripe patterns in the PIC simulation shown in figure 5.13(c), normalised to the maximum.

will now explore some alternative hypotheses.

5.4 Alternative hypotheses

As was seen in figure 5.14, the flatness of the intensity profile of the transmission stripes could suggest interference between two sources as being a source of the stripes rather than aperture diffraction. This process would produce fringes with much more consistent intensity, rather than the more, on average, Gaussian intensity profile that the modelling so far has predicted [153]. When looking at images of the transmitted light taken from experiment A, shown in figure 5.15, two clear bright spots of transmitted light on the screen can be seen, with a comparatively lower brightness stripe pattern in the background. This could be an indication of two sources of light propagating from the target and interacting with each other, causing a pattern of fringes similar to two-slit interference. A few likely scenarios that could potentially cause this effect are discussed below.

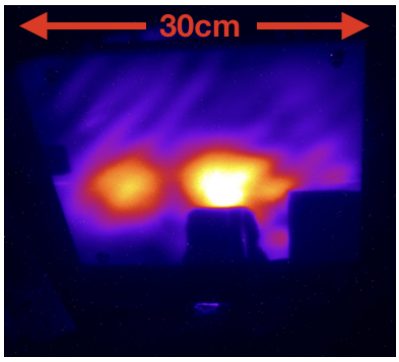

Figure 5.15: Image of transmitted light as captured by the scatter screen, from experiment A showing two prominent hot spots with a striped pattern in the background.

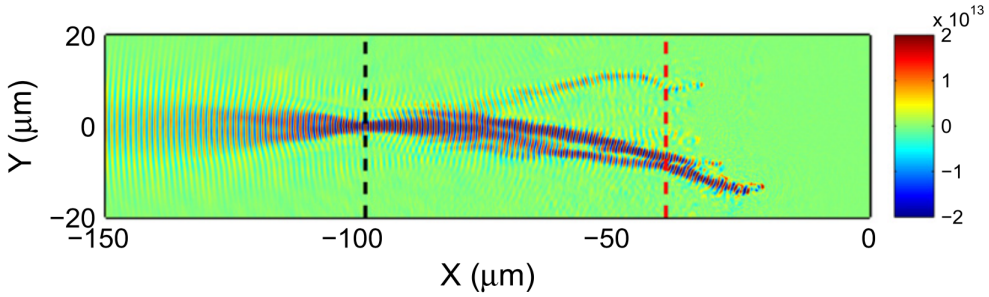

Figure 5.16: 2D PIC simulation showing bifurcation of the laser as it propagates through a long scale-length plasma. Electric field in units of Vm^{-1} is shown. Reproduced from Gray *et al.* [83]

5.4.1 Laser bifurcation

The first possible explanation is that the laser is bifurcating as it passes through the target, causing the beam to split into two or more components [83]. As the beam bifurcates, the two filaments would diverge away from each other as they propagate through the target due to fluctuations in the refractive index of the plasma, as shown in figure 5.16. This divergence could lead to the two components of the beam fully separating in space, creating two distinct spots on the imaging screen. As these two beams propagate downstream, they could act as two interfering sources and create a pattern of maxima and minima, much like the stripes seen experimentally.

One issue with this suggestion however, is that in order to observe breakup of the laser pulse in this manner, typically very long scale-length plasmas are required, on the

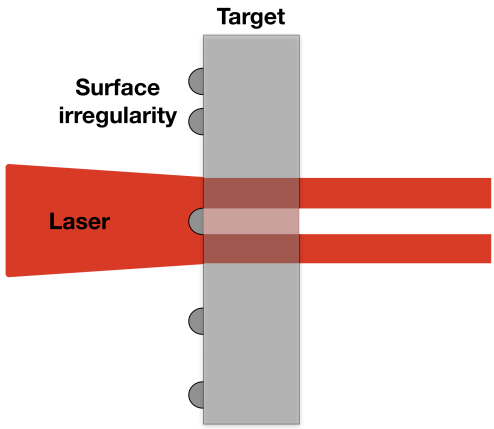

Figure 5.17: Schematic of a possible scenario whereby some form of irregularity on the front surface of the target, such as wrinkles in the foil, or dust and other particulates, causes the laser to be separated into two beams as it propagates through the target.

order of tens or even hundreds of microns. In the case presented here, much thinner targets are being considered, and therefore it is likely that much shorter distances of plasma are present for the laser to propagate into, although the plasma will expand significantly during irradiation. Additionally, laser bifurcation is an intrinsically random behaviour, seeded by the growth of transverse instabilities within the plasma [154], and as such it is unlikely that it would occur with the same degree of regularity as the appearance of the stripe patterns that have been observed. Bifurcation also would likely not be able to account for the rotation in the angle of the stripes as the laser is defocussed for best focus.

5.4.2 Target surface irregularity

A second possible cause of interference in the transmitted light could be that the laser beam gets broken up into two parts due to irregularities in the thickness of the target, causing a path difference between different parts of the laser. These irregularities could be due to folds or crinkles in the surface of the target, or possibly particles of dust partially occluding a part of the focal spot. This could result in part of the laser having to propagate through a marginally greater thickness of material than the other part,

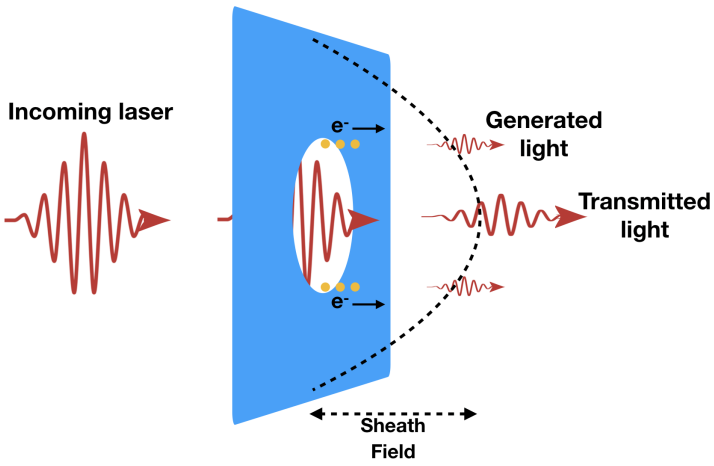

Figure 5.18: Illustration of the generation of electron bunches at the edges of the aperture being accelerated by the laser pulse, which subsequently undergo deceleration due to the sheath field, producing a source of coherent light.

leading to a separation of the two parts of the beam, as shown in figure 5.17, and subsequently interference between these two "sources". The issue with this mechanism is that, again, it would be unlikely to occur with the same frequency that the stripes have been observed, and it would not account for the rotation in the patterns.

5.4.3 Coherent transition radiation (CTR)

A third possible cause of the stripe patterns could be the mixing of the transmitted light and CTR as reported in Duff *et al.* [155]. Here, a linearly polarised laser acts to directly accelerate bunches of electrons from the edges of the plasma aperture, as illustrated in figure 5.18. These electron bunches are accelerated into the region of the sheath field at the rear of the target, where they subsequently experience strong electrostatic forces acting to decelerate them, resulting in the radiation of light and the production of coherent light source. This CTR light then mixes with the transmitted laser light, modifying its spatial mode, and potentially this could occur in such a way as to produce interference between these sources of light.

This is likely a more probable process than the others that have been suggested, as it has been shown to occur with ultra-thin foil targets like those used in the experiments

discussed in this thesis. However, the light produced by this mechanism is typically of a much lower intensity relative to the main transmitted beam than is observed here. In the case of our transmitted light patterns, the magnitude of the fringes, i.e number of counts, peak to trough, makes up a significant part of the overall intensity of the signal, typically around 15 - 20%. This would suggest that the sources of light responsible for the interference pattern must therefore have an intensity of a similar order of magnitude as the main component of the transmitted light; however, the intensity of the light produced by CTR is typically between 1 and 3% of the transmitted light.

5.5 Conclusion

During this investigation into the formation of the stripe patterns in the transmitted laser light of targets undergoing relativistic self-induced transparency, analysis of the properties of these stripes has been carried out, and how their presence, and physical attributes such as stripe spacing and rotational angle, could be related to a variety of target and laser parameters. Modelling has been undertaken, using both ray-tracing and PIC simulations, to try and ascertain the physical processes responsible for their formation. Although no definitive answer has been found with the techniques and measurements available, a variety of feasible scenarios have been discussed which could potentially explain the observations. In order to model the formation of the stripe patterns, high resolution 3D simulations at long pulse lengths would be required, the computational requirements of which are currently out with our budget and time constraints. Currently, as discussed in section 3.5.1, only short timescale laser pulses can be simulated in 3D and at this resolution, which may well be fundamentally incompatible with the processes we seek to observe, as they may required longer timescales to be established. Future advances in the computing capabilities available will certainly push the boundary of what is able to be modelled, enabling for much more in depth and realistic laser-plasma interactions to be modelled.

In addition, the proposed alternative hypotheses could be tested experimentally. The possibility that the laser is bifurcating due to irregularities on the surface of the

target, could be tested by utilising targets that have small microstructures on the front surface, such as micron-scale beads. Images of the transmitted light from these targets could be compared to those from the regular flat targets, to determine if there is a higher incidence of observing the stripe patterns. The potential for CTR to be contributing to the formation of the stripes could be tested by measuring the probability of observing stripes as the angle of incidence of the laser on the surface of the target is increased, as it would be expected that the CTR light would propagate in the direction normal to the rear surface of the target.

It is hoped that the work that has been carried out here, would be able to be carried on in the future and investigated further as discussed, allowing for the source of the stripes to be determined, as understanding the behaviour of the plasma aperture could lead to the possibility of being able to control the dynamics of the aperture and influence the acceleration of the charged particles.

Chapter 6

Spectral analysis of back-reflected light and the dependence of target heating and expansion on laser polarisation

6.1 Introduction

In this chapter, experimental measurements of the back-reflected laser light from the irradiation of thin foil targets with short, 40 fs, high intensity laser pulses will be presented and discussed. Analysis of the spectral broadening of this component of light from the interaction will be carried out, along with numerical modelling, to determine the cause of variations in the magnitude and spectral direction of the broadening, when comparing the irradiation of a target with p-polarised light and c-polarised light. In addition, results from modelling of the influence of self-phase modulation on the spectra of the back-reflected laser light will be presented, in order to help explain some of the spectral features that are observed as the light is passed out of the target chamber, through a glass window.

During the interaction of a high intensity laser pulse and target, the back-reflected

light is the component of the laser light that is reflected from the front surface of the target back along the axis of laser propagation. When the target is angled such that the laser is at normal incidence, this back-reflected light will be comprised of both the specularly reflected light, such as that which was investigated in chapter 4, and scattered light. Spectral measurements of this back-reflected laser light can be of great interest for studying mechanisms of the interaction, such as laser hole-boring [156], plasma expansion, and the amplification of laser light by pulse compression [157], as well as being a tool for measuring laser absorption into the generated plasma. As such, measuring the spectrum of the light reflected from the plasma critical surface, and diagnosing any changes in the spectral properties of this light with respect to another interaction, can give insight into the behaviour and motion of the plasma at the critical surface. Similar measurements of the motion of the plasma critical surface have been made in the past, through utilising an optical pump-probe to observe the Doppler shift of light incident on the front surface of the expanding target [158]. The work presented here, however, investigates the motion of the plasma critical surface for significantly higher laser intensities, and for ultra-thin targets undergoing relativistic self-induced transparency. In this regime, the motion of the critical surface becomes significantly more complex, the study and understanding of which is of great importance when considering the extreme laser intensities achievable by the newest laser facilities.

6.2 Experimental setup

The spectra of the back-reflected light that are under investigation in this chapter were measured by taking a sample area of the laser via a pick-off mirror as it is reflected back up the laser axis after irradiating the target. This pick-off of the beam is achieved by placing a 1 inch mirror to divert a portion of the outer edge of the reflected beam out through a glass window with a thickness of 2.5 cm in the side of the target chamber. This pick-off beam is then passed through a series of turning mirrors before it illuminates a PTFE screen, producing a diffuse area of scattered light that can easily be sampled, as discussed in section 3.4. This diffuse light is collected by an optical fibre placed

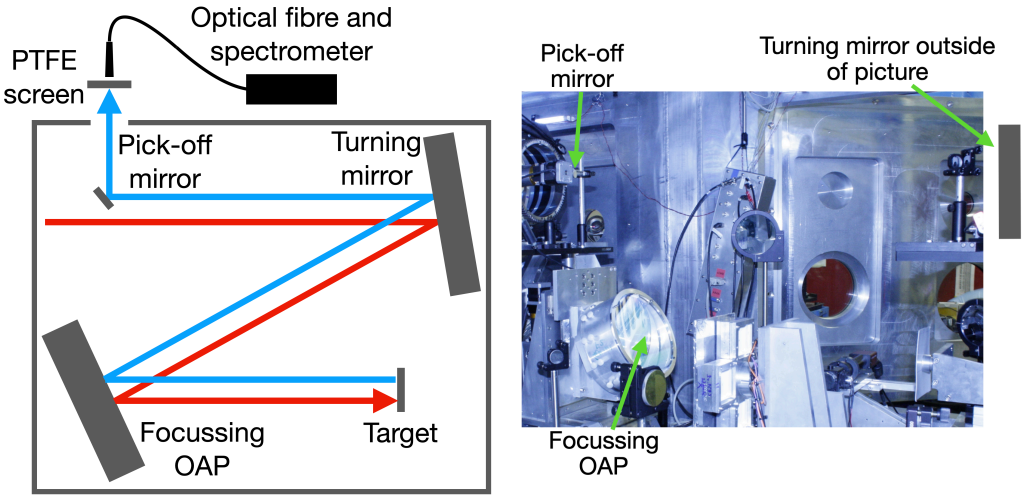

(a) (b)

Figure 6.1: Schematic (a) and photograph (b) of the experimental setup used in the Gemini laser target area. The incoming laser, shown in red, enters top left, reflecting from a turning mirror and an off-axis parabola, before focussing onto the front surface of the target. The light reflected from the target, shown in blue, passes back along the path of the incoming laser and a small 1 inch pick-off is directed out of the vacuum chamber before being directed onto a PTFE screen. The light from this screen is then collected using a optical fibre and directed to a spectrometer.

behind this screen and the spectrum then measured by an Ocean Optics spectrometer with a 100 ms integration time, 0.5 nm spectral resolution and measurement range of 188 - 1100 nm. A schematic of this setup is shown in figure 6.1 along with an example spectrum.

6.3 Experimental measurements of spectra of back-reflected laser light

Using the Gemini laser, a number of aluminium foil targets with thickness ranging from 10 nm to 100 nm were irradiated by either a linearly or circularly polarised (controlled by a $\lambda/4$ waveplate) 40 fs FWHM laser pulse, with a central wavelength of 800 nm and bandwidth of 40 nm, and with a calculated on-target intensity of $(3 \pm 0.5) \times 10^{20}$ Wcm^{-2}. The spectrum of the back-reflected laser light was measured for each shot, along with a reference spectrum of the incoming laser light before it interacts with the

target taken from further up the laser chain, before the target chamber. Example back reflected spectra measured for interactions employing 40 nm and 50 nm foil targets are shown in figure 6.2, where the spectrum of the back-reflected light are shown in blue, and the input reference spectrum for the same shot is shown in red.

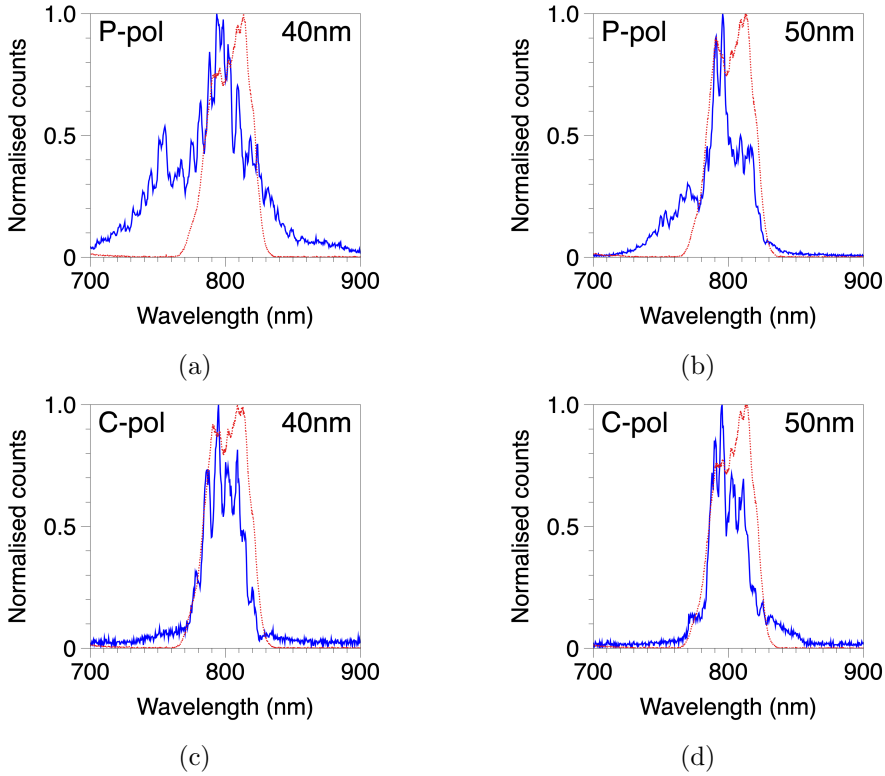

Figure 6.2: Spectra measured of back-reflected light from the irradiation of 40 and 50 nm-thick foil targets using both p-polarised and c-polarised laser pulses. Measured spectra shown in blue, with input reference laser spectra shown in red.

In the cases of the p-polarised laser light shown in figure 6.2(a) and (b), it is seen that the measured spectra after the interaction with the target display significant broadening compared to the input reference spectra measured before the interaction. In the cases of the c-polarised laser light shown in figure 6.2(c) and (d) however, this broadening does not occur. When plotting the spectral peak of the back-reflected spectra as a function of peak laser intensity, shown in figure 6.3(a), it is difficult to define any clear trends in the shift of the peak wavelength as the laser intensity increases. What is clear however, is that there is a greater degree of variation in the peak wavelength of

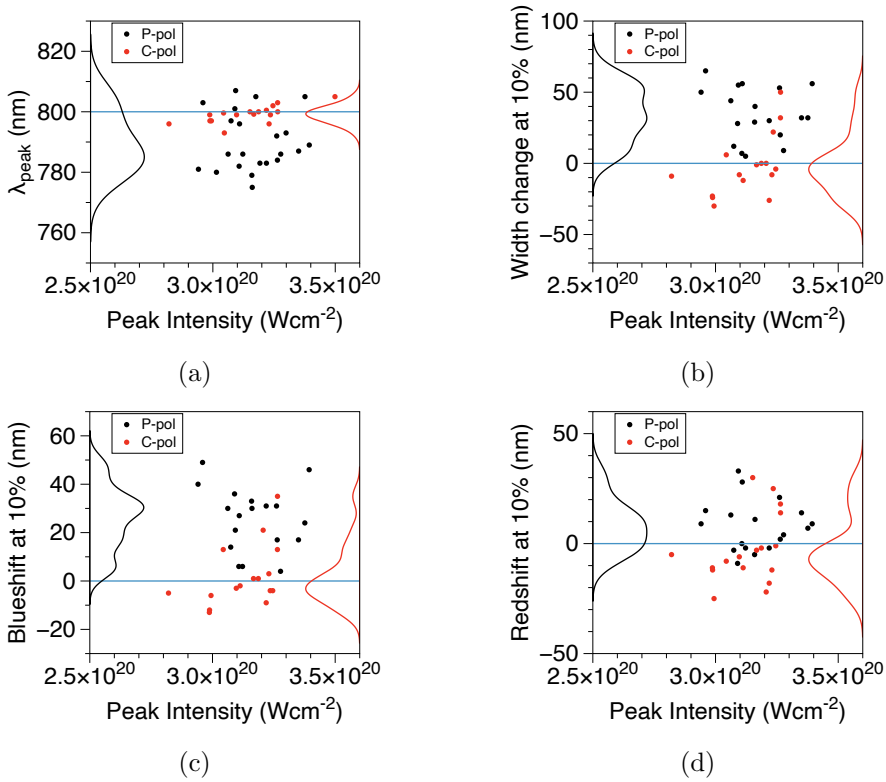

Figure 6.3: (a) Wavelength of peak signal of back-reflected light as a function of peak intensity on target, and input reference central wavelength denoted by blue line. (b) Change in spectral width relative to input reference spectra, measured at 10% of maximum signal. (c) Change in wavelength of blue edge of spectra relative to input reference spectra, measured at 10% of maximum signal. (d) Change in wavelength of red edge of spectra relative to input reference spectra, measured at 10% of maximum signal. Probability density functions of each laser polarisation are also shown, with curves with increasing value to the right in the case of p-polarised (black) and to the left in the case of c-polarised (red) .

the p-polarised light when compared to the c-polarised light. In the case of the spectra measured for c-polarised irradiation, the peak wavelength of the back-reflected laser light is located near to the 800 nm central wavelength of the incoming laser, with a relatively small degree of variation. However, in the case of the p-polarised laser light, there is a frequent, and significant blue-shift in the peak wavelength of the back-reflected light. Similarly, when measuring the change in the width of the spectra, measured as the full width at 10% of the maximum signal of the measured spectrum minus the full width at 10% of the maximum signal of the reference spectrum, shown in figure

6.3(b), around 25-50 nm of spectral broadening is seen relative to the input reference for the p-polarised light. In the case of the c-polarised light, however, the spectra are predominantly either unchanged, or narrowed with respect to the input reference spectra. When further analysing this measurement by separating the broadening into the wavelength on the blue side of the measured spectrum, minus the wavelength on the blue side of the reference spectrum, measured at 10% of the maximum, shown in figure 6.3(c), and the same for the red side, figure 6.3(d), it is seen that the blue side of the spectra for p-polarised light is frequently blue-shifted by 20-30 nm, whereas the spectra from the c-polarised light are typically more central around the reference wavelength.

6.4 Balance between thermal expansion and hole boring pressure

The experimentally-measured blue shift using p-polarised irradiation of thin foil targets that is observed in the back-reflected spectra, suggests that there is a degree of Doppler shifting in the light as it reflects from the critical plasma surface. To test this hypothesis, 1D EPOCH PIC simulations with a 1 nm spatial resolution were conducted to model the interaction between a Gaussian laser pulse with a FWHM pulse duration of 40 fs, and a central wavelength of 800 nm, and a near-solid density target (700 n_c), to approximate the experimental parameters. From these simulations, the temporal evolution of the electric field in the reflected direction was extracted and plotted, with the instantaneous wavelength shift as a function of time overlaid on top, as shown in figure 6.4.

The profile of instantaneous wavelength shift was determined by taking the spatial profile of the electric field of the pulse at a time step late on in the simulation relative to the point of reflection, so that it is fully separated from the plasma. This snapshot of the reflected pulse is then converted to the profile of the electric field in time by taking the velocity of the light to be c, and translating the spatial axis to time. The period, T, between each cycle of the electric field is then measured as a function of time, which can subsequently be converted to wavelength shift as a function of time via $\lambda = Tc$. The wavelength shift of the reflected pulse relative to the 800 nm central wavelength

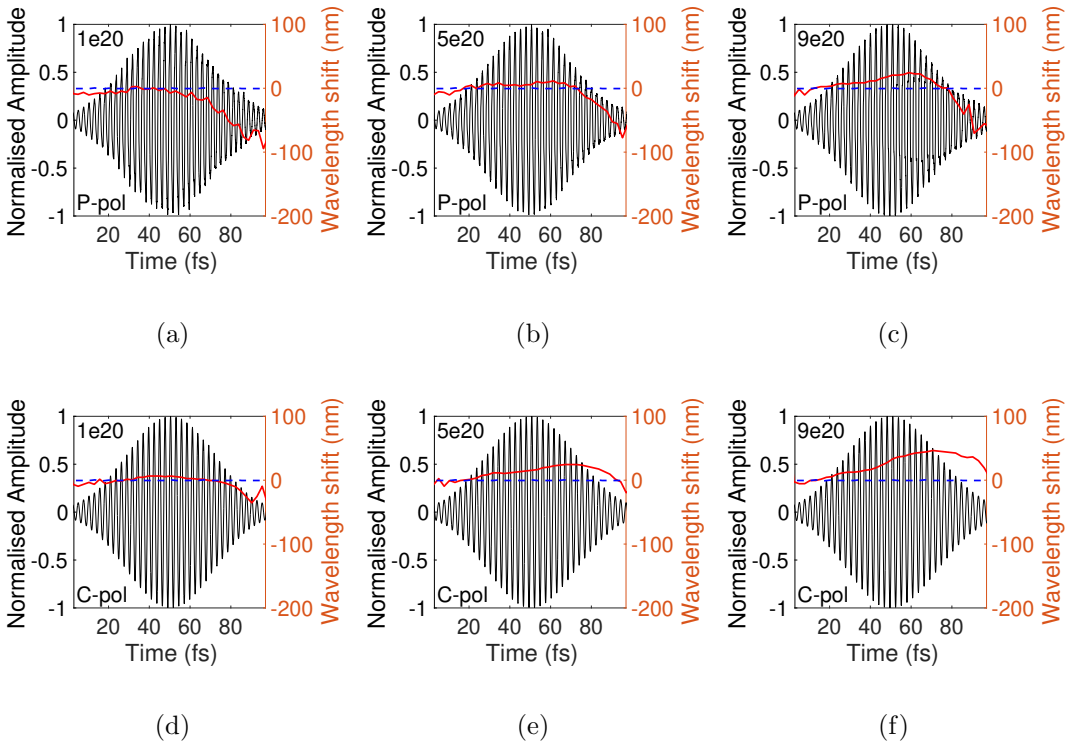

Figure 6.4: Plots from PIC simulations showing the change in wavelength (right-hand y-axis) as a function of time over the temporal evolution of a 40 fs FWHM pulse as it reflects from the plasma surface, with the electric field amplitude normalised to the maximum on the left-hand y-axis. Plots for p-polarised light (a-c), and c-polarised (d-f), and increasing intensity left to right (as quoted in each plot in units of Wcm^{-2}). Dashed blue line denotes zero wavelength shift, such that a red-shift lies above this line, and a blue-shift lies below.

of the incoming pulse as a function of time is plotted, along with the corresponding electric field profile for both p-polarised and c-polarised light, for laser intensities of 1×10^{20} Wcm^{-2}, 5×10^{20} Wcm^{-2}, and 9×10^{20} Wcm^{-2}, in figure 6.4.

From these plots, it can be seen that in the case of the c-polarised light, a red-shift in the wavelength (denoted by a positive shift value) is induced across the profile of the reflected pulse, which increases in magnitude as the laser intensity increases due to the strong radiation pressure that is produced by circularly polarised light. In the case of the p-polarised light (a-c) however, the behaviour in the wavelength shift across the reflected pulse is significantly different to what is seen with the c-polarised light

(d-f). As the laser intensity increases, an increase in the magnitude of the hole boring red-shift is seen once again, albeit with only around half as much of a shift compared to the c-polarised case. The more prominent feature, however, is the large blue-shift that is induced after $\sim$ 80 fs. These shifts in the wavelength of the pulse as it reflects from the target plasma show that the reflected light is gaining a chirp as it interacts with the plasma. In the case of the p-polarised light, the large blue-shift of 50-100 nm at the tail end of the pulse (after $\sim$ 80 fs) suggests that it is obtaining a red-to-blue, or up-chirp. For the c-polarised light, the strong red-shift of up to 50 nm generated by the laser radiation pressure is imparting a blue-to-red, or down-chirp into the reflected pulse.

The rapid blue-shift in the tail of the pulse suggests that there is a significant outward expansion of plasma, and therefore of the reflective critical surface, that is occurring towards the end of the interaction with the laser pulse. A possible explanation for this expansion in the case of the p-polarised light, is that the plasma is being heated to a much greater degree than with the c-polarised laser, leading to a significant increase of thermal pressure within the plasma which drives a rapid expansion out into vacuum, as described in section 2.8. This is consistent with what would be expected from theory, as the p-polarised light will lead to strong $J \times B$ heating, expanding the plasma, whereas in the c-polarised case this does not occur as discussed in section 2.7.

Outwards expansion of plasma can be seen when analysing time-space plots of the plasma density normalised to the critical density, as shown in figure 6.5. Here the evolution of the plasma density as a function of 1D space and time can be seen for both p-polarised and c-polarised light, and for increasing peak laser intensity. In these plots, the plasma density normalised to the relativistically corrected critical density is shown on a logarithmic scale, such that the reflective critical surface is denoted by the transition from pale blue to yellow on the colour bar, where $\log(n_c) = 0$, and the laser enters the simulation from the left (negative side of spatial scale). In the case of the p-polarised laser, for a peak intensity of 1×10^{20} Wcm^{-2} it is seen that when the particle motion is initialised at $t = 0$ fs, the critical surface expands outwards from the target fairly slowly relative to later in the simulation, and then as the intensity

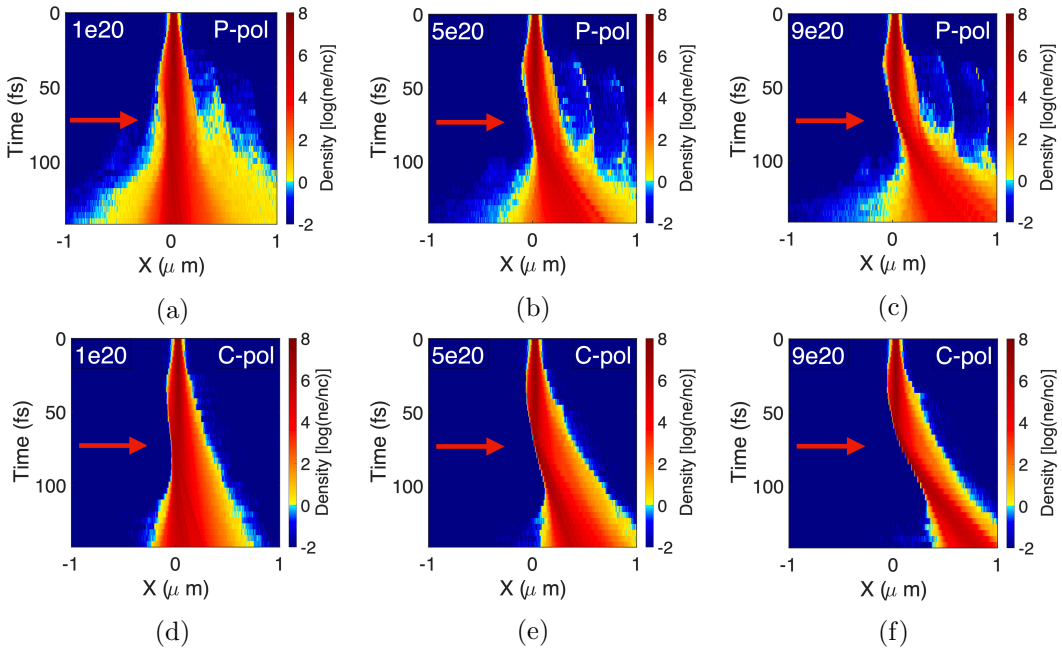

Figure 6.5: 1D simulation time-space plots showing the electron density evolution of a target when irradiated by a 40 fs FWHM Gaussian temporal intensity profile laser pulse, where the laser is incident along the positive X direction. Plots for p-polarised light shown (a-c), and c-polarised (d-f), with peak intensity increasing left to right (as quoted in each plot in units of Wcm^{-2}). Red arrow denotes laser direction.

of the laser increases to its maximum at $t = 65$ fs, the outwards expansion of the plasma is impeded by the radiation pressure of the laser. As the intensity of the laser, and therefore the radiation pressure exerted on the plasma starts to drop, the plasma critical surface resumes its outwards expansion at a rate significantly greater than when the simulation was initialised, as the plasma temperature, and therefore the thermal pressure, is significantly higher. This suggests that there is a balance of two opposing forces; the inward radiation pressure exerted on the critical surface by the laser, and the thermal pressure of the plasma pushing in the opposite direction. Both these forces will vary as a function in time, as the radiation pressure of the laser will vary with the Gaussian temporal intensity profile of the pulse, and the thermal pressure will vary in time as the plasma electrons are heated by the laser.

As the intensity of the p-polarised pulse is increased, the evolution in time of the balance between these two opposing forces changes, as can be clearly seen in the case

of the 9×10^{20} Wcm^{-2} simulation, shown in figure 6.5(c). Here, once again the plasma begins to slowly expand outwards by ~ 50 nm after $t = 0$ fs, but as the intensity of light irradiating the plasma increases, the inwards radiation pressure grows quicker than the outwards thermal pressure, leading to the critical surface of the plasma being pushed forwards into the target. Once the radiation pressure of the laser begins to drop (as the intensity of irradiating light decreases on the falling edge of the pulse), the balance between the two forces switches to be in favour of the outwards thermal pressure, driven by the heating action of the laser. This can be seen in the rapid switch in direction of the motion of the critical surface at ~ 100 fs in figure 6.5(c), as it reverses direction and quickly expands outwards.

In the case of the circularly-polarised light, the balance between these two opposing forces is significantly different. For a c-polarised pulse with a peak intensity of 9×10^{20} Wcm^{-2}, the rising radiation pressure exerted on the plasma by the laser causes the critical surface to be driven forwards into the plasma, as seen in the p-polarised case. In this case, however, the outwards thermal pressure of the heated plasma is significantly reduced and does not overcome inwards radiation pressure as the laser intensity drops. This is consistent with the theory of circularly-polarised light not driving the strong oscillations in the motion of the plasma electrons that a linearly-polarised laser does, leading to a much lesser degree of plasma heating.

The difference in the balance between these opposing forces for the two polarisation cases can also be observed by plotting the total kinetic energy of the plasma electrons as a function of time and the laser intensity, and therefore radiation pressure, as a function of time. This is shown in figure 6.6 for a 50 nm target. When the total kinetic energy of the plasma electrons at each time step is plotted during the interaction of the laser pulse and the plasma, it is seen that for both polarisations the total energy increases to ~ 100 MeV as the particle motion in the simulation is initialised. However in the case of the circularly-polarised pulse, the total kinetic energy of the electrons does not increase by a significant degree during irradiation by the laser. In the case of the p-polarised laser however, a significant degree of plasma heating is indeed observed, as the total kinetic energy of the electrons increases by an additional ~ 2.5 orders of

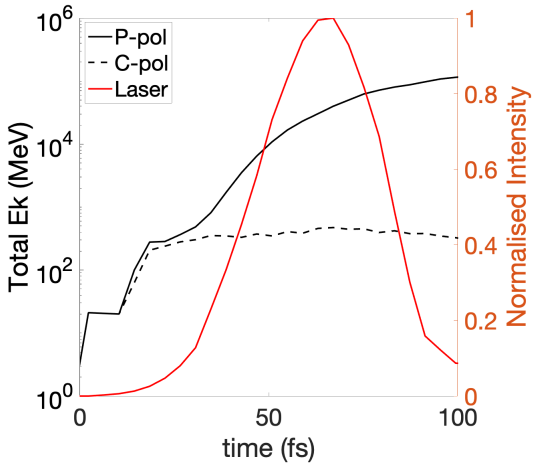

Figure 6.6: Plot from PIC simulations of the total electron kinetic energy as a function of time during the interaction of both a p-polarised and a c-polarised laser pulse and a 50 nm target. Temporal evolution of laser intensity normalised to the maximum shown in red.

magnitude as the plasma is irradiated by the pulse. In addition, it can be seen that in the case of the linearly-polarised laser light, as the intensity of the pulse drops, the plasma electrons continue to gain kinetic energy as the build up of kinetic energy within the plasma drives the outwards expansion of the front surface. In the case of the circularly-polarised light this does not occur, and as the laser intensity begins to drop, the kinetic energy of the electrons starts to decrease.

Thus far, only a 1D simulation approach to modelling the interactions has been employed, which does not give a complete picture of how the reflected pulse is chirped by the motion of the plasma critical surface during reflection of the laser, as the interaction is limited in its spatial degrees of freedom. In order to explore the influence of an additional spatial dimension, a series of 2D simulations were conducted. These consisted of a 65×10 μm box, of spatial resolution 2 nm. A plasma 50 nm in thickness and with an electron density of 700 n_c was added, and a 50 fs FWHM laser pulse with either linear or circular polarisation, and with peak intensity of either 1×10^{20} Wcm^{-2} or 9×10^{20} Wcm^{-2}, was propagated into the simulation box.

For each case, the instantaneous wavelength shifts of the reflected pulse as a function of time was calculated via the same method as before, and are shown in figure 6.7.

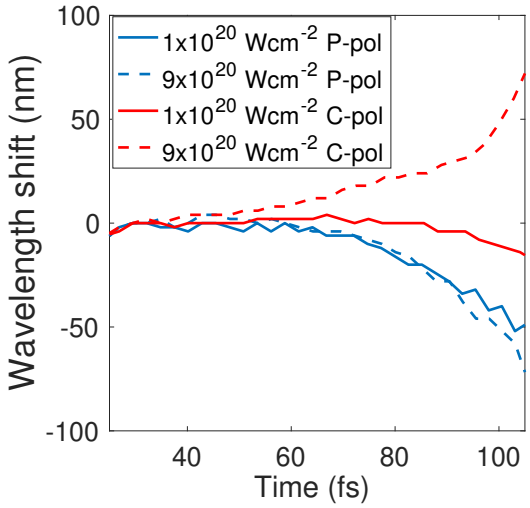

Figure 6.7: Plot from 2D PIC simulations, showing the change in wavelength as a function of the temporal evolution of a 40 fs FWHM pulse as it reflects from the plasma surface, for 1×10^{20} Wcm^{-2} and 9×10^{20} Wcm^{-2}, for both p and c polarisations.

Comparing these simulations to the results shown previously in figure 6.4 for the 1D simulations, it can be seen that the instantaneous wavelength shift of the reflected pulse for each laser polarisation and intensity is slightly different when the simulations are conducted in 2D, although the overall behaviour is similar. In the cases involving a p-polarised pulse, it is seen that, similarly to the 1D simulations, the reflected pulse becomes increasingly blue-shifted by up to $\sim$ 50 nm with time due to the outwards expansion of the plasma critical surface. In the case of the 2D simulations however, the initial redshift in the higher intensity p-polarised case is not present as in the 1D case. This implies that the hole-boring into the target was exaggerated by the restricted degrees of freedom, since the particles could only move in one axis. In the case of the circularly polarised simulations, again similar behaviour is seen in the 2D cases as in the 1D simulations, with the hole-boring pressure and thermal pressure approximately balancing each other for the 1×10^{20} Wcm^{-2} peak intensity case, and for the 9×10^{20} Wcm^{-2} case, a strong degree of red-shifting of up to $\sim$ 70 nm of the reflected pulse due to the hole-boring velocity.

Although there are some differences displayed in the 2D simulations compared to

1D, the key features of a strong degree of blue-shifting in the p-polarised cases, and strong red-shifting in the c-polarised cases are still seen in the 2D simulations. This is highly encouraging as it demonstrates that these behaviours are not simply an artefact of simulating the interactions in only one spatial dimension, but are reproducible as the number of dimensions are increased.

6.5 Influence of self-phase modulation

As well as this spectral broadening of the back-reflected spectra, the presence of spatial structuring in some of the spectra was also observed. As mentioned in section 6.1, the experimental measurements of the wavelength spectrum of the back-reflected light were made by passing a pick-off of this component of reflected light out through a window in the chamber, which was then directed to an optical spectrometer. As was discussed in section 2.2, as an intense pulse of light propagates through a material, such as glass, the pulse will undergo self-phase modulation (SPM) due to the variation in the refractive index of the material, induced by the optical Kerr effect [159]. Despite the measurements being made from a small area, as sampled by a 1 inch pick-off of the edge of the back-reflected beam, there is still a significant intensity ($> 10^{10}$ Wcm^{-2}) of laser light that is passing through the glass window. This means that the spectrum of the back-reflected light could be modified by SPM prior to being captured by the spectrometer, resulting in the measurement being altered.

Looking at two example spectra, we can see some of the characteristic features of SPM, as shown in figure 6.8. In each of these spectra, a different characteristic feature of SPM is seen; in the plot for the p-polarised case (a), a central peak with a lower amplitude peak at either side is displayed, whereas in the c-polarised case (b), the central wavelength in the spectrum has been hollowed out, both of which are well documented features of SPM [160–162]. For both of these shots, the experimental parameters are nominally identical, other than the polarisation of the laser light. As discussed previously, the interaction between the inward radiation pressure of the laser pulse and the outward thermal expansion of the plasma, and how the balance between

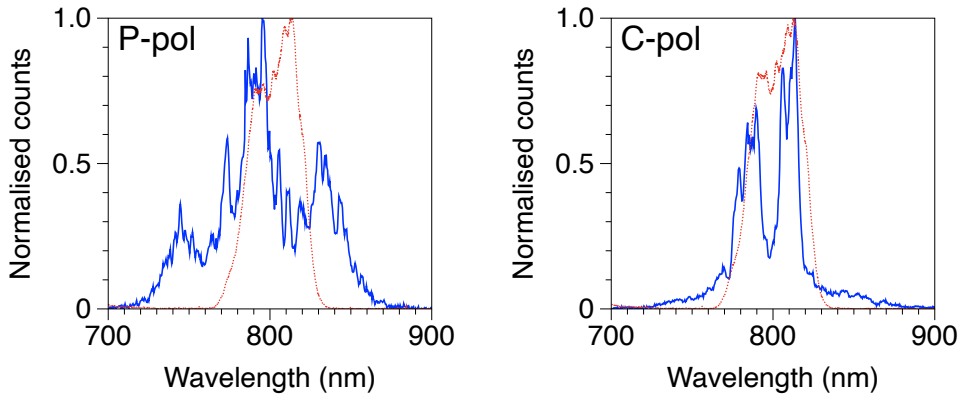

(a) (b)

Figure 6.8: Plots of measured spectra of back-reflected light displaying features associated with SPM. (a) Spectrum measured from back refected light from the interaction of a 40 nm target with a p-polarised pulse which displays a central peak with a lower amplitude wing on each side. (b) Spectrum measured from back-reflected light from the interaction of a 40 nm target with a c-polarised pulse which displays hollowing at the central wavelength. Reference input spectrum in both cases shown in red.

these forces is different for the two interaction conditions, results in reflected pulses of each polarisation with different directions of wavelength chirp.

A simple model was developed to investigate how the spectrum of a chirped Gaussian pulse would be altered by SPM as it propagates through 2.5 cm of glass, i.e. the window of the chamber used in the experimental measurements. This was done by using the derivation of self-phase modulation given in section 2.2, and by considering the laser pulse to be in the form of amplitude $\times$ phase, and the phase to be given by:

$$exp\left(i\left(\omega_{SPM} + Bt\right)\right) \tag{6.1}$$

where ω_{SPM} is the self-phase modulated frequency, given previously in equation 2.6, and B is the chirp parameter, either positive or negative. The intensity of laser light passing through the glass in the model was chosen to be similar to the intensity on the window in the experiment. This was calculated by taking the intensity expected experimentally on the front surface of the target, assuming a reflectivity of 40 %, and scaling the beam diameter up to 20 cm as to match the beam diameter immediately prior to the pick-off

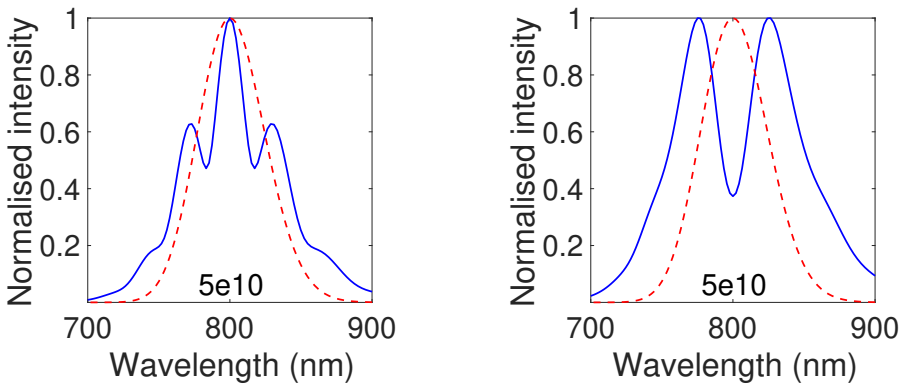

(a) (b)

Figure 6.9: Plots of the results of modelling the influence of SPM on a chirped pulse with an intensity of 5×10^{10} Wcm^{-2} passing through 2.5 cm of glass. (a) Spectrum of a Gaussian input pulse with an up-chirp after undergoing SPM. (b) Spectrum of a Gaussian pulse with a down-chirp after undergoing SPM. Reference input spectrum in both cases shown in red.

optic in the experimental setup. As shown in figure 6.9, when a Gaussian pulse with a FWHM pulse duration of 40 fs and an intensity of 5×10^{10} Wcm^{-2}, equal to that estimated to have passed through the window in the experimental case, is propagated through the glass, structures similar to those measured experimentally are observed to form in the modelled spectrum. The difference between the spectra calculated from the model is simply the direction of the chirp placed on the input Gaussian pulse, i.e. the sign of B in equation 6.1. The plot in 6.9(a) results from passing a pulse with an up-chirp through the glass, and closely matches the spectrum measured experimentally for a p-polarised pulse as shown in figure 6.8(a), expected to undergo an up-chirp due to the thermal expansion of the plasma. Similarly, the plot in figure 6.9(b) results from a down-chirped pulse passing through the glass in the model, and closely matches the measured spectrum from the c-polarised laser in figure 6.8(b), which is predicted to undergo a down-chirp due to the inward radiation pressure.

In addition, as the intensity of the light passing through the glass in the model is increased between 1×10^{10} Wcm^{-2} and 9×10^{10} Wcm^{-2}, the extent of the modulation of the spectrum due to SPM becomes more extreme, as shown in figure 6.10. The key difference in the spectra between the two directions of chirp is the depletion of the

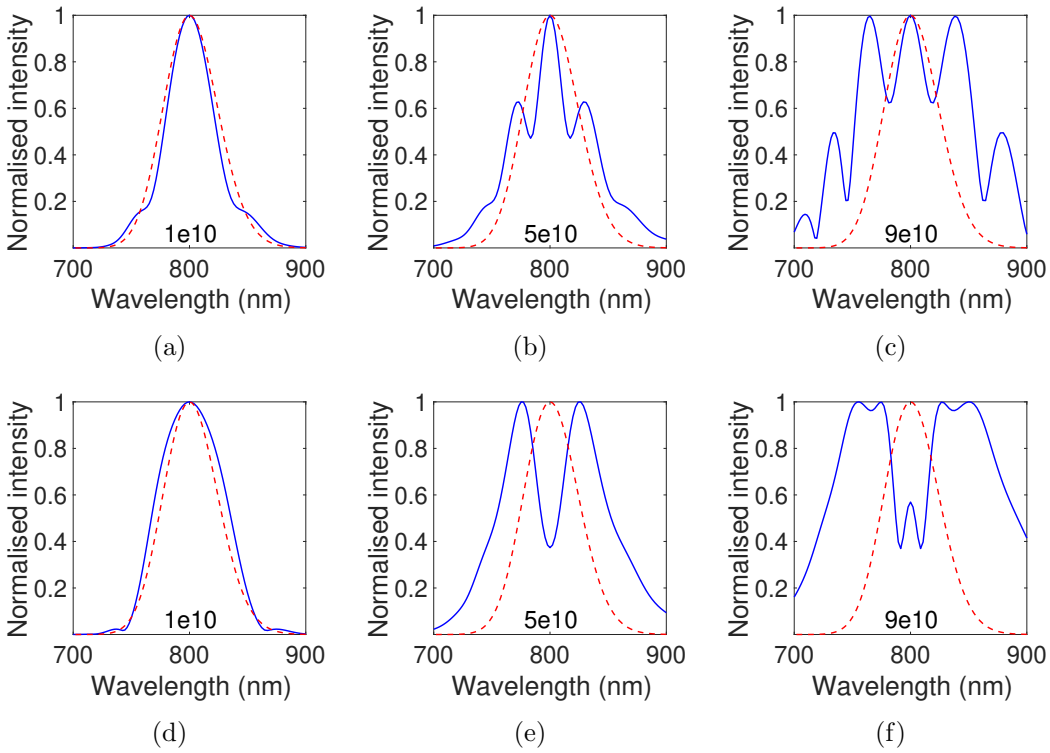

Figure 6.10: Plots showing the results of modelling the influence of SPM on a chirped input pulse passing through 2.5 cm of glass for increasing laser intensity (as quoted in each plot in units of Wcm^{-2}). Top row is for an up-chirp (negative chirp parameter), and bottom row is for a down-chirp (positive chirp parameter). Reference input spectrum in each case shown in red.

peak at the 800 nm central wavelength when the pulse possesses a down-chirp, but the evolution of the spectral structuring with increasing intensity differs as well. In the case of the up-chirped pulse (a-c), as the peak intensity of light passing through the glass increases, SPM quickly acts to generate additional peaks radiating out from the central wavelength with a fairly high spatial frequency (approximately every 30 nm), whereas in the down-chirped case (d-e), the spectrum is less prone to the development of satellite peaks with respect to an increase in peak intensity, and instead broadens with a depleted central wavelength.

6.6 Conclusion

In this chapter, the broadening and shifting of the spectrum of back-reflected laser light from the irradiation of thin, 40 and 50 nm foil targets has been investigated. A possible explanation for this behaviour has been given by modelling, through PIC simulations, how the interaction between the inward radiation pressure and outward thermal pressure lead to an evolution in the direction of chirp as the pulse is reflected from the plasma critical surface, and can induce either a net up-chirp or down-chirp, depending on which force dominates. This hypothesis is similar to that in work carried out by M. Streeter [163], where the motion of the plasma front surface is measured through use of frequency-resolved optical gating (FROG). Here, experimental data measured on Gemini is presented, and the temporal evolution of motion of the the reflective surface of the plasma is estimated, but as a function of target thickness rather than intensity. This study found a similar interplay between the outwards thermal pressure and the inwards radiation pressure, when considering the interaction of a p-polarised, 50 fs pulse with solid targets. In this case, the balance between these two forces was found to change depending on the target thickness, and with thick targets a significant net blue-shift of the reflected laser light was measured. For thin, < 100 nm targets, this previous study found that a net red-shift is measured after irradiation by a p-polarised pulse. However, the measurements made were only able to be resolved for a window of time of $\pm$ 30 fs relative to the peak of the pulse. It is likely therefore, that the blue-shifting demonstrated in this chapter is a result of the sampling time extending later in time, and capturing more of the thermal expansion after the radiation pressure from the laser has ended.

In addition, the influence of self-phase modulation has been observed in some of the spectra measured experimentally, and has been replicated by employing a simple model. The two spectral profiles, distinctive of SPM that were observed experimentally can be linked to the polarisation of the laser, due to the differing direction of chirp that is induced with p-polarised and c-polarised light.

The observation of these spectral profiles experimentally, could potentially be em-

ployed as a method of probing the direction of motion of the critical surface of the plasma as an ultra-intense laser pulse reflects from the target, as the significant differences in the self-phase modulated spectrum are indicative of the direction of this wavelength chirp. Additionally, by observing the extent of the modulation in the back-reflected spectrum, it may be possible to use SPM as a means of probing the plasma reflectivity and thus the energy content of the back-reflected light on a shot-to-shot basis by choosing a specific thickness of glass, such that the onset of SPM in the spectra is at the bottom end of the range of intensities expected to be propagating through the glass. Subsequently, any increase in the intensity of back-reflected light passing through the glass should result in a visible modulation of the spectrum, and the degree of this modulation could be used as a means of estimating the intensity of the light, and by extension the reflectivity of the plasma. Further work into determining how sensitive this method is to changes in the laser intensity, and therefore what magnitude of intensity change can be resolved, would be a highly beneficial avenue of further study.

Furthermore, if it is desired to preserve the spectrum of the back-reflected light as much as possible, such that any further analysis being conducted can be done with spectra which have not been modified, then this study highlights that steps must be taken to reduce any possible self-phase modulation. Even the act of passing the light through the glass in a target chamber window, as is often done, can significantly alter the spectral profile of the reflected pulse, potentially leading to increased spectral broadening, that is not attributed to the dynamics of the laser-plasma interaction.

Chapter 7

Conclusions and future work

This thesis presents work carried out both experimentally, and through a variety of numerical modelling techniques, that focusses on studying a variety of methods of optically diagnosing the evolution of the dense plasma during the interaction with an ultra-intense laser pulse. The key findings from each of the results chapters, along with a discussion into ways the work could potentially be expanded on in the future, is provided in this chapter.

7.1 Diagnosing plasma electron temperature and laser focal size via analysis of specularly-reflected light from microstructured solid targets

In chapter 4, measurements of the light specularly reflected from the front surface of microstructured solid targets, during irradiation by an ultra-intense laser pulse are presented, and the behaviour of spatial structuring in both the 1ω and 2ω light investigated. It is demonstrated that this spatial structuring in the specularly reflected light arrises due to the spatial profile of the microstructured target surface, and that in the case of a target with parallel grooves etched into the front of the target, the reflected light contains a pattern of bright and dark regions aligned to the orientation of the target grooves. Furthermore, through numerical modelling, it is shown that the

spacing between the maxima is related to the spatial profile of these groove structures, as this profile is varied from a sharp, square-wave distribution resembling the unexpanded target, to a smooth sinusoidal profile, resembling a thermally-expanded target. In addition, it is shown that the evolution of this groove profile during the thermal expansion induced by irradiation of the laser, is dependent on the temperature of the plasma electrons within the region of the laser focal spot. Through the combination of the link between the separation of reflected maxima and the spatial profile of the expanded groove structures, and the link between this profile of the grooves and the plasma electron temperature, a model describing the relationship between the observed spacing in reflected maxima, and the plasma temperature reached within the focal region of the laser has been explored. In the case presented in chapter 4, when observing the 2ω light, this model suggests that a plasma temperature of 28 keV is reached within the laser focus, at the peak intensity of the pulse.

The use of the structuring in the specularly reflected light as a means of estimating the on-shot focal spot size, which could be done by utilising targets with a specifically designed periodicity of structuring was also explored.. These findings are of great interest, as measurements of the plasma temperature limited to only the focal region of the laser, and the focal spot size during a full-power shot, are both exceedingly difficult to achieve by other means. The use of microstructured targets, along with this modelling, could prove to be a highly useful method of characterising the laser focal spot at the beginning of a laser-solid experiment.

7.1.1 Future work

In the future, this work could be built upon experimentally, and the use of such microstructured targets could be tested by taking a number of shots at different incident energies, and therefore intensities, and observing if the specularly reflected light, in conjunction with this model, suggests a variation in the achieved plasma temperature as laser intensity is changed. This would add additional confidence in the proposed technique, and enable the model to be refined as a diagnostic method for future experimental use. In addition, other microstructure geometries could be investigated to

test if the performance of the diagnostic technique can be improved by, for example, increasing or decreasing the structure spacing, or changing from a groove structure to something else. The limits of the technique could also be determined, by finding the maximum and minimum spacings required for the method to work. Also, different target materials could be tested, potentially allowing for the technique to be applied to experiments involving higher peak laser intensities, perhaps by aiming to slow down the rate of deformation of the microstructures, thereby allowing them to retain their shape for longer.

The proposed method for determining the focal spot size during a full-power shot could potentially be built upon in a similar way by testing different structure geometries, and be developed into an experimental technique to be used in conjunction with existing methods of characterising the size of the focal spot of the laser at low power, to bring a new degree of robustness to the characterisation of the focused laser pulse during an experiment. Both of these techniques, when developed further, could aid the measurement of properties of both the laser pulse and the plasma, and bring new insight into the dynamics of the resulting interaction.

7.2 Analysis of the spatial-intensity distribution of laser light transmitted through a plasma aperture

In chapter 5, experimental results exhibiting the formation of stripe patterns in the laser light transmitted through a target undergoing relativistic self-induced transparency, as imaged on a scatter screen, were analysed and modelling was carried out to attempt to ascertain their source. The spatial separation of these stripes, and their angle relative to the vertical is analysed, and compared to changes in the laser properties, such as percentage of transmission, energy, and defocus distance. Additionally, the probability of the appearance of these stripes as a function of a variety of laser and target parameters, such as target thickness, laser energy, and defocus distance was discussed.

In order to investigate the source of the formation of these stripe patterns, particle-in-cell simulations and ray tracing modelling are performed to determine if the structur-

ing in the transmitted light formed due to diffraction as the laser propagated through a plasma aperture, and subsequently, how the size, ellipticity, and angle of this aperture would influence the spatial distribution of these stripes. It is demonstrated that, by varying these physical parameters of the aperture, the spacing and angle of the stripes could be directly influenced, and the resulting spatial profile of the structures is found to closely resemble that observed experimentally. The results of this modelling pointed to the process of aperture diffraction as being the source of the stripe patterns. However it is found that the intensity distribution of the stripes that were measured experimentally did not accurately match that demonstrated by the numerical modelling. Instead, it is found that the intensity of the stripes as measured experimentally, have a more level distribution than the Gaussian distribution expected from diffraction theory, and following from this, some alternative hypotheses of the source of the stripe patterns are considered.

7.2.1 Future work

In order to validate or rule out the alternative hypotheses for the experimentally measured spatial distribution in the transmitted laser light, the next step would be to establish the experimental parameters needed to consistently produce the stripe patterns in the transmitted light. A future experiment would therefore start off by taking a relatively large number of shots on thin foil targets of around 50 nm in thickness, comparable to those used previously. This would, however, likely be expensive to do due to the single-shot nature of systems such as the Vulcan and PHELIX lasers. The laser parameters would be kept constant for these shots, with p-polarisation, and at normal incidence to the target, allowing for the frequency of occurrence of the stripes to be established for these nominal conditions. Once a substantial dataset with these initial conditions has been acquired, the effect of changing parameters such as target thickness, and laser energy could be investigated to determine which conditions are required for the onset of pattern formation. In addition, the size of the laser focal spot could be varied, driving different diameters of apertures in the plasma. From this, it could be investigated if the pattern generation is dependent on the size of the plasma

aperture, and if the distribution of the pattern varies with increasing aperture diameter, as we have modelled.

The dependence of the stripe patterns on the ellipticity of the aperture could be experimentally investigated by taking a series of shots at increasing target angles relative to the laser axis, which would result in the spatial distribution of the focal spot being stretched into an ellipse. From this, the extent to which the elongation of the stripes depend on the the aperture shape could be determined, and if the stripes transition from an Airy disc pattern to a pattern containing vertical stripes. Finally, the influence of the rotational angle of an elliptical aperture could be tested by deliberately inducing an astigmatism in the elliptical aperture, by either having a fixed degree of astigmatism and scanning the position of best focus of the laser along the laser axis as described previously, or by using an adaptive optic system, such as a deformable mirror, to manually control the shape of the focal spot.

These proposed investigations would test the initial hypothesis that the patterns are formed by simple aperture diffraction, and would aim to replicate the behaviour expected from the various components of the modelling that has been carried out. If these experimental tests do not replicate the stripe patterns, or are not able to control their behaviour, then further studies could be carried out to investigate the feasibility of the hypotheses that have been discussed suggesting that two-source interference could be the cause of the formation of these patterns.

7.3 Spectral analysis of back-reflected light and the dependence of target heating and expansion on laser polarisation

In chapter 6, experimental measurements of the spectra of back-reflected laser light from the irradiation of 40 and 50 nm-thick foil targets are analysed, and the spectral shifting and broadening present in the spectra is discussed. It is found that when comparing spectra from shots with comparable laser and target parameters, but differing laser polarisations, shots with p-polarised irradiation display significant spectral broadening

and blue-shifting of around 25-50 nm relative to the input spectrum, but for c-polarised irradiation, the width of the spectra remains largely unchanged. Following from this, PIC simulations are utilised to determine if the blue shift in the spectra measured with p-polarised irradiation can be explained by Doppler shifting in the pulse as it reflects from the backwards-expanding surface of the plasma late in the interaction after the peak of the laser pulse. These simulations show that there is a significant blue shift induced in the reflected pulse in the case of p-polarised light, and a red shift in the case of c-polarised light, and that these shifts become more extreme as the laser intensity is increased. Furthermore, the temporal evolution of the plasma density shows that after an initial inwards compression, the critical surface on the front of the target subsequently begins to rapidly expand outwards, against the propagation direction of the laser, in the case of the p-polarised irradiation, but in the case of the c-polarised irradiation, this rapid outwards expansion is suppressed by the inwards radiation pressure of the high intensity laser light.

As well as the analysis of the spectral shifting, numerical modelling was carried out to investigate the source of the self-phase modulation in the reflected laser spectra, as this was observed in some of the spectra recorded experimentally. It is found that by passing a chirped pulse through 2.5 cm of glass, representative of the window in the target chamber that the measured laser light passes through, the resulting spectra is subject to self phase modulations with the two distinct spectral profiles that were observed. The difference in the input parameters that is needed to change between the two distinct spectra, is found to be simply the direction of chirp applied. Through the modelling, the direction of chirp is, in turn, seen to be determined by the polarisation of the laser irradiating the target, which correlates with the experimental data that was recorded.

The results are discussed in the context of potentially using the measurements of the spectral shifting as a means of probing the direction of motion of the plasma critical surface, which is a measurement that is difficult to make by other means. In addition, the presence of self-phase modulation in the spectra is discussed as a potential way of estimating the plasma reflectivity, and the energy contained in the backwards-reflected

laser light. This can be achieved by choosing a thickness of glass to propagate the light through, such that the onset of self-phase modulation lies at the lower end of the intensities expected to propagate through the glass. Any increase in the energy content of the back-reflected laser light, and therefore the intensity passing through the glass, could then be detected by observing the increasing modulation of the spectrum relative to a low intensity pulse.

7.3.1 Future work

The study could be further developed in the future by making more measurements of the back-reflected spectra for shots over a larger range of laser intensities, and determine if more definitive trends between laser intensity and the magnitude of spectral shift can be made. This would provide additional experimental confirmation of the interplay between the outwards thermal expansion of the heated plasma, and the inwards hole boring of the laser. In addition, development of the potential use of the presence of self-phase modulation as a diagnostic tool for estimating plasma reflectivity and back-reflected laser energy, by measuring the spectra of the back-reflected laser light as a function of laser intensity and characterising how the modulation of the spectrum changes as the intensity is increased. The effect that changing the thickness of the glass, or switching to a different material entirely, has on the modulation of the spectra could be characterised. By changing the thickness of glass, or type of material, that is being used to propagate the back-reflected pulse through, the minimum intensity required for the onset of self-phase modulation could be tailored, allowing for different laser intensity regimes to be probed. With further testing into how sensitive the observable changes in the spectrum are to changes in the intensity, this could potentially be developed into a diagnostic technique that could be employed on future experiments, as a method for estimating back reflected laser energy which is simple to set up and run, and could be run in conjunction with other techniques, to further bolster the measurements being made.

7.3.2 Summary

The new results presented in this body of work highlight the potential for further development of optical probing techniques to provide new insights into high power laser plasma interactions. It shows that such techniques could be developed to diagnose the size of the laser focus on a high power shot (present techniques are limited to indirect diagnosis of X-ray emission) or to determine the temperature of the plasma in the region of highest intensity, when used in conjunction with reference structured targets. It also shows that the diffraction of intense laser light when propagating through a self-generated relativistic plasma aperture can be used to diagnose the shape and size of the aperture and thus probe the evolution of this plasma feature. New techniques such as this will become even more important at the higher intensities achievable with multipetawatt scale laser facilities coming on-line, because even near-solid density targets start to become relativistically transparent. It also shows that optical spectral measurements can be used to infer the motion of the plasma critical surface within the duration of the laser pulse, as well as the reflectivity of the plasma. If developed further, these new optical techniques will aid future studies undertaken into this field of research.

Bibliography

[1] A. Einstein. "Zur Quantentheorie der Strahlung". Physikalische Zeitschrift. **18** 121–128 (1917).

[2] T. H. Maimen. Stimulated Optical Radiation in Ruby. Nature, **187**, 4736, 493-494 (1960).

[3] F. J. McClung, *et al.* Giant optical pulsations from ruby. Journal of Applied Physics, **33** 828–829 (1962).

[4] L. E. Hargrove, *et al.* Locking of He-Ne laser modes induced by synchronous intracavity modulation. Applied Physics Letters, **5** 4–5 (1964).

[5] D. Strickland and G. Mourou. Compression of amplified chirped optical pulses. Optics Communications, **55**, 6, 447–449 (1985).

[6] S. W. Bahk *et al.* Generation and characterization of the highest laser intensities (10^{22} W/cm^2). Optics Letters, **24**, 29 (2004).

[7] J. W. Yoon *et al.* Achieving the laser intensity of 5.5×10^{22} W/cm^2 with a wavefront-corrected multi-PW laser. Optics Express, **15**, 27 (2019).

[8] B. Rus *et al.* Eli-beamlines: Progress in development of next generation short-pulse laser systems. Proceedings SPIE, Research Using Extreme Light: Entering New Frontiers with Petawatt-Class Lasers III, (102410J) (2017).

[9] P. R. Drake. "Introduction to High-Energy-Density Physics". Springer (2006).

[10] G. Gregori *et al.* Generation of scaled protogalactic seed magnetic fields in laser-produced shock waves. Nature, **481**, 7382, 480 (2012).

[11] D. A. MacLellan, D. C. Carroll, *et al.* Tunable mega-ampere electron current propagation in solids by dynamic control of lattice melt. Physical Review Letters, **113**, 18, 185001 (2014).

[12] J. Nuckolls *et al.* Laser Compression of Matter to SuperHigh Densities: Thermonuclear (CTR) Applications. Nature, **239**, 5268, 139-142 (1972).

[13] J. D. Lawson. Some criteria for a power producing thermonuclear reactor. Proceedings of the Physical Society. Section B, **70**, 6 (1957).

[14] M. Tabak *et al.* Ignition and high gain with ultrapowerful lasers. Physics of Plasmas, **1**, 5, 1626–1634 (1994).

[15] R. Kishoni and D. Shvarts. Ignition condition and gain prediction for perturbed inertial confinement fusion targets, Phys. Plasmas **8**, 4925 (2001).

[16] J. D. Lindl, Development of the indirect-drive approach to inertial confinement fusion and the target physics basis for ignition and gain. Physics of Plasmas, **2**, pp. 3933-4024 (1995).

[17] https://home.cern/resources/faqs/facts-and-figures-about-lhc (accessed 12/01/2021)

[18] T. E. Cowan *et al.* Ultralow emittance, multi-MeV proton beams from a laser virtual-cathode plasma accelerator. Physical Review Letters, 92, **20**, 204801 (2004).

[19] E. L. Hatchett *et al.* Electron, photon, and ion beams from the relativistic interaction of Petawatt laser pulses with solid targets. Physics of Plasmas, **75**, 2076 (2000).

[20] R. A. Snavely *et al.* Intense high-energy proton beams from Petawatt-laser irradiation of solids. Physical Review Letters, **85**, 2945 (2000).

[21] C. A. Tobias *et al.* Pituitary irradiation with high-energy proton beams a preliminary report. Cancer Research, **18**, 121–134 (1958).

[22] M. Goitein and M. Jermann. The relative costs of proton and x-ray radiation therapy. Clinical Oncology, **15**, S37–S50 (2003).

[23] S. V. Bulanov*et al.* Interaction of an ultrashort, relativistically strong laser pulse with an overdense plasma. Physics of Plasmas, **1**, 745–757 (1994).

[24] B. Dromey *et al.* High harmonic generation in the relativistic limit. Nature Physics, **2**, 456-459 (2006).

[25] K. Shiraga *et al.* Determination of the complex dielectric constant of an epithelial cell monolayer in the terahertz region. App. Phys. Lett. **102**, 5 (2013).

[26] W. Zouaghi *et al.* Broadband terahertz spectroscopy: principles, fundamental research and potential for industrial applications. Our. J. Phys. **34** S179 (2013).

[27] W. L. Chan *et al.* Imaging with terahertz radiation. Rep. Prog. Phys. **70** 1325 (2007).

[28] E. Förster *et al.* X-Ray Microscopy of Laser-Produced Plasmas. with the Use of Bent Crystals, Laser Part. Beams **9**, 1 (1991).

[29] M. Notley *et al.* "A K-alpha Imaging Crystal diagnostic for CLF". https://www.clf.stfc.ac.uk/Pages/80.pdf (accessed 26/01/2021).

[30] H. Nishimura *et al.* Kα spectroscopy to study energy transport in ultrahigh-intensity laser produced plasmas. Journal of Quantitative Spectroscopy and Radiative Transfer, **87**, 2 (2004).

[31] P. Köster *et al.* Experimental investigation of fast electron transport through Kα imaging and spectroscopy in relativistic laser–solid interactions. Plasma Phys. Control. Fusion **51** 014007 (2009).

[32] P. Koester *et al.* X-ray measurements of laser-solid interactions on the PW laser. CENTRAL LASER FACILITY ANNUAL REPORT (2007).

[33] X. X. Lin *et al.* Note: Diagnosing femtosecond laser-solid interactions with monochromatic Kα imager and x-ray pinhole camera. Rev. Sci. Instrum. **82**, 036104 (2011).

[34] R. Trebino. "Frequency-Resolved Optical Gating: The Measurement of Ultrashort Laser Pulses'. Springer US, Boston, MA (2000).

[35] S. Akturk *et al.* Measuring spatial chirp in ultrashort pulses using single-shot Frequency-Resolved Optical Gating. Optics Express. **11**, 1 (2003).

[36] https://www.rp-photonics.com/frequency_resolved_optical_gating.html (accessed 26/01/2021).

[37] N. Bloembergen and P. Lallemand. Complex intensity-dependent index of refraction, frequency broadening of stimulated Raman lines, and stimulated Rayleigh scattering. Phys. Rev. Lett, **16**, 81 (1966).

[38] R. G. Brewer. Frequency shifts in self-focusing light. Phys. Rev. Lett. **19**, 8 (1967).

[39] F. Shimizu, "Frequency broadening in liquids by a short light pulse", Phys. Rev. Lett. **19**, 1097 (1967).

[40] R. H. Stolen and C. Lin. Self-phase modulation in silica optical fibers. Phys. Rev. A **17**, 1448–1453 (1978).

[41] N. L. Markaryan, L. K. Muradyan, and T. A. Papazyan. Spectral compression of ultrashort laser pulses. Sov. J. Quantum Electron. **21**, 783–785 (1991).

[42] C. Finot and S. Boscolo. Design rules for nonlinear spectral compression in optical fibers. J. Opt. Soc. Am. B **33**, 760–767 (2016).

[43] M. Oberthaler and R. A. Höpfel. Spectral narrowing of ultrashort laser pulses by self-phase modulation in optical fibers. Appl. Phys. Lett. **63**, 1017–1019 (1993).

[44] P. E. Powers. "Field Guide to Nonlinear Optics". SPIE Field Guides, FG29 (2013).

[45] R. Paschotta. "Effect of self-phase modulation on the pulse bandwidth". https://www.rp-photonics.com/self_phase_modulation.html (accessed 29/01/2021)

[46] T. A. Birks *et al.* Supercontinuum generation in tapered fibers. Optical Letters, **19**, 25, pp. 1415-1417 (2000).

[47] M. Göppert-Mayer. Uber elementarakte mit zwei quantensprungen. Annalen der Physik, 401, **3**, 273–294 (1931).

[48] L. Keldysh. Ionization in the field of a strong electromagnetic wave. Sov. Phys. JETP, 20, **5**, 1307–1314 (1965).

[49] P Gibbon. Short Pulse Laser Interactions With Matter: An Introduction. Imperial College Press (2005).

[50] F. F. Chen. Introduction to Plasma Physics and Controlled Fusion: 2nd Edition, Springer (2005).

[51] T. J. M. Boyd and J. J. Sanderson. The physics of plasmas. Cambridge University Press (2003).

[52] P. Debye and E. Huckel. The theory of electrolytes i. the lowering of the freezing point and related occurrences. PHYSIKALISCHE ZEITSCHRIFT, **24**, 185–206 (1923).

[53] R. O. Dendy. Plasma Physics: An Introductory Course. Cambridge University Press (1995).

[54] I. Langmuir. Oscillations in ionized gases. Proceedings of the National Academy of Sciences of the United States of America, **14**, 8 (1928).

[55] L. Tonks and I. Langmuir. Oscillations in ionized gases. Physical Review, 33, **2**, 195 (1929).

[56] A. Macchi, S. Veghini, and F. Pegoraro. Light sail acceleration reexamined. Phys. Rev. Lett., **103**, 085003 (2009). [pages 50, 59]

[57] S. Bulanov, C. Schroeder, E. Esarey, and W. Leemans. Optimized laser pulse profile for efficient radiation pressure acceleration of ions. Physics of Plasmas, **19**, 093112 (2012).

[58] V. Vshivkov, M. Naumova, F. Pegoraro, and S. V. Bulanov. Nonlinear electrodynamics of the interaction of ultra-intense laser pulses with a thin foil. Physics of Plasmas, **5**, 2727–2741 (1998).

[59] A. Higginson,*et al.* Near-100 MeV protons via a laser-driven transparency-enhanced hybrid acceleration scheme. Nature Commun. **9**, 724 (2018).

[60] J.D. Lawson, IEEE Trans. Nucl. Sci. NS-26, 4217 (1979).

[61] P. Gibbon and E. Förster. Short-pulse laser-plasma interactions. Plasma physics and controlled fusion, **38**, 769 (1996).

[62] GJ. Pert. Inverse bremsstrahlung in strong radiation fields at low temperatures. Physical Review E, 51, **5**, 4778 (1995).

[63] L. Schlessinger and J. Wright. Inverse-bremsstrahlung absorption rate in an intense laser field. Physical Review A, **20**, 1934 (1979).

[64] J. P. Freidberg, R. W. Mitchell, R. L. Morse, and L. I. Rudsinski. Resonant Absorption of Laser Light by Plasma Targets. Phys. Rev. Lett. **28**, 795 (1972).

[65] S.C. Wilks and W.L. Kruer. Absorption of ultrashort, ultra-intense laser light by solids and overdense plasmas. IEEE Journal of Quantum Electronics, **33**, 1954–1968 (1997).

[66] P. Mulser and D. Bauer. High power laser-matter interaction, **238**. Springer (2010). [pages 41, 44, 46]

[67] D. Forslund, J. Kindel, K. Lee, E. Lindman, and R. Morse. Theory and simulation of resonant absorption in a hot plasma. Physical Review A, **11**, 679 (1975). [page 44]

[68] S. Eliezer. The interaction of high-power lasers with plasmas. Series in plasma physics. Institute of Physics Publishing, Bristol, Philadelphia, (2002). [page 44]

[69] J. C. Kieffer *et al.* Short-pulse laser absorption in very steep plasma density gradients. Physical Review Letters, **62** (1989).

[70] F Brunel. Not-so-resonant, resonant absorption. Physical Review Letters, **59**, 6–9 (1987).

[71] P. Gibbon and A. R. Bell. Collisionless absorption in sharp-edged plasmas. Physical review letters, **68**, 10 (1992).

[72] W. L. Kruer and K. Estabrook. J× B heating by very intense laser light. Physics of Fluids, **28** (1985).

[73] A. Macchi. "A Superintense Laser-plasma Interaction Theory Primer". Springer, (2013). [pages 36, 39, 41, 46, 59]

[74] P. Mora. Theoretical model of absorption of laser light by a plasma. The Physics of Fluids, 25, **6**, 1051–1056 1982.

[75] P. Mora, Plasma Expansion into a Vacuum. Phys. Rev. Lett. **18**, 90, 185002 (2003).

[76] , B Bezzerides, SJ Gitomer, and DW Forslund. Randomness, Maxwellian Distributions, and Resonance Absorption. Physical Review Letters, **44**, 651654 (1980).

[77] P. M. Nilson *et al.* Bulk heating of solid-density plasmas during high-intensity-laser plasma interactions. Physical Review E, **79**, 1 (2009).

[78] C. D. Chen *et al.* Bremsstrahlung and K-alpha fluorescence measurements for inferring conversion efficiencies into fast ignition relevant hot electrons. Physics of Plasmas. **16**, 082705 (2009)

[79] J. R. Davies. Laser absorption by overdense plasmas in the relativistic regime. Plasma Physics and Controlled Fusion. **51**, 0144006 (2009).

[80] F. N. Beg, *et al.* A study of picosecond lasersolid interactions up to 10^{19} Wcm^2. Physics of Plasmas, **4**, 447 (1997).

[81] J. Fuchs, *et al.* Dynamics of subpicosecond relativistic laser pulse self-channeling in an underdense preformed plasma. Physical review letters, **80**, 1658 (1998). [pages 9, 66]

[82] A. Lei, *et al.* Relativistic laser channeling in plasmas for fast ignition. Physical Review E, **76**, 066403 (2007). [pages 9, 66]

[83] R. J. Gray, *et al.* New J. Phys. **16**, 113075 (2014)

[84] B. Gonzalez-Izquierdo, *et al.* Optically controlled dense current structures driven by relativistic plasma aperture-induced diffraction, Nature Phys. **12**, 505 (2016).

[85] I. N. Ross *et al.* The prospects for ultrashort pulse duration and ultrahigh intensity using optical parametric chirped pulse amplifiers. Optics Communications, **144**, 125-133 (1997).

[86] I. Jovanovic *et al.* Optical parametric chirped-pulse amplification in periodically poled $KTiOPO_4$ at 1053 nm. App. Phys. Lett., 83, **20**, 4125–4127 (2003).

[87] D. Herrmann, *et al.* Generation of sub-three-cycle, 16 TW light pulses by using noncollinear optical parametric chirped-pulse amplification. Optics Letters, **34**, 2459–2461 (2009).

[88] S. Witte and S. E. Eikema. Ultrafast optical parametric chirped-pulse amplification. IEEE Journal of Selected Topics in Quantum Electronics, **18**, 296–307 (2012).

[89] A. Dubietis *et al.* Powerful femtosecond pulse generation by chirped and stretched pulse parametric amplification in BBO crystal. Optics Communications, **88**, 437–440 (1992).

[90] D. N. Papadopoulos *et al.* High-contrast 10 fs OPCPA based front end for multi-PW laser chains. Optics Letters, **42**, 3530–3533 (2017).

[91] C. Ziener *et al.* Specular reflectivity of plasma mirrors as a function of intensity, pulse duration, and angle of incidence. Journal of Applied Physics, **93**, 768–770 (2003).

[92] B. Dromey, S. Kar, M. Zepf, and P. Foster. The plasma mirror—A subpicosecond optical switch for ultrahigh power lasers. Rev. Sci. Instrum. **75**, 645 (2004).

[93] C. Thaury *et al.* Plasma mirrors for ultrahigh-intensity optics. Nature Physics, **3**, 424, (2007).

[94] R. Wilson *et al.* Development of Focusing Plasma Mirrors for Ultraintense Laser-Driven Particle and Radiation Sources. Quantum Beam Sci. **2**, 1 (2018).

[95] T. Ebert, *et al.* Enhanced brightness of a laser-driven X-ray and particle source by microstructured surfaces of silicon targets. Physics of Plasmas **27**, 043106 (2020).

[96] M. Nakatsutsumi, *et al.* Fast focusing of short-pulse lasers by innovative plasma optics toward extreme intensity. Optics Letters, **35**, 2314–2316 (2010).

[97] R. Wilson *et al.* Ellipsoidal plasma mirror focusing of high power laser pulses to ultra-high intensities. Physics of Plasmas, **23**, 033106 (2016).

[98] https://www.gsi.de (accessed 26/5/2020).

[99] https://www.clf.stfc.ac.uk/Pages/Vulcan (accessed 20/9/2020).

[100] C. J. Hooker, *et al.* The Astra Gemini project-A dual-beam petawatt Ti: Sapphire laser system. Journal de Physique IV, **133**, pages 673–677. EDP Sciences (2006).

[101] J. MacKay and S. Butcher. Choosing a tunable ultrafast laser system. Laser Focus World. **42**, 7 (2006).

[102] J. S. Pearlman *et al.* Emission of rf radiation from laser-produced plasmas. Journal of Applied Physics **49**, 457 (1978).

[103] M. De Marco *et al.* Electromagnetic pulse (EMP) radiation by laser interaction with a solid H2 ribbon. Physics of Plasmas **24**, 083103 (2017).

[104] M. J. Mead *et al.* Electromagnetic pulse generation within a petawatt laser target chamber. Review of Scientific Instruments **75**, 4225 (2004).

[105] P. Bradford *et al.* EMP control and characterization on high-power laser systems. High Power Laser Science and Engineering, **6**, 21 (2018).

[106] R. L. Zaffino *et al.* Wafer-scale fabrication of target arrays for stable generation of proton beams by laser-plasma interaction. IOP Conf. Series: Journal of Physics: Conf. **1079** (2018).

[107] S. J. Haney *et al.* Prototype high-speed tape target transport for a laser plasma soft-x-ray projection lithography source. Applied Optics, **32**, 34 (1993).

[108] S. Jiang, *et al.* Effects of front-surface target structures on properties of relativistic laser-plasma electrons. Phys. Rev. E. **89**, 013106 (2014).

[109] D. Margarone, *et al.* Laser-Driven Proton Acceleration Enhancement by Nanostructured Foils. Phys. Rev. Lett. **109**, 234801 (2012).

[110] D. Zhuang and J. H. Edgar. Mater. Sci. Eng. R Reports **48**, 1 (2005).

[111] A. A. Tseng, K. Chen, C. D. Chen, and K. J. Ma, IEEE Trans. Electron. Packag. Manuf. **26**, 2 (2003).

[112] J. Kong, A. M. Cassell, and H. Dai, Chem. Phys. Lett. **292**, 4 (1998).

[113] B. R. Tull, J. E. Carey, E. Mazur, J. P. McDonald, and S. M. Yalisove, MRS Bull. **31**, 8 (2006).

[114] R. J. Gray *et al.* Enhanced laser-energy coupling to dense plasmas driven by recirculating electron currents. New J. Phys. **20** 033021 (2018).

[115] M. Singh and R. P. Sharma. Generation of THz Radiation by Laser Plasma Interaction. Contrib. Plasma Phys. **53**, 540 (2013).

[116] C. K. Birdsall and B. A. Langdon. Plasma physics via computer simulation. CRC press 2004.

[117] M. M. Marinak *et al.* Three-dimensional HYDRA simulations of National Ignition Facility targets. Physics of Plasmas, **8**, 5 (2001).

[118] T. D. Arber *et al.* Contemporary particle-in-cell approach to laser-plasma modelling. Plasma Physics and Controlled Fusion, **57**, 113001 (2015).

[119] J. P. Boris. Relativistic plasma simulation-optimization of a hybrid code. In Proceedings of the 4th Conference on Numerical Simulations of Plasmas, pages 3–67 (1970).

[120] R. W. Hockney. Measurements of collision and heating times in a two-dimensional thermal computer plasma. Journal of Computational Physics, **8**, 19–44 (1971).

[121] J. Vyskocil *et al.* Simulations of bremsstrahlung emission in ultra-intense laser interactions with foil targets. Plasma Phys. Control. Fusion. **60** 054013 (2018).

[122] https://www.zemax.com/products/opticstudio. (Accessed 29/12/2020).

[123] D. C. Carroll, *et al.* A modified Thomson parabola spectrometer for high resolution multi-MeV ion measurements - application to laser-driven ion acceleration. Nuc. Inst. Methods in Physics A **620**, 1 (2010).

[124] D. Rusby, *et al.* Measurement of the angle, temperature and flux of fast electrons emitted from intense laser–solid interactions. J. Plasma Phys, **81**, 475810505 (2015).

[125] M. Zepf, *et al.* Fast particle generation and energy transport in laser-solid interactions. Appl. Phys. Lett. **8**, 2323 (2001).

[126] H. Chen *et al.* Hot-Electron Characterization from Kα Measurements in High-Contrast, p-Polarized, Picosecond Laser-Plasma Interactions. Phys. Rev. Lett. **70**, 22 (1993).

[127] Z. Yang, *et al.* Space-Resolved Diagnosis for Electron Temperature of Laser-Produced Aluminum Plasma. Phys. Lett. **28**, 065201 (2011).

[128] J. P. Zou *et al.* Design and current progress of the Apollon 10 PW project. High Power Laser Sci. Eng. **3** (2016).

[129] B. Rus *et al.* ELI-Beamlines laser systems: Status and design options. Proc. SPIE, 87801T (2013).

[130] T.-H. Her, R. J. Finlay, C. Wu, S. Deliwala and E. Mazur. Microstructuring of silicon with femtosecond laser pulses. Appl. Phys. Lett. **73**, 1673 (1998).

[131] T. Ebert, N. W. Neumann, T. Abel, G. Schaumann and M. Roth, Laser-induced microstructures on silicon for laser-driven acceleration experiment. High Power Laser Sci. Eng. **13**, 18 (2017).

[132] Born and Wolf, "Principles of Optics". p. 427 (1999).

[133] J. Parashar and A. K. Sharma. Second-harmonic generation by an obliquely incident laser on a vacuum-plasma interface. EPL **41** 389 (1998).

[134] T. D. Arber, *et al.* Contemporary particle-in-cell approach to laser-plasma modeling. Plasma Phys. Control. Fusion **57**, 113001 (2015).

[135] A. Diaw and P. Mora. Thin-foil expansion into a vacuum with a two-temperature electron distribution function. Physical Review E. **86**, 026403 (2012).

[136] Yuri, Mathworks File Exchange, https://bit.ly/2xUoAtP

[137] A. Fresnel, "Mémoire sur la diffraction de la lumière" (deposited 1818, "crowned" 1819), in Oeuvres complètes (Paris: Imprimerie impériale, 1866–70), **1**, pp. 247–363

[138] "Huygens' Principle". https://www.mathpages.com/ (Retrieved 2020-10-01).

[139] A. J. Kemp and L. Divol. What is the surface temperature of a solid irradiated by a Petawatt laser? Phys. Plasmas **23**, 090703 (2016)

[140] B. Gonzalez-Izquierdo *et al.* Radiation Pressure-Driven Plasma Surface Dynamics in Ultra-Intense Laser Pulse Interactions with Ultra-Thin Foils. Appl. Sci. **8**, 336 (2018).

[141] Wilks, S. C. *et al.* Energetic proton generation in ultra-intense laser-solid interactions. Phys. Plasmas **8**, 542 (2001).

[142] P L Poole *et al.* New J. Phys. **20** 013019 (2018).

[143] T. Esirkepov *et al.* Phys. Rev. Lett. **92**, 175003 (2004).

[144] A. P. L. Robinson, M Zepf, S Kar, R G Evans, C Bellei. Radiation pressure acceleration of thin foils with circularly polarized laser pulses. New Journal of Physics, **10**, 013021 (2008).

[145] S. D. R. Williamson *et al.* Energy absorption and coupling to electrons in the transition from surface- to volume-dominant intense laser–plasma interaction regimes. New J. Phys. **22** 053044 (2020).

[146] T. P. Frazer *et al.* Enhanced laser intensity and ion acceleration due to self-focusing in relativistically transparent ultrathin targets. Phys. Rev. Research **2**, 042015 (2020).

[147] X. Zhao and Y. C. Sing. Laser–plasma interaction and plasma enhancement by ultrashort double-pulse ablation. Applied Physics B **120** 81-87 (2015).

[148] J. Parashar and A. K. Sharma. Second-harmonic generation by an obliquely incident laser on a vacuum-plasma interface. Europhys. Lett. **41**, 389 (1998).

[149] K. Adusumilli, D. Goyal, and V. K. Tripathi. Relativistic second harmonic generation from an S-polarized laser in over-dense plasma. Physics of Plasmas **18**, 083105 (2011).

[150] F. A. Jenkins and H. E. White Fundamentals of Optics 3rd.ed. (1957).

[151] G. B. Airy. "On the Diffraction of an Object-glass with Circular Aperture". Transactions of the Cambridge Philosophical Society. 283–91 (1835).

[152] E. Hecht. "Optics" 2nd.ed. (1987).

[153] http://hyperphysics.phy-astr.gsu.edu/hbase/phyopt/sindoub.html (accessed 11/8/20).

[154] N. Naseri *et al.* Self-channelling of relativistic laser pulses in large-scale underdense plasmas. Physics of Plasmas **17**, 033107 (2010).

[155] M. J. Duff, *et al.* High order mode structure of intense light fields generated via a laser-driven relativistic plasma aperture. Sci Rep **10**, 105 (2020).

[156] M. Zepf *et al.* Physics of Plasmas **3**, 3242 (1996).

[157] S. V. Bulanov *et al.* Light Intensification towards the Schwinger Limit. Phys. Rev. Lett. **91**, 8 (2003).

[158] S. Modal *et al.* Phys. Rev. Lett. **105**, 105002 (2010)

[159] J. Kerr. "A new relation between electricity and light: Dielectrified media birefringent". Philosophical Magazine. **4**, 50, 332, 337–348 (1875).

[160] D. Duchesne *et al.* High Performance, Low-loss Nonlinear Integrated Glass Waveguides. PIERS Online, **6**, 3 (2010).

[161] E. T. J. Nibbering *et al.* Spectral determination of the amplitude and the phase of intense ultrashort optical pulses. J. Opt. Soc. Am. B. **13**, 2 (1996).

[162] A. Elena *et al.* Single-shot laser pulse reconstruction based on self-phase modulated spectra measurements. Sci. Rep. **6**, 33749 (2016).

[163] M. Streeter. Ultrafast Dynamics of Relativistic Laser Plasma Interactions, PhD Thesis (2013).